

RESEARCH ARTICLE | FEBRUARY 18 2026

Planing hull dynamics in water waves: Physical insights from nonlinear strip theory models and fully nonlinear computational fluid dynamics simulations

Sasan Tavakoli  ; Rasul Niazmand Bilandi  ; Fatemeh Roshan  ; Mansi Singh  ; Simone Mancini 



Physics of Fluids 38, 027129 (2026)

<https://doi.org/10.1063/5.0311446>



Articles You May Be Interested In

Hydrodynamic analysis of a catamaran derived from a Fritsma planing hull: Effects of demi-hull spacing, wake dynamics, and resistance

Physics of Fluids (December 2025)

Experimental study of hydrodynamic effect of loading and longitudinal variations of the center of gravity on the performance of a single-step craft in calm water

Physics of Fluids (December 2024)

Effects of yaw angle on hydrodynamic performance for an oblique planing hull

AIP Advances (August 2024)



AIP Advances

Why Publish With Us?

21 DAYS average time to 1st decision

OVER 4 MILLION views in the last year

INCLUSIVE scope

Learn More

AIP Publishing

Planing hull dynamics in water waves: Physical insights from nonlinear strip theory models and fully nonlinear computational fluid dynamics simulations

Cite as: Phys. Fluids **38**, 027129 (2026); doi: [10.1063/5.0311446](https://doi.org/10.1063/5.0311446)

Submitted: 10 November 2025 · Accepted: 4 January 2026 ·

Published Online: 18 February 2026



View Online



Export Citation



CrossMark

Sasan Tavakoli,^{1,2,a)} Rasul Niazmand Bilandi,³ Fatemeh Roshan,⁴ Mansi Singh,⁵ and Simone Mancini^{3,6}

AFFILIATIONS

¹Australian Maritime College, University of Tasmania, Newnham, TAS 7250, Australia

²Department of Infrastructure Engineering, The University of Melbourne, Parkville, VIC 3031, Australia

³Hydro and Aerodynamic Department, FORCE Technology, 2800 Kongens Lyngby, Denmark

⁴Estonian Maritime College, Tallinn University of Technology, Kuressaare, Estonia

⁵Mathematical Institute for Machine Learning and Data Science, Katholische Universität Eichstätt-Ingolstadt, Ingolstadt 85049, Germany

⁶Department of Industrial Engineering, University of Naples "Federico II," Naples, Italy

^{a)}Author to whom correspondence should be addressed: sasan.tavakoli@utas.edu.au

ABSTRACT

The dynamic motions of planing hulls in water waves represent a well-known example of a strongly nonlinear fluid–structure interaction problem, where wave-induced motions are governed by intermittent contact, spray formation, transom wake flow, and higher-harmonic responses. In this study, nonlinear strip theory models, namely, two-dimensional plus time ($2D + t$) models, extending classical strip theory formulations by incorporating nonlinear wave kinematics and an improved analytical water-entry solution that captures nonlinearity, are developed alongside a fully nonlinear computational fluid dynamics (CFD) model based on a Reynolds-averaged Navier–Stokes solver. These models are employed to investigate the physics of nonlinear unsteady planing motions under different wave conditions. Results show that the second harmonic of the heave motion tends to increase with wave steepness, whereas that of the pitch motion may decrease due to the onset of airborne phases. The higher harmonics of heave and pitch in short waves are primarily caused by intermittent wetted-surface variations and wave scattering, the latter introducing irregularities in the response that are absent in the $2D + t$ model. At intermediate wavelengths, nonlinearities arise mainly from airborne motion and subsequent slamming impacts, while at long-wave conditions, additional effects, including water detachment and subsurface vorticity generation, contribute to the nonlinear response, phenomena captured only by the CFD simulations. Consequently, the response amplitude operators of heave and pitch are seen to increase with wave steepness in long-wave conditions when computed using the CFD model. This distinction highlights that, although the second-order and earlier $2D + t$ formulations remain valuable predictive tools, they cannot fully reproduce the nonlinear behavior observed in steep-wave regimes. Specifically, they can have application in the early-stage design, rapid parametric studies for physical studies, and long-duration simulations due to its low computational cost and clear physical interpretability.

© 2026 Author(s). All article content, except where otherwise noted, is licensed under a Creative Commons Attribution (CC BY) license (<https://creativecommons.org/licenses/by/4.0/>). <https://doi.org/10.1063/5.0311446>

I. INTRODUCTION

Planing hulls are high-speed marine vessels that have been in use for over a century.¹ These craft operate under the support of hydrodynamic lift, which raises the vessel and allows it to travel with a bow-up attitude, thereby reducing wave generation at the bow and minimizing

the wetted-surface area.² As a result, they are capable of achieving relatively high speeds on the water. The fluid dynamics around planing vessels are significantly more complex than those around conventional displacement ships (i.e., vessels whose weight is fully supported by buoyancy). This complexity arises from the fact that the bottom

surface of the hull may partially or fully ride on the water surface, leading to highly nonlinear flow phenomena with minimal hydrodynamic contact. These include lifting surface problem,^{3–5} spray formation,^{6,7} transom flow,^{8,9} narrow wake waves,^{10–12} and water separation,¹³ all of which contribute to the challenges in accurately modeling their hydrodynamic behavior, including calm-water performance, maneuvering, and seakeeping, and require a thorough understanding of the underlying physics and the associated fluid-dynamic nonlinearities.

The complex nature of the fluid motion around planing hulls significantly affects their performance in both calm and rough water. In calm conditions, an improper loading configuration can lead to an unbalanced distribution of hydrodynamic pressure,¹⁴ particularly along the transverse axis of the vessel. This may destabilize the ride and give rise to instabilities such as porpoising and chine walking.^{15–17} In rough water, the wave-induced motions are strongly influenced by nonlinearities associated with the planing hydrodynamics.¹⁸ Since hydrodynamic contact with the water is minimal and the vessel rides near the surface, the inertia, damping, and restoring forces may vary significantly even with small rigid-body motions.¹⁹ This results in a highly nonlinear response to incident waves, including those categorized as mildly or gently sloped waves.^{20–22}

In particular, the forebody of the vessel frequently exits and reenters the water, while the aft section experiences considerable variation in immersion, from shallow to deep, during each cycle. In the deeply immersed condition in the rear part of the vessel (i.e., near transom), hydrodynamic pressures diminish, and hydrostatic pressure becomes the dominant contributor. These effects can induce large accelerations, especially near the bow, and may lead to significant heave and pitch responses in the resonance region, where the wavelength of an incoming head wave is typically between three and fourth times the length of vessel.^{20,23} Experimental results have revealed that the second harmonic may contribute in the pitch response, and second and third harmonics may contribute to the vertical acceleration of the vessel at bow or even its center of gravity.^{19,22,23} The motion in random sea is also seen to be highly nonlinear. The probability density of the pitch response has been reported to deviate from the Gaussian distribution, while the exceedance probabilities of heave, pitch, and CG acceleration do not conform to any Rayleigh distribution.²⁴ Under random wave conditions, intermittency in the heave and pitch motions is observed, which is seen to increase with increasing wave steepness and speed. This demonstrates how slamming can induce nonlinearity in the response and, consequently, how non-Gaussianity emerges.²⁵ Recent towing tank experiments conducted under random wave conditions have revealed extremely high slamming pressures during water re-entry events, each of which can induce significant strain in the hull panels subjected to impact.^{26,27}

The physical tests on planing dynamic motion in rough water has been conducted since 1950s, with the most famous set of experiments run by Fridsma in late 1960s.²⁰ These were followed by several further campaigns from the 1990s through to the 2020s. Most of these experiments focused on planing motions in regular waves, typically reporting how hull form influences the motions of planing craft, or how such motions exhibit nonlinear characteristics (see examples in Refs. 22, 23, and 28–30). Among the many physical tests conducted over the years, the contribution by Pigazzini *et al.*²² provides a particularly deep physical insight into motion nonlinearities in regular wave conditions. The authors showed that the RAOs of heave and pitch decrease with

increasing wave steepness, while the second-harmonic components grow with steepness. This clearly demonstrates the presence of nonlinearities in the measured heave and pitch responses of a planing hull in regular waves.

The motion of planing hulls cannot be accurately captured using linear models, including frequency-domain panel methods. These approaches typically neglect the temporal variation of displaced volume and completely omit the contribution of hydrodynamic lift. Yet, linear models have been seen to be employed to model motions of planing hulls in waves (e.g., in Ref. 31). The most common strategies found in the literature involve either weakly nonlinear strip theory models or fully nonlinear computational fluid dynamics (CFD) simulations. The weakly nonlinear strip theory approach solving unsteady planing motion was first introduced to the naval architecture community by Zarnick³² and has been further developed by different scholars over time. The original model assumes that the vessel can be divided into a finite number of strips, and the force acting on each can be determined using a water entry problem by neglecting the gravity effects. Hence, no oscillatory radiation force is assumed, unlike the typical weakly nonlinear strip theories developed for displacement ships (e.g., in Ref. 33).

Zarnick original model was developed for linearized water waves, with nonlinearity of hydrodynamic force introduced through a single additional force term, namely, cross-flow drag, although the boat dynamic was simulated using a weakly nonlinear approach. That is, the time-varying added mass, lift force, pitching moment, and the Froude-Krylov force were all computed based on the wetted area. The water-entry force was formulated by considering the momentum variation of the added mass associated with each section entering the water based on Von Karman and Wagner water-entry models,^{34,35} an approach that demonstrated reasonable accuracy in predicting rigid-body responses.³⁶

Subsequent efforts focused on developing more accurate methods for calculating the added mass around each section.^{37–42} Over time, the approach was further extended to calm-water performance modeling (e.g., in Refs. 43–45) asymmetric planing (e.g., in Refs. 46–48) and maneuvering simulations (e.g., in Refs. 49–52). More recently, it has also been adapted to simulate the nonlinear motions of stepped planing surfaces⁵³ by considering tandem configurations in which the planing surfaces act sequentially (one after another).

Up to now, three major physics-related considerations have largely been overlooked in strip theory models developed for planing hull motions. The first concerns wave nonlinearity. Most existing models have been developed for linear waves, despite the inherently nonlinear nature of water waves. Even regular waves can exhibit significant nonlinearity and may be better represented using higher-order wave theories, such as second- or fifth-order Stokes theory.^{54,55} However, for irregular waves, the challenge becomes more pronounced. Phenomena such as modulation instability arise, which are difficult to incorporate into ship motion models unless coupled with advanced numerical approaches, such as high-order spectral methods⁵⁶ or the Chalikov model.^{57,58}

The second consideration relates to nonlinearities in the sectional flow, which are most often addressed using simplified momentum variation models. A notable exception is the boundary element method (BEM)-based approach of Sun and Faltinsen,⁵⁹ which provides a more accurate representation of nonlinearities associate with sectional

hydrodynamics. However, incorporating BEM-based methods into strip theory is relatively challenging, despite the availability of rich analytical water-entry models (e.g., Refs. 60–65). It remains an open question why these robust models have not gained wider adoption in the community. This concern was explicitly raised by Korobkin *et al.*,⁶⁶ who argued that the theoretical foundations of the field (the argument is related to hydroelasticity but can be valid for the present problem too) are being overlooked by modelers and that accurate and reliable modeling cannot be achieved without a rigorous theoretical basis.

The third concern relates to hydroelastic effects, which may arise at both local (e.g., Refs. 27, 64, and 67–73) and global scales.^{74–76} At the local level, dynamic structural responses within individual sections can significantly influence the surrounding flow field and the resulting pressure distribution, primarily due to fluid–solid momentum exchange. This becomes particularly important for wedge-shaped bodies when the relative sectional velocity is low, in which case structural natural modes may influence the pressure response.^{72,77}

From a global perspective, hydroelasticity may manifest through the coupling of the symmetric elastic modes with the longitudinal pressure distribution. For example, through variations in the local angle of attack along the hull, these global effects have not yet been incorporated into existing strip theory models and, while important, lie beyond the scope of the present study. Yet, this approach has been applied in the modeling of displacement ships in the literature (e.g., in Refs. 78 and 79). For a comprehensive review on marine hydroelasticity with future possible research directions with emphasis on the dynamic responses of ships, refer to Tavakoli *et al.*⁸⁰

With the first two concerns in mind, their incorporation into modeling approaches is essential, not only because it may improve the accuracy of the predictions, but more importantly because it enables a deeper understanding of the dynamic responses of planing hulls. Addressing these nonlinearities allows for a more focused investigation of their role in dynamics of the vessel riding in waves, ultimately contributing to more robust and physically grounded models. That is, it can help in understanding the physics of unsteady planing motion in waves.

Given this, the first objective of this article is therefore to introduce a second-order $2D + t$ model that incorporates nonlinear wave effects and a modified analytical water-entry formulation accounting for pressure nonlinearity. This second-order $2D + t$ model is introduced to address two specific gaps in the previous models, namely: (I) the absence of nonlinear wave kinematics in the external wave forcing condition, which is currently taken as the Airy model, and (II) the classical water-entry formulation, which is herein replaced by a general Wagner-based model, together with the inclusion of other nonlinear terms. Incorporating second-order Stokes wave theory and an alternative water-entry formulation may provide a more physically grounded simulation of planing motion, the results of which may differ from those of previous models and are therefore worth exploring. This may not necessarily offer a universal improvement in accuracy, but it opens the door to exploring other versions of the model and can help us understand how the nonlinear nature of the response may differ under the inclusion of different nonlinear mechanisms.

In addition, a viscous-based CFD model is presented. This inclusion is motivated by the fact that viscous-based simulations, namely, CFD methods, are capable of capturing the dynamic motions of planing hulls by resolving fully nonlinear hydrodynamic behavior,

including turbulence development around the hull. Both meshed (e.g., Refs. 81 and 82) and meshless (e.g., Refs. 83 and 84) approaches have been explored in the literature, although meshed methods are generally preferred due to their superior accuracy and robustness in resolving complex flow features (e.g., Refs. 85–88). Interestingly, CFD approaches have been accepted as a reliable hydrodynamic tool that can be used for solving steady and dynamic motions of ships and floating structures in waves and calm-water conditions (see, e.g., in Refs. 89–94).

Comparing the predictions of the newly developed nonlinear $2D + t$ model with those of a CFD model provides a valuable opportunity to assess the performance of the proposed model against a fully nonlinear benchmark. This comparison also enables a more detailed understanding of the role and significance of nonlinearities in the dynamic response of planing hulls. This leads to the second objective of the present article, which is to investigate the nonlinear characteristics of the motion of a planing hull operating in monochromatic wave conditions using different models.

The second objective of this paper is to provide a deeper understanding of physics of planing motion in waves, and in specific, the influence of wave steepness on the dynamics of planing hulls in waves, and to employ the CFD model to capture the nonlinear effects that arise from wave nonlinearity and body nonlinearity. In doing so, the study addresses a gap in the existing literature. This topic have gained greater attention in the context of similar projects and studies examining ship responses under the action of nonlinear waves. While experimental and numerical investigations have reported ship responses and loads,^{95–104} the focus for planing hulls has largely been on modeling approaches (e.g., Ref. 105) improving accuracy, and motion reduction.^{106,107} However, the underlying physics of the problem, particularly the role of wave steepness and changes in wave characteristics while emphasized on,¹⁰⁸ remains equally important. This is especially relevant since planing hulls often operate in intermediate and finite depth conditions, where waves can become increasingly nonlinear and steeper.

The remaining of this article is organized as follows. The problem is defined in Sec. II. The $2D + t$ models are introduced in Sec. III, where the fundamentals of the approach are first outlined, with each model described in a separate subsection. This is followed by the general method used for solving the problem in the time domain. The fully nonlinear CFD model and the associated numerical method are presented in Sec. IV. The test cases employed for validation and for studying the physics of the problem, together with the geometry of the planing hull, are described in Sec. V. Validation and benchmarking are discussed in Sec. VI. Results obtained from the different methods, including the effects of wave steepness on the dynamic response of the hull, are examined in Sec. VII. The flow field around the planing hull advancing in waves, captured only by the CFD model, is presented in Sec. VIII to highlight the physical features resolved by this approach and to discuss possible sources of discrepancy between the $2D + t$ models and the CFD results. Section IX presents a general comparison of the different models presented in this article. Concluding remarks are given in Sec. X. Some Appendixes are also presented. Appendixes A and B provide theoretical background for the $2D + t$ model. The former presents the second-order wave theory equations implemented in the model, while the latter outlines equations for treating a fictitious half-beam under wet chine conditions. Appendix C compares the

results of the second-order $2D + t$ model using different approaches to clarify how the method should be applied and calibrated when nonlinear terms are incorporated. Finally, [Appendix D](#) presents the mesh study performed to select the most suitable configuration for the CFD simulations. [Appendix E](#) shows the emergence of fly-over motion during CFD simulations and mathematical modeling of the problem. [Appendix F](#) presents the effects of wave steepness on acceleration, as the discussion on acceleration is not included in the main body of the manuscript. [Appendix H](#) provides an example of the wetted surface of the planing hull obtained from the CFD simulations, during which water detachment can be observed.

II. PROBLEM DEFINITION

Let a hard-chine planing hull advance at a constant speed u in the presence of head-sea monochromatic waves. The forward speed is non-dimensionalized by the Froude number based on the beam, expressed as follows:

$$F_B = \frac{u}{\sqrt{gB}}, \quad (1)$$

where $g = 9.81 \text{ m/s}^2$ is gravitational and B denotes the beam of the hull. The geometry of the vessel, in addition to its beam is characterized by the length between perpendiculars, L ; the deadrise angle, β ; and the chine height, h_c . The deadrise angle β is defined as the angle between the inclined hull surface and the horizontal plane, measured in a transverse cross section (i.e., from the bodyline profile). The chine height represents the vertical distance from the keel to the chine in the transverse cross section.

The vessel is hypothetically free to respond in the vertical symmetric rigid modes, namely, heave (z_{CG}) and pitch (θ). The incident wave is characterized by the wave height, H , defined as the vertical distance between crest and trough, wave period T , and wavelength λ , defined as the horizontal distance between two successive crests. The water depth is denoted by D . The wave angular frequency ($\omega = 2\pi/T$) and wavenumber ($k = 2\pi/\lambda$) are related by the dispersion relationship as

$$\omega^2 = gk \tanh(kD). \quad (2)$$

The wave steepness is defined as

$$\varepsilon = k \frac{H}{2}. \quad (3)$$

A sketch of the problem is shown in [Fig. 1](#). To formulate the rigid-body motion equations, two coordinate systems are introduced. The first is a hydrodynamic frame, which translates forward at a speed u but remains unaffected by wave-induced motions. The second is a body-fixed frame, which moves with the vessel and captures its oscillatory behavior. Accordingly, the rigid motions of vessel can be described using rigid-body dynamics as

$$m\ddot{z}_{CG} = F^* + mg \quad \text{and} \quad I_{yy}\ddot{\theta} = M^*, \quad (4)$$

where m is the mass, I_{yy} is the pitch moment of inertia about the transverse axis, \ddot{z}_{CG} and $\ddot{\theta}$ are the vertical acceleration at CG and angular acceleration, and F^* and M^* denote the total hydrodynamic force and moment acting on the hull.

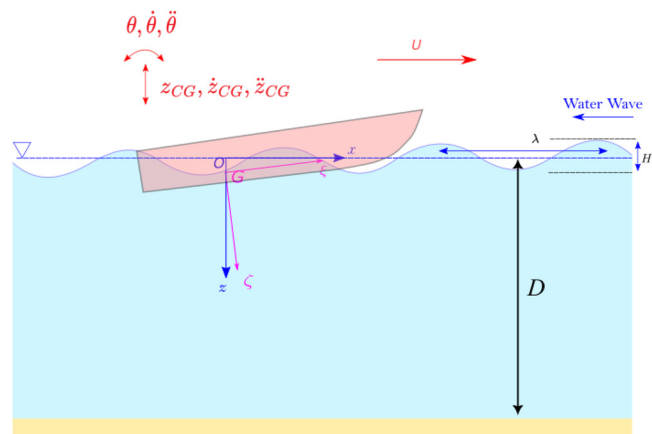


FIG. 1. Sketch of the problem showing a planing hull advancing in regular head waves at $F_B > 1.5$, where the motions are expected to be nonlinear. The rigid-body motions of the vessel are formulated in two coordinate systems, Oxz and $G\xi\zeta$. The vessel is free only in heave (positive downward) and pitch. Wake-driven waves and transom waves may also emerge, but are omitted here for simplicity.

The heave response is local and varies along the length of the vessel. Accordingly, the heave displacement, heave rate, and vertical acceleration at a point located at a longitudinal distance x from the CG are formulated based on classic rigid-body motion equations, and are expressed as follows:

$$z(x, t) \approx z_{CG} - x\theta, \quad (5)$$

$$\dot{z}(x, t) \approx \dot{z}_{CG} - x\dot{\theta}, \quad (6)$$

$$\ddot{z}(x, t) \approx \ddot{z}_{CG} - x\ddot{\theta}, \quad (7)$$

where $x\theta$ is the vertical contribution of pitch motion at position x under a small pitch angle consideration.

Instantaneous motion of the hull at location ξ in the normal direction to the keel (motion of the hull surface at longitudinal coordinate ξ in the body-attached normal direction) can be formulated as follows:

$$\Xi(\xi, t) \approx z_{CG} \cos \theta - \xi\theta, \quad (8)$$

$$\dot{\Xi}(\xi, t) \approx \dot{z}_{CG} \cos \theta - z_{CG} \sin \theta \dot{\theta} - \xi \dot{\theta}, \quad (9)$$

$$\begin{aligned} \ddot{\Xi}(\xi, t) \approx & \ddot{z}_{CG} \cos \theta - 2\dot{z}_{CG} \sin \theta \dot{\theta} - z_{CG} \sin \theta \ddot{\theta} \\ & - z_{CG} \cos \theta \dot{\theta}^2 - \xi \ddot{\theta}. \end{aligned} \quad (10)$$

Here, $z_{CG} \cos \theta$ is the projection of the vertical heave displacement of CG along the direction normal to keel. Instantaneous motion of the hull at location ξ in the direction ship baseline is also approximated as follows:

$$\chi(\xi, t) \approx z_{CG} \sin \theta, \quad (11)$$

$$\dot{\chi} \approx \dot{z}_{CG}(t) \sin \theta + z_{CG} \cos \theta \dot{\theta}, \quad (12)$$

$$\ddot{\chi}(\xi, t) \approx \ddot{z}_{CG} \sin \theta + 2\dot{z}_{CG} \cos \theta \dot{\theta} - z_{CG} \sin \theta \dot{\theta}^2 + z_{CG} \cos \theta \ddot{\theta}. \quad (13)$$

In contrast to heave motion, the pitch angle, pitch rate ($\dot{\theta}$), and pitch acceleration are constant along the vessel.

The heave force and pitching moment vary with time, and depend on the instantaneous position of the vessel, instantaneous wetted-surface area, and instantaneous fluid pressure distribution. The main task is to develop a model that couples rigid-body dynamics with a mathematical or a CFD code capable of resolving F^* and M^* as time-dependent quantities.

III. 2D+t MODELS

2D + t models, including a fully second-order nonlinear formulation and a weakly nonlinear alternative, are considered. The former is developed in the present work, and the latter has been previously introduced and partially improved by various researchers over the past three decades. The general concept of the 2D + t model and its inherent nonlinearity is illustrated in Fig. 2.

A general hypothesis shared by both 2D + t models is that the vessel operates in a non-displacement flow regime, under partial or predominant hydrodynamic lift support. Consequently, the high forward speed governs the flow dynamics around the boat; that is, the flow field is characterized by strong longitudinal velocities and comparatively stronger transverse velocity variations. This justifies the assumption that

$$\left| \frac{\partial}{\partial x} \right| \ll \left| \frac{\partial}{\partial y} \right|, \quad (14)$$

and then, fluid flow around two-dimensional sections of the vessel can be solved. Each section is subsequently assumed to evolve independently of the others, with its flow field varying over time and remaining uncoupled from the wave-induced fluid motion. Under these assumptions, the potential flow around each section can be modeled as an impulsive flow, effectively a two-dimensional water-entry problem.

The flow is then solved for a section subject to an imposed vertical velocity $V(\xi, t)$, a corresponding vertical acceleration $\dot{V}(\xi, t)$, and an instantaneous immersion profile $h(\xi, t)$. In addition, each section may be subjected to a horizontal velocity $U(\xi, t)$ and a corresponding horizontal acceleration, $\dot{U}(\xi, t)$. The sectional forces are subsequently integrated along the vessel length, assuming that longitudinal gradients of the flow field are negligible compared to the transverse gradients. Near the stern, an empirical reduction coefficient is introduced to account for the transom region, where the flow is governed by a Kutta-type condition. The corresponding mathematical formulation is introduced later [it is shown in Eqs. (28), (31) and (32)]. The resulting integrated sectional forces and moments give the total three-dimensional hydrodynamic forces/moment acting on the hull and are employed in the Newton-Euler rigid-body equations to determine the global heave and pitch responses of the vessel.

Immersion depends on the instantaneous relative position of each section with respect to the water surface profile (shown by η), and also the slope of the waves (shown by ν). As such, it can be formulated as follows:

$$h = \frac{\Xi - \eta}{\cos \theta - \nu \sin \theta}. \quad (15)$$

$h(\xi, t)$ temporally varies over time and can be approximated via

$$\dot{h} = \frac{\dot{\Xi} - \dot{\eta}}{\cos \theta - \nu \sin \theta}. \quad (16)$$

Here, the time derivative of the pitch motion is not considered, consistent with the original work of Zarnick.³² In contrast, the relative vertical and horizontal velocity components and corresponding accelerations are dependent of temporal heave and pitch rates, as well as

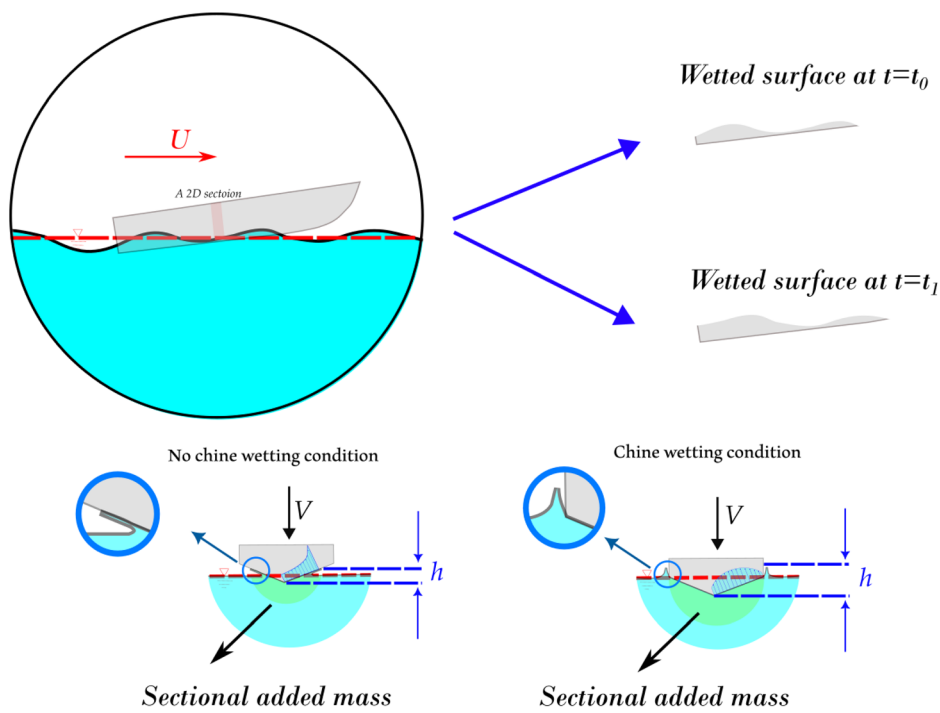


FIG. 2. Schematic showing the general idea of the 2D+t method for modeling the nonlinear motions of a high-speed planing hull in waves. The weakly nonlinear character of the method is highlighted by the wetted surface considered at two different instants on the right side. The bottom panels show two possible phases of the impulsive problem: in one, both chines are dry, so the sectional added mass is below its maximum value although pressures peak near the spray root; in the other, the chines are wetted and a splash is generated, leading to a different pressure pattern with zero pressure at the chine and a larger sectional added mass than in the dry chine case.

the instantaneous horizontal and vertical velocities and accelerations at the air–water interface. To express the relative velocities formally, the horizontal and vertical components are written as

$$U = u \cos \theta + \dot{\chi} - w_x \cos \theta - w_z \sin \theta, \quad (17)$$

$$V = u \sin \theta + \dot{\Xi} - w_x \sin \theta - w_z \cos \theta. \quad (18)$$

Under a zero-surge-motion assumption (i.e., $\dot{u} = 0$), the relative horizontal and vertical accelerations at a section located a distance ξ from the CG are formulated as

$$\ddot{U} = -u \sin \theta \dot{\theta} + \ddot{\chi} - \dot{w}_x \cos \theta + w_x \sin \theta \dot{\theta} - \dot{w}_z \sin \theta - w_z \cos \theta \dot{\theta}, \quad (19)$$

$$\ddot{V} = u \cos \theta \dot{\theta} + \ddot{\Xi} - \dot{w}_x \sin \theta - w_x \cos \theta \dot{\theta} - \dot{w}_z \cos \theta + w_z \sin \theta \dot{\theta}. \quad (20)$$

The fluid flow is solved around a 2D section. To achieve this, a 2D plane with a symmetric V-shape body with a beam of B is considered. A 2D right-handed coordinate system shown with $o'x'y'$ is placed at center of the section, which is described with a function of

$$\mathcal{F}(x') = |x'| \tan \beta. \quad (21)$$

The fluid motion around each section is modeled as incompressible and irrotational, with assuming nil surface tension. As a result, the flow is governed by potential theory. The fluid motion is solved over the domain $|x'| < c$. Here, $|c|$ is the half-wet beam. There are many different theoretical and numerical models developed to solve this problem (e.g., in Refs. 109–116). Herein, the theoretical ones are considered, as they can be more easily implemented within a strip theory framework.

In most two-dimensional water-entry models, the solution is restricted to cases where $c < B/2$. This implies that two distinct regimes must be considered when solving the fluid motion around each section: those for which $c > B/2$ and those for which $c \geq B/2$. These are conventionally referred to as the dry and wet chine conditions, respectively.

A key challenge lies in determining the wetted half-beam c , which is influenced by spray formation along the wedge wall prior to reaching the chine. Once the spray reaches the chine, flow separation typically occurs. Prior to this, under dry chine conditions, the half-wetted beam, c is computed using the Wagner boundary condition,³⁵ which is given as follows:

$$\int_0^{\pi/2} \mathcal{F}(c \cdot \sin \gamma) d\gamma = \frac{\pi}{2} \cdot h. \quad (22)$$

Evaluation the integral presented in Eq. (22) yields in

$$c = \frac{\pi}{2} \frac{h}{\tan \beta}. \quad (23)$$

As seen in Eq. (23), the half-wetted beam c for a section with a dry chine depends on the local immersion depth $h(\xi, t)$. Physically, this implies that c varies with time. The temporal rate of change of the wetted half-beam can therefore be expressed as

$$\dot{c} = \frac{\pi}{2} \frac{\dot{h}}{\tan \beta}, \quad (24)$$

for a two-dimensional section with a dry chine. Insofar as a water rise-up occurs along the hull surface, an effective immersion depth,

denoted by h_e , is introduced to account for this effect. It is defined as follows:

$$h_e = c \tan \beta. \quad (25)$$

The height difference between the effective immersion and the actual immersion is referred to as the water pile-up height. It is calculated as follows:

$$h_{wp} = \left(\frac{\pi}{2} - 1 \right) h. \quad (26)$$

For a wet chine condition, either a fictitious half-wetted beam is computed, or a simplified assumption of $c = B/2$ is considered.

Assuming that the potential flow within the contact region is known [$\varphi(x', y', t)$], the pressure acting on the section can be determined using Bernoulli's equation as follows:

$$p(x', y', t) = -\rho_w \left(\frac{\partial \varphi}{\partial t} + \frac{1}{2} |\nabla \varphi|^2 \right). \quad (27)$$

Under a linear consideration, the nonlinear term $|\nabla \varphi|^2$ is set to be zero, a common simplification adopted in many established models.

Assuming that the fluid force around the sectional forces entering water with impact speed of V , shown with $f(\xi, t)$, is found by integrating the pressure acting on the section, the three-dimensional hydrodynamic force and pitching moment caused by the fluid motion are found as follows:

$$F_{hd}^*(t) = \int_L \mu(\xi) \cdot f_{hd}(\xi, t) d\xi \quad (28)$$

and

$$M_{hd}^*(t) = \int_L \mu(\xi) \cdot \xi \cdot f_{hd}(\xi, t) d\xi. \quad (29)$$

Here, $\mu(\xi)$ is an empirical correction function that introduces the effects of transom to the distribution of the sectional forces across the boat length. Similarly, assuming that the sectional hydrostatic force is found, the three-dimensional hydrostatic force, and three-dimensional hydrostatic pitching moment are found as follows:

$$F_{hs}^*(t) = \int_L \mu(\xi) \cdot f_{hs}(\xi, t) d\xi \quad (30)$$

and

$$M_{hs}^*(t) = \int_L \mu(\xi) \cdot \xi \cdot f_{hs}(\xi, t) d\xi. \quad (31)$$

The transom reduction function is formulated as by Garmen³⁹ as

$$\mu(\xi) = \tanh \left(\frac{2.5}{C} (\xi - \xi_T) \right). \quad (32)$$

Here, ξ_T denotes the longitudinal position of the transom relative to the CG, and C is a constant given by

$$C = 0.34 B F_B. \quad (33)$$

The total three-dimensional hydrodynamic forces are then found as follows:

$$F^*(t) = F_{\text{hd}}^*(t) + F_{\text{hs}}^*(t) \quad \text{and} \quad M^*(t) = M_{\text{hd}}^*(t) + M_{\text{hs}}^*(t). \quad (34)$$

A. Weakly nonlinear 2D+t model

The weakly nonlinear model is introduced first, followed by the development of the fully second-order formulation. This model was originally developed by Zarnick, and any subsequent minor modifications have typically relied on specific simplifications. The first set of these simplifications concerns $\dot{\Xi}$ and $\ddot{\Xi}$, which are commonly approximated as

$$\dot{\Xi}(\xi, t) \approx \dot{z}_{CG} \cos \theta - \xi \dot{\theta}, \quad (35)$$

$$\ddot{\Xi}(\xi, t) \approx \ddot{z}_{CG} \cos \theta - z_{CG} \sin \theta \ddot{\theta} - \xi \ddot{\theta}. \quad (36)$$

Following the same rationale used for the previous simplifications, $\dot{\chi}$ and $\ddot{\chi}$ are also approximated as

$$\dot{\chi}(\xi, t) \approx \dot{z}_{CG} \sin \theta, \quad (37)$$

$$\ddot{\chi}(\xi, t) \approx \ddot{z}_{CG} \sin \theta + z_{CG} \cos \theta \ddot{\theta}. \quad (38)$$

The second assumption, which is present in all previously developed models, concerns the free surface deformation. It is typically formulated based on Airy wave theory, based on which the free surface deformation is written as follows:

$$\eta(x, t) = \frac{H}{2} \cos(kx - \omega t). \quad (39)$$

It is worth noting that Airy wave theory is derived under the assumption of perfectly linear conditions. As such, it imposes limitations on the ability of previously developed 2D + t models to capture the nonlinearities of the free surface. The horizontal and vertical components of the orbital velocity at the mean surface of water are given by

$$w_x(x, t) = \frac{Hgk}{2\omega} \cos(kx - \omega t) \quad (40)$$

and

$$w_z(x, t) = \frac{Hgk}{2\omega} \cdot \frac{\sinh(kD)}{\cosh(kD)} \sin(kx - \omega t). \quad (41)$$

In developing the weakly nonlinear model, w_x is neglected, and its effects on the relative vertical and horizontal forces are omitted by setting

$$w_x = 0. \quad (42)$$

The slope of the water surface is approximated by

$$\nu = -\frac{H}{2} k \sin(kx - \omega t). \quad (43)$$

Assuming that the section immersion, $U(\xi, t)$ and $V(\xi, t)$, along with their time derivatives, is found, the pressure acting on the section and the force can then be approximated. To do so, a flat-disk approximation is applied. That is, it is assumed that a flat disk may represent the V-shape section subjected to impulsive flow.

Here, first the pressure and resulting force for a dry section are approximated. The potential flow acting on the flat disk over $|x| < c$ can be approximated as

$$\varphi(x', 0, t) = -V \sqrt{c^2 - x'^2} \quad (|x'| < c). \quad (44)$$

The pressure acting on the section can be approximated using linear Bernoulli equation as follows:

$$p(x', 0, t) = \rho_w \left(\dot{V} \sqrt{c^2 - x'^2} + V \frac{cc'}{\sqrt{c^2 - x'^2}} \right). \quad (45)$$

The pressure acting on the section is integrated along the wetted beam, yielding the resultant force

$$f^*(x, t) = \int_{-c}^c p(x', 0, t) dx' = \rho_w \frac{\pi}{2} c^2 \dot{V} + \rho_w \pi c \dot{c} V. \quad (46)$$

In this expression, the first term represents the sectional force due to vertical acceleration, while the second term, which is linearly proportional to the vertical velocity, corresponds to the lift force. Although this component is often referred to as a slamming force in the literature, that terminology is intentionally avoided here to prevent ambiguity, as the objective is to compute the instantaneous hydrodynamic force acting on the section, rather than characterize an impact event. Hence, f^* is re-expressed as follows:

$$f^*(x, t) = a \dot{V} + b V, \quad (47)$$

where a and b denote the sectional added mass and lift coefficient, respectively.

Since b is the time derivative of a and a represents the sectional added mass, the sectional force caused by potential flow may be interpreted as arising from the variation of momentum (i.e., the material derivative of aV). It is also important to recall that each section is subjected to a horizontal relative velocity, which gives rise to convective transport. This convective effect introduces an additional term, expressed as

$$f_{ct}(\xi, t) = -U \frac{\partial(aV)}{\partial \xi}, \quad (48)$$

which contributes to the consideration of three-dimensional effects by accounting for momentum exchange along the length of the boat. Finally, nonlinear effects are introduced into the force model through the inclusion of cross-flow drag, represented by

$$f_{cd}(\xi, t) = C_{CD} \rho_w c V^2. \quad (49)$$

As such, the sectional hydrodynamic force is expressed as sum forces introduced above as follows:

$$\begin{aligned} f_{\text{hd}}(\xi, t) &= -(f^*(\xi, t) + f_{ct}(\xi, t) + f_{cd}(\xi, t)) \\ &= -a \dot{V} - b V + U \frac{\partial(aV)}{\partial \xi} - C_{CD} \rho_w c V^2. \end{aligned} \quad (50)$$

The hydrostatic pressure is formulated as follows:

$$f_{hs}(\xi, t) = -\rho_w g c \left(h - \frac{c}{2} \tan \beta \right). \quad (51)$$

For a wet chine condition, a minimal simplification is applied: it is assumed that the spray root does not influence the fluid motion. Consequently,

$$c = B/2 \quad \text{and} \quad \dot{c} = 0. \quad (52)$$

Under this assumption, the sectional hydrodynamic force is computed using Eq. (52); however, the lift term vanishes, as there is no variation in the half-wetted beam. The hydrostatic force of the section is also found as

$$f_{hs}(x, t) = -\rho_w g \frac{B}{2} h_c. \quad (53)$$

B. The second-order 2D+t model

The second-order 2D + t model is developed with the aim of incorporating nonlinearities to the greatest extent practicable and thus differs from the formulation presented in Subsection III A. That is, in contrast to the original model presented in Subsection III A, which is based on linear Airy waves and linearized momentum variation, the present approach introduces second-order Stokes waves and additional or modified terms that can be incorporated into the water-entry model for sectional force estimation, thereby retaining different linear and certain nonlinear terms that are expected to influence damping, slamming loads, and the higher harmonics. In this model, $\dot{\Xi}$ and $\ddot{\Xi}$ are formulated as following:

$$\dot{\Xi} \approx \dot{z}_{CG} \cos \theta - z_{CG} \sin \theta \dot{\theta} - \xi \dot{\theta}, \quad (54)$$

$$\ddot{\Xi} \approx \ddot{z}_{CG} \cos \theta - 2\dot{z}_{CG} \sin \theta \dot{\theta} - z_{CG} \sin \theta \ddot{\theta} - z_{CG} \cos \theta \dot{\theta}^2 - \xi \ddot{\theta}. \quad (55)$$

As seen, additional nonlinear terms are incorporated, allowing the consideration of higher-order nonlinearities. Following a similar approach, $\dot{\chi}$ and $\ddot{\chi}$ are expanded as follows:

$$\dot{\chi} \approx \dot{z}_{CG} \sin \theta + z_{CG} \cos \theta \dot{\theta}, \quad (56)$$

$$\ddot{\chi} \approx \ddot{z}_{CG} \sin \theta + 2\dot{z}_{CG} \cos \theta \dot{\theta} - z_{CG} \sin \theta \dot{\theta}^2 + z_{CG} \cos \theta \ddot{\theta}. \quad (57)$$

The model is developed for second-order Stokes waves. Hence, the free surface deformation is expressed as the sum of first- and second-order components

$$\eta(x, t) = \eta^{(1)} + \eta^{(2)}, \quad (58)$$

where $\eta^{(1)}$ and $\eta^{(2)}$ are presented in Appendix A. The horizontal orbital velocity at the water surface is given by

$$w_x = w_x^{(1)} + w_x^{(2)}, \quad (59)$$

where $w_x^{(1)}$ and $w_x^{(2)}$ are first- and second-order components of the orbital velocity at the water surface and are given in Appendix A. Similarly, the vertical orbital velocity at the water surface is expressed as the sum of first- and second-order components

$$w_z = w_z^{(1)} + w_z^{(2)}, \quad (60)$$

with $w_z^{(1)}$ and $w_z^{(2)}$ given Appendix A. The slope of the free surface is also formulated following the same approach. Hence, it can be written as

$$\nu = \nu^{(1)} + \nu^{(2)}, \quad (61)$$

where $\nu^{(1)}$ and $\nu^{(2)}$ are the first- and second-order components of the water surface slope, respectively, and are presented in Appendix A.

The immersion depth and relative horizontal and vertical velocity at each section are found using second-order nonlinear formulations presented here.

This impulsive speed, $V(\xi, t)$, is equivalent to relative vertical speed at any the 2D section of the boat and is given by

$$V = \left[u - w_x^{(1)} - w_x^{(2)} \right] \sin \theta - z_{CG} \sin \theta \dot{\theta} - \dot{\theta} \xi + \left[\dot{z}_{CG} - w_z^{(1)} - w_z^{(2)} \right] \cos \theta. \quad (62)$$

The immersion depth of the section, which would permit calculation of the its wet, is given by

$$h = \frac{z_{CG} - \xi \sin \theta - \eta^{(1)} - \eta^{(2)}}{\cos \theta - (\nu^{(1)} + \nu^{(2)}) \sin \theta}, \quad (63)$$

where $\nu^{(1)}$ and $\nu^{(2)}$ are the slope of first- and second-order components of the waves.

The potential flow during the dry chine phase is formulated based on the generalized Wagner model, developed by Korobkin,⁶⁰ which extends the classical Wagner theory, which is expressed as follows:

$$\varphi(x', t) \approx -V \sqrt{c^2 - x'^2} - V [\mathcal{F}(x') - h(t) - h_{wp}(t)] \quad |x'| < c. \quad (64)$$

The half-wetted beam of dry chine phase is approximated using the Wagner boundary condition, consistent with the approach adopted in the weakly nonlinear model. Applying Bernoulli's equation, the pressure field around the section under dry chine conditions is approximated as

$$P(x', t) \approx \rho_w \left[\dot{V} \left(\sqrt{c^2 - x'^2} + \mathcal{F}(x') - h(t) - h_{wp} \right) - V h_{wp} \right. \\ \left. + V \frac{\dot{c}c}{\sqrt{c^2 - x'^2}} - V^2 \left(\frac{1}{2} \frac{c^2}{c^2 - x'^2} \frac{1}{1 + \mathcal{F}_{x'}^2} - \frac{1}{2} \frac{\mathcal{F}_{x'}^2}{1 + \mathcal{F}_{x'}^2} \right) \right]. \quad (65)$$

The pressure acting on the section is again integrated along the wall of the section. However, this integral cannot generally be evaluated analytically over the full wetted region, as the terms involving V^2 may diverge and approach $-\infty$ as $x' \rightarrow c$. To address this, the integral is approximated by evaluating the pressure over the reduced interval $-c^* < x' < c^*$, where c^* is a regularization factor introduced to exclude the singular behavior near the spray root. Hence,

$$c^* = \epsilon c \quad \text{and} \quad \epsilon = \sqrt{1 - X^2}, \quad (66)$$

where X is given by

$$X = \frac{\sin(2\beta)}{\pi \left[1 + \sqrt{1 - 4\pi^{-2} \sin^2 \beta (\sin^2 \beta + \pi - 2)} \right]}. \quad (67)$$

The force caused by the pressure then can be expanded as follows:

$$f^*(\xi, t) \approx \rho_w \left(\frac{\pi}{2} c^2 + c^2 \tan \beta - \pi c h \right) \dot{V} \\ + \rho_w \pi c \dot{c} V - \rho_w \pi c \dot{c} \left(1 - \frac{2 \arcsin \epsilon}{\pi} \right) V \\ - \rho_w c \left(\frac{1}{2} \cos^2 \beta \ln \frac{1 + \epsilon}{1 - \epsilon} + \epsilon (\sin^2 \beta + \pi - 2) \right) V^2. \quad (68)$$

As seen in (68), the sectional force arising from the hydrodynamic pressure around the two-dimensional section consists of three distinct components. The first corresponds to inertial terms, representing the contribution of added mass. The second represents the linear lift force, and the third comprises nonlinear lift components, which arise from terms proportional to V^2 . These nonlinear terms result from the evaluation of the pressure integral over the truncated domain $-c^* < x' < c^*$. Accordingly, the sectional force can be re-expressed as

$$f^*(\xi, t) \approx a\dot{V} + b^{(1)}V + b^{(2)}V^2. \quad (69)$$

Here, terms $b^{(1)}$ and $b^{(2)}$ are intentionally distinguished using superscripts (1) and (2), respectively, to mathematically represent the linear and nonlinear contributions to the sectional force arising from the hydrodynamic pressure. Similar to approach used in development of the weakly nonlinear model, a convection term is introduced that considers the three-dimensional effects. This term is similar to that of the weakly nonlinear model and is given in Eq. (48). More importantly, an additional nonlinear term is included, referred to as the edge force. This term reflects a second-order nonlinearity and represents the contribution of the outer region during a dry chine phase, given by

$$f_{ed}(\xi, t) = b^{**}V^2, \quad (70)$$

where b^{**} is the coefficient of the nonlinear quadratic term associated with the outer-region force, estimated as

$$b^{**} = -2\rho_w c. \quad (71)$$

This additional force is a second-order correction to the outer-region pressure near the chine and is introduced to capture the reduction in hydrodynamic lift observed during the dry chine phase. The formulation is inspired from the second-order water-entry models of Korobkin⁶¹ and Oliver⁶² where the outer solution exhibits a linear dependence on the wetted half-beam. It should be noted that $f_{ed}(\xi, t)$ is not derived from a theoretical formulation. Rather, it was introduced empirically. The hydrodynamic force acting on the section is then formulated as

$$\begin{aligned} f_{hd}(\xi, t) &= -(f^*(\xi, t) + f_{ed}(\xi, t) + f_{cd}(\xi, t) + f_{ct}(\xi, t)) \\ &= -a\dot{V} - b^{(1)}V - b^{(2)}V^2 - b^{**}V^2 + U \frac{\partial(aV)}{\partial\xi} - C_{CD}\rho_w cV^2. \end{aligned} \quad (72)$$

As seen, three nonlinear quadratic terms appear in Eq. (72), among which the term $b^{(2)}$ is relatively large and is found to contribute an additional damping force, particularly over dry chine region (see the Appendix C). Therefore, in the present calculations, this quadratic term is set to zero.

The hydrostatic pressure is calculated by integrating pressure over the wet surface in the vertical direction, i.e., over $h^\dagger = -h$ to $h^\dagger = h_{wp}$,

$$f_{hs}(\xi, t) = -2\rho_w g \int_{-h_{wp}}^h h^\dagger \frac{dh^\dagger}{\tan(\beta)}. \quad (73)$$

The above integral yields in

$$f_{hs}(\xi, t) = -\frac{\rho_w g}{\tan(\beta)}(h^2 - h_{wp}^2). \quad (74)$$

This integration can be found in the work of Fairlie-Clarke and Tveitnes.¹¹⁷ If the chine becomes wetted, the same procedure as in the weakly nonlinear model is applied, whereby c is set equal to $B/2$ and its time derivative is set to zero. An alternative approach, proposed by Tassin *et al.*,¹¹⁸ introduces a fictitious spray-root location and applies a zero-pressure condition at the chine. In this formulation, \dot{c} is non-zero for sections with a wetted chine, and c exceeds $B/2$. This method is presented in Appendix B. This method was tested in the present study, but it was found to produce excessive damping forces, with resonance not being captured. As such, the method was seen to underpredict the heave and pitch RAOs (see Appendix C). The likely reason is that the approach of Tassin *et al.*¹¹⁸ was developed for short-duration water-entry problems involving cavity formation, rather than for periodic seakeeping motions.

The force resulting from hydrostatic pressure after flow separation at the chine is also calculated by integrating the pressure along the depth. However, it is assumed that the water does not hypothetically reattach to the side walls above the chine. This assumption is physically reasonable, as the spray leaving the chine does not typically return toward the hull surface. Nonetheless, this may become a point of concern in scenarios involving twin wedges entering the water under asymmetric conditions, where reattachment could occur on one side. Accordingly, the hydrostatic pressure acting on the hull surface after flow separation is calculated as

$$f_{hs}(\xi, t) = -\frac{\rho_w g}{\tan(\beta)}(h_c^2 + 2h_c(h - h_c)). \quad (75)$$

C. Time domain simulations

Either of the models used for solving the problem and calculating the related force, it can be shown that the forces can be re-written as

$$F^* = F^* - F^a \quad \text{and} \quad M^* = M^* - M^a. \quad (76)$$

Here, F^a and M^a are added mass vertical forces and pithing moments caused by heave and pitch accelerations, given by

$$F^a = m_{zz}\ddot{z}_{CG} + m_{3z0}\ddot{\theta} \quad \text{and} \quad M^a = m_0\ddot{z}_{CG} + m_{00}\ddot{\theta}. \quad (77)$$

m_{zz} , m_{z0} , m_{0z} , and m_{00} are integrals of the sectional added mass forces along the length of the boat and represent the nonlinear added mass coefficients. These coefficients are expressed as follows:

$$\begin{aligned} m_{zz} &= I_0 \cos^2 \theta, & m_{z0} &= -I_1 \cos \theta, \\ m_{0z} &= -I_1 \cos \theta, & m_{00} &= I_2. \end{aligned} \quad (78)$$

Here, I_i denotes the i th order integral of a along the ship, that is,

$$I_0 = \int_L a d\xi, \quad I_1 = \int_L \xi a d\xi, \quad I_2 = \int_L \xi^2 a d\xi. \quad (79)$$

Accordingly, the motion equations are established as

$$\begin{aligned} (m + m_{zz})\ddot{z}_{CG} + m_{z0}\ddot{\theta} &= F^* + mg, \\ m_{0z}\ddot{z}_{CG} + (I_{yy} + m_{00})\ddot{\theta} &= M^*. \end{aligned} \quad (80)$$

To solve the problem over time, the state vector is defined as

$$\mathbf{y}(t) = \begin{bmatrix} \dot{z}_{CG}(t) & \dot{\theta}(t) & z_{CG}(t) & \theta(t) \end{bmatrix}^T. \quad (81)$$

As such, the equations of the rigid-body motion can be written in first-order form as

$$\mathbf{f}(t, \mathbf{y}) = \begin{bmatrix} [\mathbf{M}^{-1}\mathbf{F}^*]_1 & [\mathbf{M}^{-1}\mathbf{F}^*]_2 & y_1 & y_2 \end{bmatrix}^T, \quad (82)$$

where \mathbf{M} is the mass matrix of the boat, which includes the mass, moment of inertia, and the added mass coefficients. \mathbf{F}^* is a vector containing the fluid forces, excluding the added mass forces and the weight force. \mathbf{M} and \mathbf{F}^* are given by

$$\mathbf{M} = \begin{bmatrix} m + m_{zz} & m_{z\theta} \\ m_{\theta z} & I_{yy} + m_{\theta\theta} \end{bmatrix}, \quad \text{and} \quad \mathbf{F}^* = \begin{bmatrix} F^* + mg \\ M^* \end{bmatrix}. \quad (83)$$

The Runge–Kutta–Merson method is used to solve the problem in the time domain.

IV. FULLY NONLINEAR CFD MODEL

The fully nonlinear model is developed within a three-dimensional computational domain $\Omega_F \subset \mathbb{R}^3$, bounded by six surfaces ($\Gamma_F \subset \partial\Omega_F$), in which a rigid body is placed and allowed to undergo heave and pitch motions. This differs from the classical strip theory approach, which is commonly referred to as a two-dimensional modeling framework in naval architecture community. This three-dimensional domain is hypothetically filled with a mixture of gas and liquid, representing air and water, which are assumed to be miscible. This domain is shown in Fig. 3.

The entire fluid is considered viscous and Newtonian, with surface tension effects neglected. By introducing $\mathbf{v} = (v_x, v_y, v_z)$ as the velocity field, ρ_e as the effective density, μ_e as the effective kinematic viscosity, RANS equations governing the incompressible air–water fluid motion around the vessel can be expressed as

$$\int_{\Gamma_F} \mathbf{v} \cdot \mathbf{n} dA = 0 \quad (84)$$

and

$$\begin{aligned} \frac{d}{dt} \int_{\Omega_F} \rho_e \mathbf{v} dV + \int_{\Gamma_F} \rho_e \mathbf{v} (\mathbf{v} \cdot \mathbf{n}) dA \\ = - \int_{\Gamma_F} p \mathbf{n} dA + \int_{\Gamma_F} \boldsymbol{\tau}_e \cdot \mathbf{n} dA + \int_{\Omega_F} \rho_e \mathbf{g} dV. \end{aligned} \quad (85)$$

In above, $\mathbf{g} = (9.81, 0, 0)$ represents the gravitational acceleration vector, $\boldsymbol{\tau}_e$ denotes the viscous shear stress tensor, and \mathbf{R} is the Reynolds stress tensor. These are defined as follows:

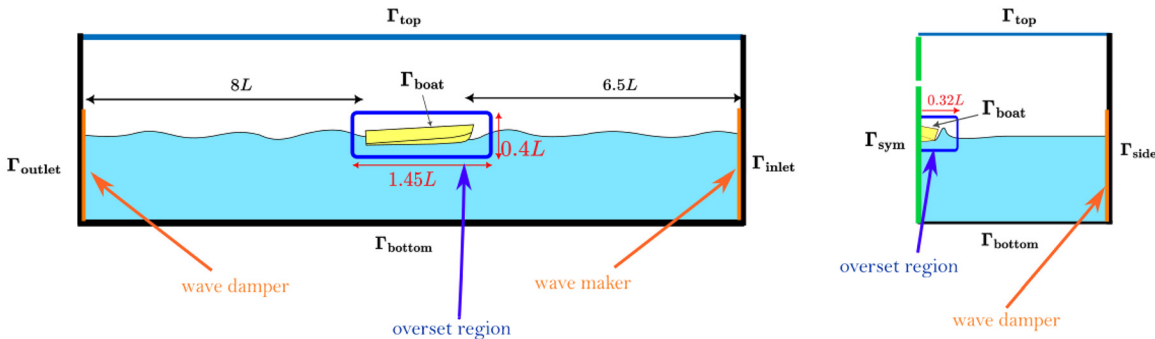


FIG. 3. The three-dimensional computational domain used to solve the fluid motion around the planing hull, coupled with the DBFI solver. Longitudinal and front views of the domain are shown. The overset region is highlighted by a blue box, while the numerical wavemaker and wave dampers are indicated by orange arrows. A symmetry boundary condition is applied, so the front view is mirrored from the side view about the centerline of the hull.

$$\begin{aligned} \boldsymbol{\tau}_e &= \mu_e \left(\nabla \mathbf{v} + (\nabla \mathbf{v})^T \right) - \frac{2}{3} \mu_e (\nabla \cdot \mathbf{v}) \mathbf{I}, \quad \text{and} \\ \mathbf{R} &= \rho_e \bar{\mathbf{v}} \bar{\mathbf{v}}' \approx -\mu_t \left(\nabla \mathbf{v} + (\nabla \mathbf{v})^T \right) + \frac{2}{3} \rho_e \kappa \mathbf{I}. \end{aligned} \quad (86)$$

Here, μ_t is the eddy viscosity and κ is the turbulence kinetic energy. The eddy viscosity μ_t is calculated using the $k-\omega$ SST turbulence model, which is denoted as the $\kappa-\omega$ model in the present study to avoid confusion with the wave number k and the angular wave frequency ω . μ_t is calculated as

$$\mu_t = \frac{\rho_e \kappa}{\omega}. \quad (87)$$

κ and ω are related to each other through the set of equations

$$\begin{aligned} \frac{d}{dt} \int_{\Omega_F} \rho_e \kappa dV + \int_{\Gamma_F} \rho_e \kappa \mathbf{v} \cdot \mathbf{n} dA \\ = \int_{\Omega_F} P_\kappa dV - \int_{\Omega_F} \mathcal{R}_3 \rho_e \kappa \omega dV + \int_{\Gamma_F} (\mu_e + \sigma_\kappa \mu_t) \nabla \kappa \cdot \mathbf{n} dA, \end{aligned} \quad (88)$$

$$\begin{aligned} \frac{d}{dt} \int_{\Omega_F} \rho_e \omega dV + \int_{\Gamma_F} \rho_e \omega \mathbf{v} \cdot \mathbf{n} dA = \int_{\Omega_F} \mathcal{R}_1 \frac{\omega}{\kappa} P_\kappa dV \\ - \int_{\Omega_F} \mathcal{R}_2 \rho_e \omega^2 dV + \int_{\Gamma_F} (\mu_e + \sigma_\omega \mu_t) \nabla \omega \cdot \mathbf{n} dA. \end{aligned} \quad (89)$$

P_κ is the production rate of turbulent kinetic energy. The coefficients \mathcal{R}_1 , \mathcal{R}_2 , and \mathcal{R}_3 govern the production of ω , the dissipation of ω , and the dissipation of κ . σ_κ and σ_ω are turbulent Prandtl numbers associated with the diffusive transport of κ and ω .

The air–water mixture is modeled using the volume-of-fluid (VOF) method.¹¹⁹ A scalar field $C \in [0, 1]$ parameter is introduced as another field, which helps model the air–water mixing at any control volume. The lower limit $C = 0$ corresponds to pure air, and the upper limit $C = 1$ corresponds to pure water. The spatial and temporal evolution of C is governed by a conservation equation, which is expressed as

$$\frac{d}{dt} \int_{\Omega_F} C dV + \int_{\Gamma_F} C \mathbf{v} \cdot \mathbf{n} dA = 0. \quad (90)$$

Effective values of density and dynamic viscosity are obtained by weighting the corresponding properties of air and water using the volume fraction value C , as

$$\rho_e = C\rho_{\text{water}} + (1 - C)\rho_{\text{air}}, \quad (91)$$

$$\mu_e = C\mu_{\text{water}} + (1 - C)\mu_{\text{air}}. \quad (92)$$

The right boundary of the fluid domain is defined as the inlet, $\Gamma_{\text{inlet}} \subset \partial\Omega_F$, on which a velocity inlet boundary condition with incoming waves generated by a numerical wave maker is imposed. Accordingly, the velocity at the inlet is given by $\mathbf{v} = \mathbf{v}_{\text{ship}} + \mathbf{v}_{\text{wave}}$, where $\mathbf{v}_{\text{ship}} = (-u, 0, 0)$. As such, the boundary condition on Γ_{inlet} can be mathematically written as

$$\begin{aligned} \mathbf{v} &= \mathbf{v}_{\text{ship}} + \mathbf{v}_{\text{wave}}, \\ C &= \begin{cases} 1, & z < \eta(x, t), \\ 0, & z \geq \eta(x, t), \end{cases} \\ \kappa &= \kappa_{\text{inlet}}, \varpi = \varpi_{\text{inlet}}, \\ \frac{\partial p}{\partial \mathbf{n}}|_{\Gamma_{\text{inlet}}} &= 0, \forall x \in \Gamma_{\text{inlet}}, \quad t > 0. \end{aligned} \quad (93)$$

An inlet velocity boundary condition is set on the left part of the domain, referred to as the side boundary $\Gamma_{\text{side}} \subset \partial\Omega_F$, on which the following condition is satisfied:

$$\begin{aligned} \mathbf{v} &= \mathbf{v}_{\text{ship}}, \quad \frac{\partial C}{\partial \mathbf{n}} = 0, \quad \kappa = \kappa_{\text{side}}, \quad \varpi = \varpi_{\text{side}}, \\ \frac{\partial p}{\partial \mathbf{n}}|_{\Gamma_{\text{side}}} &= 0, \quad \forall x \in \Gamma_{\text{side}}, \quad t > 0. \end{aligned} \quad (94)$$

The domain is defined to be symmetric, as the waves are unidirectional and the vessel exhibits neither antisymmetric nor asymmetric behavior, as previously described in Sec. II. Accordingly, a symmetry boundary $\Gamma_{\text{sym}} \subset \partial\Omega_F$ is introduced, across which no flow penetration occurs, and all other fields are subject to Neumann boundary conditions. Hence, the boundary condition on Γ_{sym} is mathematically represented by

$$\begin{aligned} \mathbf{v} \cdot \mathbf{n} &= 0, \quad \frac{\partial \mathbf{v}_{\parallel}}{\partial \mathbf{n}} = 0, \quad \frac{\partial C}{\partial \mathbf{n}} = 0, \quad \frac{\partial \kappa}{\partial \mathbf{n}} = 0, \\ \frac{\partial \varpi}{\partial \mathbf{n}} &= 0, \quad \frac{\partial p}{\partial \mathbf{n}} = 0, \quad \forall x \in \Gamma_{\text{sym}}, \quad t > 0. \end{aligned} \quad (95)$$

The upper patch of the domain, $\Gamma_{\text{top}} \subset \partial\Omega_F$, is intentionally prescribed as a velocity inlet, which is mathematically represented by

$$\begin{aligned} \mathbf{v} &= \mathbf{v}_{\text{ship}}, \quad C = 0, \quad \kappa = \kappa_{\text{top}}, \quad \varpi = \varpi_{\text{top}}, \\ \frac{\partial p}{\partial \mathbf{n}}|_{\Gamma_{\text{top}}} &= 0, \quad \forall x \in \Gamma_{\text{top}}, \quad t > 0. \end{aligned} \quad (96)$$

An outlet surface on the left side of the computational domain, $\Gamma_{\text{outlet}} \subset \partial\Omega_F$, is defined through which the fluid exits the domain. To facilitate this, an outlet pressure condition is applied, enabling a zero-gradient condition for velocity. Accordingly, the boundary condition is expressed as follows:

$$\begin{aligned} \frac{\partial \mathbf{v}}{\partial \mathbf{n}} &= 0, \quad \frac{\partial C}{\partial \mathbf{n}} = 0, \quad \frac{\partial \kappa}{\partial \mathbf{n}} = 0, \\ \frac{\partial \varpi}{\partial \mathbf{n}} &= 0, \quad p = p_{\text{outlet}}, \quad \forall x \in \Gamma_{\text{outlet}}, \quad t > 0. \end{aligned} \quad (97)$$

A moving wall boundary condition is applied on the wall of the planing buoy $\Gamma_{\text{boat}} \subset \partial\Omega_F$,

$$\begin{aligned} \mathbf{v} &= \mathbf{v}_{\text{wall}}^{\text{DFBI}}, \quad \frac{\partial C}{\partial \mathbf{n}} = 0, \quad \frac{\partial \kappa}{\partial \mathbf{n}}|_{\Gamma_{\text{boat}}} = 0, \\ \varpi &= \frac{u_{\tau}^2}{\nu_e}, \quad \frac{\partial p}{\partial \mathbf{n}} \Big|_{\Gamma_{\text{boat}}} = 0, \quad \forall x \in \Gamma_{\text{boat}}, \quad t > 0. \end{aligned} \quad (98)$$

Here, $\mathbf{v}_{\text{wall}}^{\text{DFBI}}$ is the dynamic fluid–body interaction velocity given by

$$\mathbf{v}_{\text{wall}}^{\text{DFBI}}(\mathbf{x}, t) = \mathbf{V}_c(t) + \boldsymbol{\Theta}(t) \times (\mathbf{x} - \mathbf{x}_{CG}(t)). \quad (99)$$

where $\mathbf{V}_c(t)$ is the translational velocity of the center of mass and $\boldsymbol{\Theta}(t)$ is the angular velocity vector. $\mathbf{x}_{CG}(t)$ is the position of the center of gravity. On the bottom surface ($\Gamma_{\text{bottom}} \subset \partial\Omega_F$) of the three-dimensional domain, a velocity inlet boundary condition is imposed, satisfying

$$\begin{aligned} \mathbf{v} &= \mathbf{v}_{\text{ship}}, \quad C = 1, \quad \kappa = \kappa_{\text{bottom}}, \quad \varpi = \varpi_{\text{bottom}}, \\ \frac{\partial p}{\partial \mathbf{n}} \Big|_{\Gamma_{\text{bottom}}} &= 0, \quad \forall x \in \Gamma_{\text{bottom}}, \quad t > 0, \end{aligned} \quad (100)$$

which is prescribed.

The specific turbulence dissipation rate ϖ in the vicinity of the wall of the boat is calculated by embarking a two-layer all y^+ wall treatment. This method adapts to the local mesh resolution near the wall of the hull by blending between low and high y^+ formulations.

The dimensionless wall distance y^+ is defined as follows:

$$y^+ = \frac{y v_{\tau}}{\nu_e}, \quad (101)$$

in which y is the wall-normal distance to the first cell center and v_{τ} is the friction velocity.

Using a blending function F_2 to smoothly transition between the viscous sublayer and the logarithmic region, the model predicts ϖ as

$$\varpi = F_2 \cdot \frac{6\nu_e}{\beta_1 y^2} + (1 - F_2) \cdot \frac{(y^+)^2 \nu_e}{y^2}. \quad (102)$$

Here, $\beta_1 \approx 0.075$ is a constant, and the blending function F_2 is given by

$$F_2 = \tanh \left(\left[\max \left(\frac{2\sqrt{\kappa}}{\beta^* \omega y}, \frac{500\nu_e}{y^2 \omega} \right) \right]^2 \right). \quad (103)$$

This approach is believed to be suitable for simulating turbulent flow regimes around the moving boundaries of a ship or boat exposed to water waves. An example of the y^+ distribution on the bottom of the planing hull studied in this work is shown in Fig. 4. The summary of the considered boundary conditions is outlined in Table I.

The waves may be reflected from Γ_{side} and Γ_{outlet} . To mitigate this, virtual wave damping is applied near these boundaries. Damping is implemented by artificially attenuating the momentum source term in the vicinity of the boundary as

$$\mathbf{S}_v(x) = -\alpha_{\text{damp}}(x)(\mathbf{v}(x, t) - \mathbf{v}_{\text{ref}}(x)), \quad (104)$$

where $\mathbf{v}_{\text{ref}} = \mathbf{0}$ and α_{damp} is a spatially varying damping coefficient. The waves at Γ_{inlet} are generated using fifth-order Stokes theory, the formulation of which is omitted here for brevity (see Ref. 55 for more technical information).

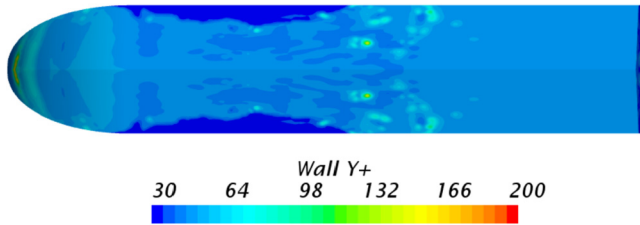


FIG. 4. Example distribution of y^+ on the bottom surface of the tested planing hull introduced in Sec. V.

The mesh motion of the vessel within the computational domain is modeled using the overset method, which requires the definition of an overset region. A linear interpolation between the background mesh and the overset mesh is performed as

$$\phi_{\text{fringe}} = \sum_{i=1}^N w_i \phi_{\text{donor},i}, \quad \sum_{i=1}^N w_i = 1, \quad \phi \in \{\mathbf{v}, p, \alpha, \kappa, \varpi\}. \quad (105)$$

The fluid force and moment vectors acting on the boat are calculated as

$$\mathbf{F} = \int_{\Gamma_{\text{boat}}} (-p\mathbf{n} + \boldsymbol{\tau} \cdot \mathbf{n}) dA, \quad (106)$$

$$\mathbf{M} = \int_{\Gamma_{\text{boat}}} (\mathbf{x} - \mathbf{x}_{\text{CG}}) \times (-p\mathbf{n} + \boldsymbol{\tau} \cdot \mathbf{n}) dA. \quad (107)$$

Here, $\mathbf{F} = (F_x, F_y, F_z)$ and $\mathbf{M} = (M_x, M_y, M_z)$. The component F_z represents the fluid force in the heave direction and corresponds to F^* in Eq. (3). Similarly, M_y denotes the pitch moment induced by fluid pressure and shear stresses, and corresponds to M^* .

TABLE I. Summary of boundary conditions applied in the fluid domain.

Boundary	\mathbf{v}	C	κ	ϖ	p
Γ_{inlet}	$\mathbf{v}_{\text{ship}} + \mathbf{v}_{\text{wave}}$	$C = \begin{cases} 1, & z < \eta(x, t) \\ 0, & z \geq \eta(x, t) \end{cases}$	κ_{inlet}	ϖ_{inlet}	$\frac{\partial p}{\partial \mathbf{n}} \Big = 0$
Γ_{side}	\mathbf{v}_{ship}	$\frac{\partial C}{\partial \mathbf{n}} = 0$	κ_{side}	ϖ_{side}	$\frac{\partial p}{\partial \mathbf{n}} \Big = 0$
Γ_{sym}	$\mathbf{v} \cdot \mathbf{n} = 0, \frac{\partial \mathbf{v}_{\parallel}}{\partial \mathbf{n}} = 0$	$\frac{\partial C}{\partial \mathbf{n}} = 0$	$\frac{\partial \kappa}{\partial \mathbf{n}} = 0$	$\frac{\partial \varpi}{\partial \mathbf{n}} = 0$	$\frac{\partial p}{\partial \mathbf{n}} \Big = 0$
Γ_{top}	\mathbf{v}_{ship}	$C = 0$	κ_{top}	ϖ_{top}	$\frac{\partial p}{\partial \mathbf{n}} \Big = 0$
Γ_{bottom}	\mathbf{v}_{ship}	$C = 1$	κ_{bottom}	ϖ_{bottom}	$\frac{\partial p}{\partial \mathbf{n}} \Big = 0$
Γ_{outlet}	$\frac{\partial \mathbf{v}}{\partial \mathbf{n}} = 0$	$\frac{\partial C}{\partial \mathbf{n}} = 0$	$\frac{\partial \kappa}{\partial \mathbf{n}} = 0$	$\frac{\partial \varpi}{\partial \mathbf{n}} = 0$	$p = p_{\text{outlet}}$
Γ_{boat}	$\mathbf{v} = \mathbf{v}_{\text{wall}}^{\text{DFBI}}$	$\frac{\partial C}{\partial \mathbf{n}} = 0$	$\frac{\partial \kappa}{\partial \mathbf{n}} \Big = 0$	$\varpi = \frac{u_{\tau}^2}{\nu_e}$	$\frac{\partial p}{\partial \mathbf{n}} \Big = 0$

To solve all governing equations, the computational domain is first generated, and a computer-aided design (CAD) file of the boat is inserted. The domain is defined with dimensions of $15.5L \times 5L \times 6L$, and the boat is placed within an overset region of dimensions $1.5L \times 0.34L \times 0.42L$. Then, a surface mesh is generated using the Surface Remesher, which cleans the geometry and generates high-quality surface elements. Following this, the Trimmed Cell Mesher is applied to create a hexahedral-dominant mesh with cut cells, and the Prism Layer Mesher tool is used to add boundary layer cells near the wall of the vessel. To mesh the fluid domain, volumetric controls are applied to refine the cell size in specific regions, such as near the water surface and the hull wall. The height of the prism layers is also adjusted based on the desired turbulence resolution, targeting a specific y^+ value. The meshing is performed by using a CFD code, namely, STAR-CCM+ 22.10 (17.02.007-R8).¹²⁰ The generated mesh is shown in Fig. 5. The final mesh size was chosen following a mesh study, presented in Appendix D.

The fluid motion equations are solved using the same CFD code. An implicit unsteady RANS model is employed, and the SIMPLE (Semi-Implicit Method for Pressure-Linked Equations) algorithm is utilized to solve the equations in both space and time. The air-water interface is tracked using the HRIC (High-Resolution Interface Capturing) approach. A segregated flow solver is used, and temporal discretization is performed using a second-order scheme. The convection terms in both the momentum and turbulence equations are discretized using second-order accurate methods. Up to five iterations are performed per time step, and ten iterations are executed for the 6DOF motion solver within each inner iteration. The time step for the simulations is set as

$$\delta t_{\text{CFD}} \approx 0.0045 \frac{L}{u}. \quad (108)$$

The above expression is a general guideline recommended by the ITTC for CFD modeling of ship-related problems.¹²¹ The summary of

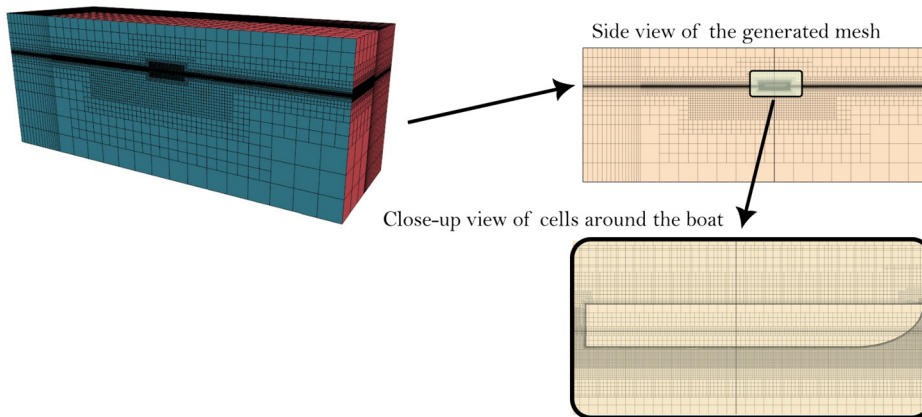


FIG. 5. Generated mesh around the planing hull advancing in waves. Shown are three-dimensional and longitudinal views of the mesh, together with a close-up view around the hull.

the setup for the CFD model is presented in [Table II](#), and the algorithm used for solving the problem is shown in [Fig. 6](#).

V. TESTED CASES

In the present study, one of the academic planing hulls originally tested by Frijdsma²⁰ is selected as the reference geometry. This hull, with its prismatic form, is particularly well-suited for analysis using the

$2D + t$ model. Hence, it is widely considered as a canonical test case in academic investigations. Moreover, extensive experimental data are available for this hull. This includes dynamic responses of the hull in both regular and irregular waves over a broad range of wavelengths

TABLE II. Summary of simulation setup and numerical methods.

Aspect	Description
Computational domain	$15.5L \times 5L \times 6L$
Overset region	$1.5L \times 0.34L \times 0.42L$ (around the boat)
CAD geometry	Imported boat CAD file
Mesh type	Hexahedral-dominant mesh with cut cells
Mesh generation	Surface Remesher, Trimmed Cell Mesher, Prism Layer Mesher
Mesh refinement	Volumetric controls near water surface and hull wall
Prism layers	Height adjusted to achieve target y^+
CFD code	STAR-CCM+ 22.10 (17.02.007-R8)
Solver type	Implicit unsteady RANS, segregated flow solver
Pressure–velocity coupling	SIMPLE algorithm
Interface capturing	HRIC (High-Resolution Interface Capturing)
Temporal discretization	Second-order implicit
Spatial discretization	Second-order accurate for convection terms (momentum and turbulence)
Iterations	Up to 5 per time step; 10 for 6DOF motion solver (inner loop)
Time step size	$\delta t_{CFD} \approx 0.0045 L/u$ (ITTC guideline)

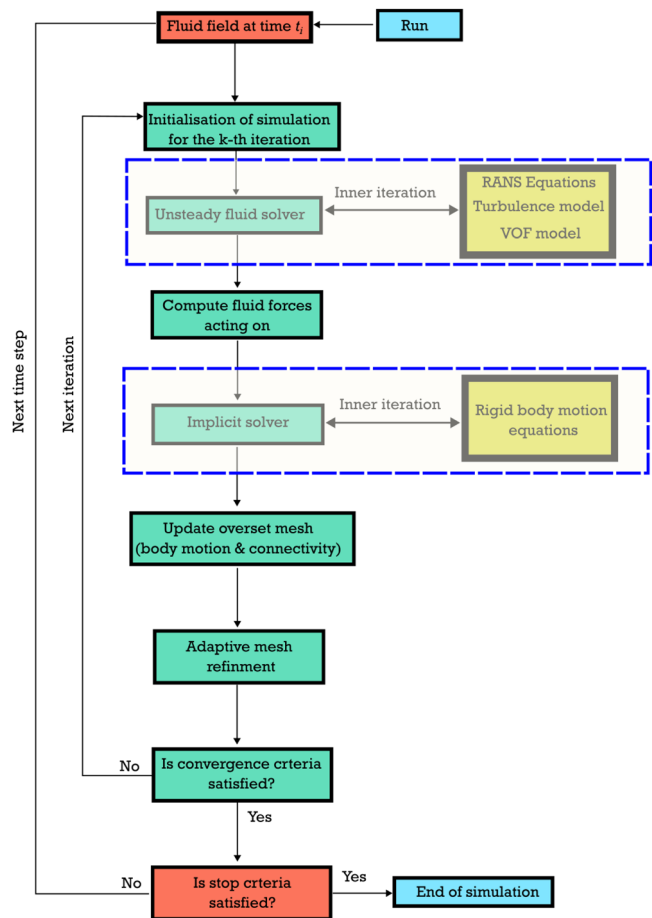


FIG. 6. The algorithm used for solving the motions of planing hull exposed to water waves using the CFD model.

TABLE III. Principal particulars of the studied planing hull.²⁰

Main particular	Value
L (m)	1.143
L/B (-)	5
β ($^{\circ}$)	20
C_{Δ}	0.608
L_{CG}/L at $F_B = 2.65$	0.41
L_{CG}/L at $F_B = 4.0$	0.38
K_{yy}/L	0.25

and speeds, which aids in validating the model. The hull has also been tested in calm-water conditions, with recorded running trim angles, sinkage, mean wetted length, and resistance across a wide speed spectrum. The hull examined in the present study has a deadrise angle of $\beta = 20^{\circ}$ and a length-to-beam ratio of $L/B = 5$. The length of hull is ≈ 1.14 m. The deadrise angle is constant along the hull length. The beam is also constant over approximately $0.8L$, measured forward from the transom, and the keel line is flat over the same region. The non-flat portion of the keel is represented geometrically as

$$\left(\frac{X}{0.228}\right)^2 + \left(\frac{8Y}{1.143}\right)^2 = 1. \quad (109)$$

Its principal characteristics are summarized in Table III. The body profile of this hull is shown in Fig. 7.

Two sets of tests are performed on this hull. The first set is conducted to validate the models and to compare their relative accuracy. These tests numerically replicate the towing tank experiments originally carried out by Fridsma.²⁰ These tests are conducted at two different Froude numbers, $F_B \approx 2.65$ and $F_B \approx 4.0$. Six different wavelengths of $\lambda/L = 1$, $\lambda/L = 1.5$, $\lambda/L = 2$, $\lambda/L = 3$, $\lambda/L = 4$, and $\lambda/L = 6$ are considered. One similar wave height is considered for all wavelength. Hence, wave steepness across different wavelengths is different. It is important to note that²⁰ performed his experiments by keeping the wave height-to-beam ratio (H/B) constant, rather than maintaining a constant wave steepness. The summary of these waves is presented in Table IV

The second set of tests is performed to investigate the effects of wave steepness on the motions of planing hulls in regular waves. These tests are specifically designed to address the second objective of this

TABLE IV. Waves used for running the validation cases, identical to those tested by Fridsma.²⁰ The parameters include wavelength ratio λ/L , wave number k , non-dimensional wave period $T\sqrt{g/B}$, encounter wave period $T_e\sqrt{g/B}$ for $F_B \approx 2.65$ and $F_B \approx 4.0$, wave height ratio H/B , and the corresponding steepness ε .

λ/L	k (rad/m)	$T\sqrt{g/B}$	$T_e\sqrt{g/B}$			
			$F_B \approx 2.65$	$F_B = 4.0$	H/B	ε
1	5.49	5.61	1.40	1.02	0.11	0.07
1.5	3.66	6.87	1.99	1.47	0.11	0.05
2	2.75	7.93	2.54	1.90	0.11	0.03
3	1.83	9.71	3.56	2.70	0.11	0.02
4	1.37	11.21	4.49	3.46	0.11	0.02
6	0.92	13.73	6.18	4.85	0.11	0.01

study, namely to understand the physics of planing motion in waves, and to examine how wave steepness influences the dynamic response of planing hulls advancing in monochromatic waves. The tests are carried out at two Froude numbers, $F_B \approx 2.65$ and $F_B \approx 4.0$, using the same six wavelengths as those considered in the first test set. For each wavelength, three different wave steepness values are considered: $\varepsilon \approx 0.04$, $\varepsilon \approx 0.07$, and $\varepsilon \approx 0.1$. The summary of these tests is listed in Table V.

All runs outlined in both tables are performed using the two-dimensional strip theory models and the three-dimensional CFD model. The nonlinear strip theory models formulate the problem for a fluid domain under far-field boundary conditions, as the impact models solve a water-entry problem with no side walls. The three-dimensional model, however, is bounded by surfaces and solves the problem with the prescribed boundary conditions (velocity inlets on the side, bottom, and front faces, and an outlet at the back face), which represents the closest practical setup to far-field conditions. It is important to emphasize that the size of the computational domain is chosen carefully to minimize any backflow or blockage effects that may occur within the fluid domain.

VI. MODEL PREDICTIONS AGAINST EXPERIMENTS

Predictions from all three models are compared against the measured data from the tank tests of Fridsma,²⁰ using the cases outlined in Table IV. This comparison provides an assessment of the accuracy of each model across different frequency ranges. Representative time

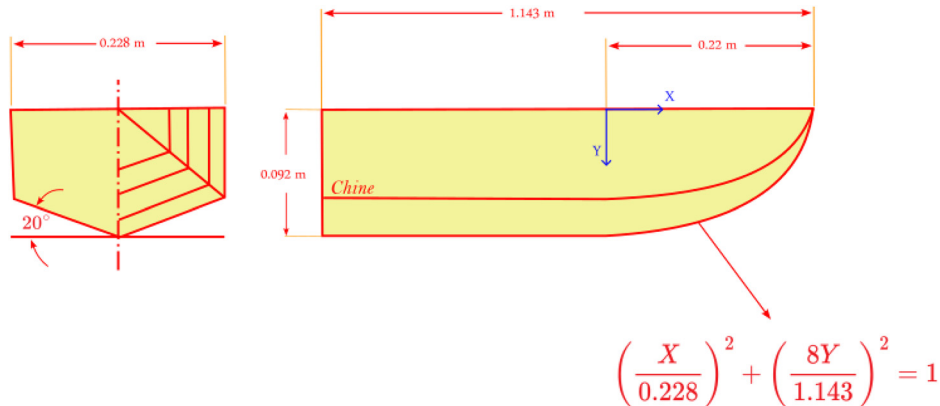
**FIG. 7.** Body profile of the Fridsma hull with $L/B = 5$ and $\beta = 20^{\circ}$.

TABLE V. Waves used in the parametric study of wave steepness effects on the dynamic responses of the planing hull. Cases were run with all three models (CFD, weakly nonlinear $2D+t$, and second-order $2D+t$). The table lists wavelength ratio λ/L , wave number k , non-dimensional wave period $T\sqrt{g/B}$, encounter period $T_e\sqrt{g/B}$ for $F_B \approx 2.65$ and $F_B \approx 4.0$, and the corresponding wave height ratio H/B .

λ/L	k (rad/m)	$T\sqrt{g/B}$	$T_e\sqrt{g/B}$		H/B at different ε		
			$F_B \approx 2.65$	$F_B \approx 4.0$	$\varepsilon \approx 0.04$	$\varepsilon \approx 0.07$	$\varepsilon \approx 0.1$
1	5.49	5.61	1.40	1.02	0.06	0.11	0.16
1.5	3.66	6.87	1.99	1.47	0.09	0.17	0.24
2	2.75	7.93	2.54	1.90	0.13	0.22	0.32
3	1.83	9.71	3.56	2.70	0.19	0.33	0.48
4	1.37	11.21	4.49	3.46	0.25	0.45	0.63
6	0.92	13.73	6.18	4.85	0.38	0.67	0.95

histories of the heave and pitch responses of the vessel advancing at a Froude number of 4.0 and $\lambda/L = 4.0$ are presented in Fig. 8. The upper panels show the results obtained from the fully nonlinear CFD simulations, while the second and third rows present those from the weakly nonlinear and second-order nonlinear models, respectively. A broadly similar harmonic behavior in the heave and pitch response curves is observed across all models, with the results of the $2D+t$ model being particularly close to one another. Evidently, the time histories of both motions predicted by all models display ten cycles over a duration of $10T_e$, confirming that all four models capture the underlying physics and the possible Doppler shift when the vessel operates in head-

sea conditions. In addition, it can be seen that the heave and pitch responses exhibit asymmetric behavior, confirming the nonlinear nature of the motion. This will be discussed in more detail in Secs. VII–X of the paper. The time history of the vertical acceleration predicted by all three models is observed to show a similar pattern, exhibiting highly nonlinear behavior. The weakly nonlinear model, however, produces larger upward accelerations.

The amplitude of heave and pitch motions, regardless of nonlinearity that may appear in the signal of the motion, is found by using a zero-crossing method, which is calculated for a time period of $> 10T_e$. Heave amplitude is normalized using $H/2$, and pitch amplitude is normalized using ε .

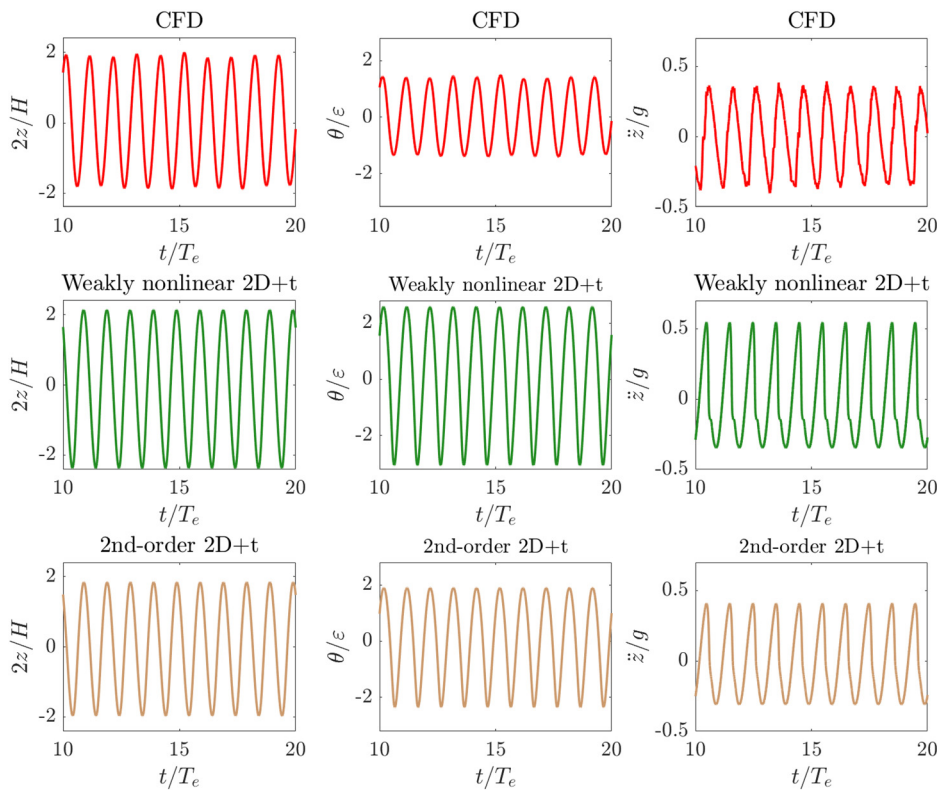


FIG. 8. Sample time histories of heave response (left column), pitch response (middle column), and vertical acceleration at CG (right column) of the planing hull in regular waves obtained using the CFD model (upper row), the weakly nonlinear $2D+t$ model (middle row), and the second-order $2D+t$ model (lower row). Results are shown over $\approx 10T_e$ for $F_B \approx 4.0$ and $\lambda/L = 4.0$, with wave steepness $\varepsilon \approx 0.02$.

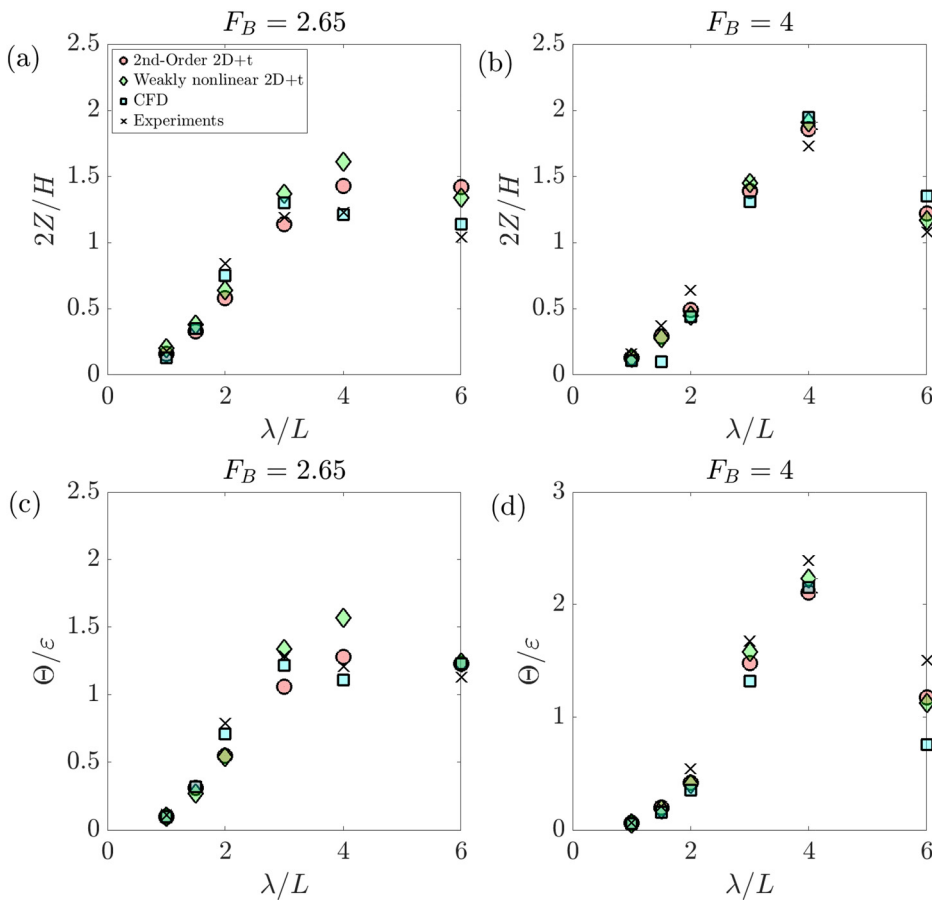


FIG. 9. Comparison between heave (a and b) and pitch (c and d) predictions from the $2D + t$ models and the CFD model against the experimental measurements of Fridsma.²⁰ Results for $F_B = 2.65$ and $F_B = 4.0$ are presented in the left and right panels, respectively.

The heave and pitch RAOs of the vessel operating at the two considered beam Froude numbers, $F_B \approx 2.65$ and $F_B \approx 4.0$, in incident waves of relative height $H/B \approx 0.111$, are presented in Fig. 9, together with the experimental measurements (cross markers) and the predictions of the CFD model (square markers), the weakly nonlinear $2D + t$ model (diamond markers), and the second-order nonlinear $2D + t$ model (circle markers).

The motion results from all the models are seen to follow the physics well. Specifically, the RAOs of heave and pitch motions approach 0 as $\lambda/L \rightarrow 0$, and tend to 1.0 as $\lambda/L \rightarrow \infty$, with resonance of heave and pitch motions occurring when waves are between $3L$ and $4L$ in length. Given that the experimental measurements serve as the reference values for validation, one can conclude that all the models demonstrate satisfactory accuracy.

Evidently, at both speeds and in short-wave conditions (i.e., $\lambda/L \leq 1.5$), the second-order $2D + t$ model may provide improved predictions of heave and pitch RAOs relative to the earlier version of the model. This is reasonable insofar as, for shorter waves, wave steepness is higher and the nonlinear forces and moments may contribute; their contribution can be captured more accurately when the nonlinearity of restoring and hydrodynamic forces is accounted for.

In medium-length wave conditions and in the resonance zone, the CFD model and the weakly nonlinear $2D + t$ model may perform better, though not at all wavelengths, when compared with

the second-order $2D + t$ model. In long-wave conditions, all models may perform similarly.

A comparison between the vertical acceleration at the CG and those predicted numerically and computationally by the models is shown in Fig. 10. It is worth noting that the maximum upward vertical

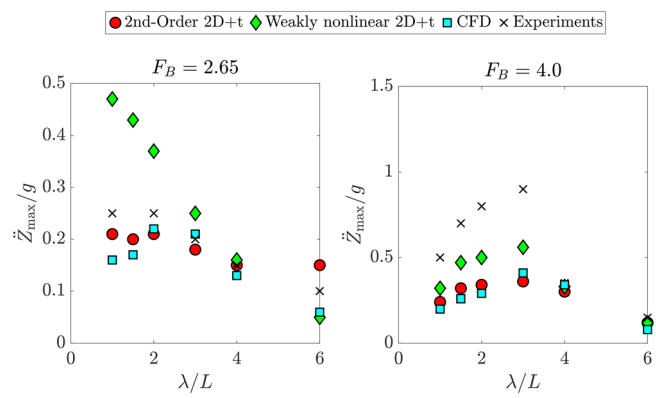


FIG. 10. Comparison between vertical acceleration predictions from the $2D + t$ models and the CFD model against the experimental measurements of Fridsma.²⁰ Results for $F_B = 2.65$ and $F_B = 4.0$ are presented in the left and right panels, respectively.

acceleration, denoted as \ddot{Z}_{MAX} , is reported. Evidently, at the lower speed, the maximum acceleration decreases with increasing wavelength, whereas at the higher speed, it first increases as the wavelength ratio rises from $\lambda/L = 1$ to $\lambda/L = 3$, and then decreases with further increase in wavelength. Such trends are captured by all three models. Interestingly, at the lower speed, the second-order $2D + t$ model and the CFD model appear to be more accurate than the weakly nonlinear $2D + t$ model, which significantly overpredicts the vertical acceleration at the CG over the range $1 \leq \lambda/L \leq 3$. At the higher speed, however, the weakly nonlinear $2D + t$ model is seen to be more accurate than both the CFD and the second-order $2D + t$ models, which underpredict the vertical acceleration at the CG. Nevertheless, this does not imply that the CFD and second-order $2D + t$ models perform poorly in predicting the heave and pitch motions, since they were observed to be even more accurate in reproducing the RAOs of these motions when compared with the weakly nonlinear $2D + t$ model.

A possible reason for the large errors of the $2D + t$ model in predicting the vertical acceleration is an under-prediction of the slamming force, following which the maximum acceleration occurs. Hence, a possible approach to improve the accuracy of the second-order $2D + t$ model is to equip it with additional nonlinear terms that are not currently included and are only activated when slamming occurs. Two possible reasons for the under-prediction of vertical acceleration by the CFD model can be identified. First, an artificial relaxation mechanism in the dynamic response solution may be present, which manifests itself more strongly in higher derivatives of the response (i.e., acceleration). The second possible reason is the temporal sampling rate, which may be insufficient to capture the peak acceleration, as it occurs over a very short timescale.

VII. RESULTS AND DISCUSSION

The effects of wave steepness on the heave and pitch RAOs of the boat at different operating speeds are shown in Figs. 11 and 12. These

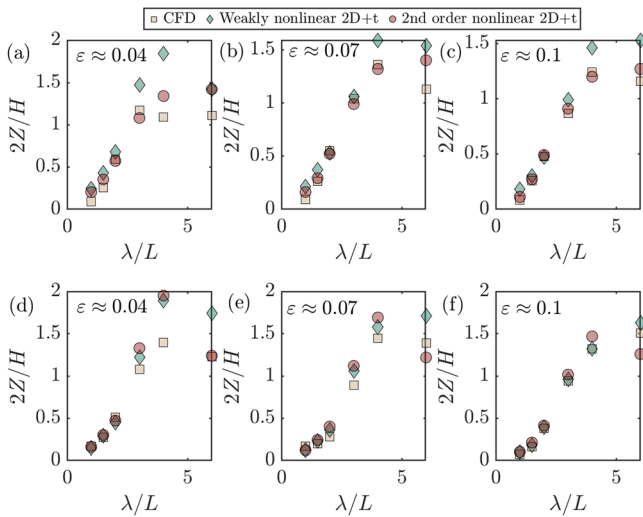


FIG. 11. RAOs of heave motion of the planing hull at beam Froude numbers $F_B \approx 2.65$ (a)–(c) and $F_B \approx 4.0$ (d)–(f), for wave steepnesses $\varepsilon \approx 0.04$ (a) and (d), $\varepsilon \approx 0.07$ (b) and (e), and $\varepsilon \approx 0.1$ (c) and (f). Results are obtained from CFD (square markers), the weakly nonlinear $2D + t$ model (diamond markers), and the second-order nonlinear $2D + t$ model (circle markers).

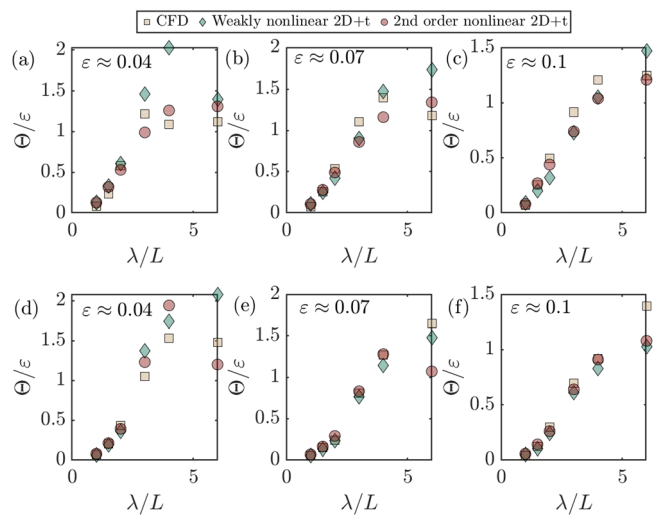


FIG. 12. RAOs of pitch motion of the planing hull at beam Froude numbers $F_B \approx 2.65$ (a)–(c) and $F_B \approx 4.0$ (d)–(f), for wave steepnesses $\varepsilon \approx 0.04$ (a) and (d), $\varepsilon \approx 0.07$ (b) and (e), and $\varepsilon \approx 0.1$ (c) and (f). Results are obtained from CFD (square markers), the weakly nonlinear $2D + t$ model (diamond markers), and the second-order nonlinear $2D + t$ model (circle markers).

results were obtained by running all three models under the wave forcing conditions listed in Table V.

In each figure, the first and second rows correspond to $F_B \approx 2.65$ and $F_B \approx 4.0$, respectively, while each panel presents RAO plots for a different wave steepness. As observed, the results for all cases and models still follow the general expectations: RAO values remain small at short waves, possible resonance occurs at comparatively medium-long waves, and RAOs tend to unity in the very long-wave limit. This can be regarded as an additional verification, indicating that all models capture the general physics under different wave steepnesses within the range $\varepsilon \leq 0.1$.

It is evident that the results of all models, while close, do not coincide at every dimensionless wavelength, which is reasonable. Each model incorporates the physics to a certain degree, and the results may therefore differ slightly or significantly depending on speed, relative wavelength, wave steepness, and the motion considered. In general, the differences between the models become more pronounced in the medium- to long-wavelength regime, where resonance or unity response occurs. In this zone, it is more likely that the vessel emerges from the water and a “flying-over” motion develops. Here, the models diverge more strongly because the forces are very large and nonlinear terms proportional to h^2 and V^2 become important.

Interestingly, in most of the cases considered, the results of the second-order $2D + t$ model are closer to those of the CFD model. This is reasonable from a fluid-dynamical perspective, since the $2D + t$ model accounts for nonlinearity to a greater degree than the weakly nonlinear model, and its predictions are therefore expected to align more closely with those of the CFD model. This difference is most evident in the larger values predicted by the weakly nonlinear model for the heave and pitch RAOs when $\lambda/L \geq 3$.

To better understand the influence of steepness on the RAO motions, the results of Figs. 11 and 12 are re-plotted in Figs. 13 and 14.

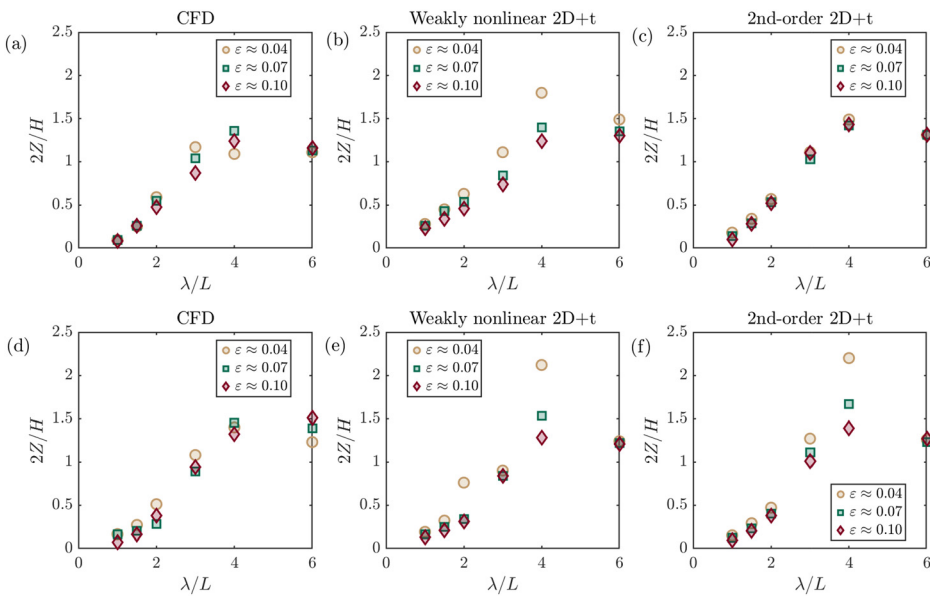


FIG. 13. Effects of wave steepness on the RAOs of heave motion at beam Froude numbers $F_B \approx 2.65$ (a)–(c) and $F_B \approx 4.0$ (d)–(f). Results from the CFD model are shown in the left panels (a) and (d), those from the weakly nonlinear $2D+t$ model in the middle panels (b) and (e), and those from the second-order $2D+t$ model in the right panels (c) and (f).

Each panel shows the effect of steepness on either the heave or pitch RAOs found by one of the models: the left panels correspond to the CFD model, the middle panels to the weakly nonlinear model, and the right panels to the second-order nonlinear $2D+t$ model. As is evident, regardless of the model employed, wave steepness affects the heave and pitch RAOs in different wave conditions. This indicates that the motions of the model are nonlinear and may vary with the incident wave characteristics. Yet, the three models do not all exhibit the same dependency on wave steepness. In general, however, it can be said that, in most cases, an increase in steepness results in a decrease in the heave and pitch RAOs. This behavior has been reported previously by several

research teams modeling the motions of ships in waves or those of floating objects. In such cases, the effect is largely attributed to the nonlinear characteristics of water waves, which also promote energy dissipation. Beyond this, it may also stem from the inherently nonlinear nature of the rigid-body motions of a high-speed planing hull, which can give rise to additional nonlinear added mass, damping and restoring forces. These, in turn, introduce higher harmonics into the wave-induced motions and can consequently modulate the overall response. This observation is consistent with responses reported for ships and other floating bodies subjected to different wave steepness (e.g., Ref. 122–124). More specifically, this observation agrees with findings of

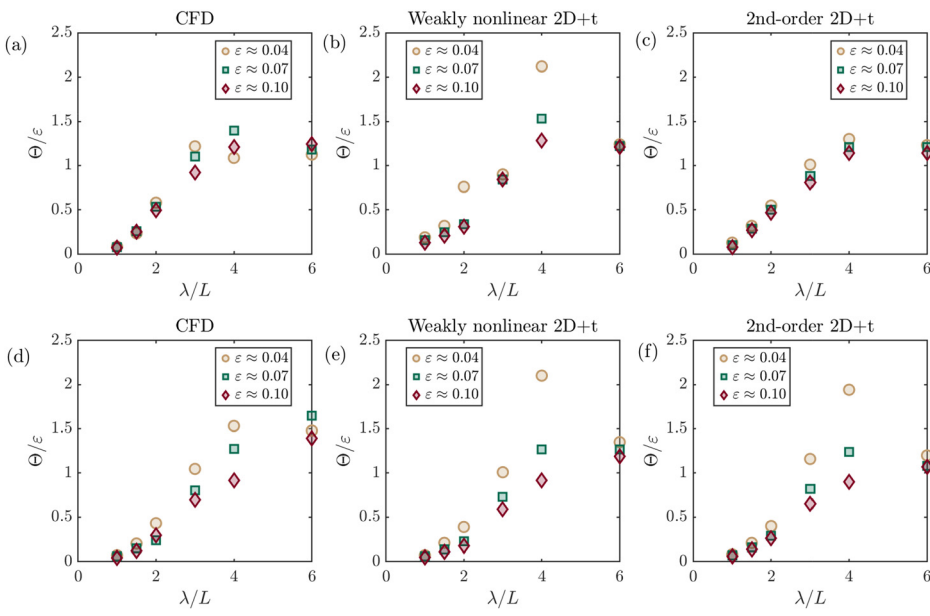


FIG. 14. Effects of wave steepness on the RAOs of pitch motion at beam Froude numbers $F_B \approx 2.65$ (a)–(c) and $F_B \approx 4.0$ (d)–(f). Results from the CFD model are shown in the left panels (a) and (d), those from the weakly nonlinear $2D+t$ model in the middle panels (b) and (e), and those from the second-order $2D+t$ model in the right panels (c) and (f).

Pigazzini *et al.*,²² who investigated the motions of planing hulls at different wave steepnesses and reported that the RAOs diminish as steepness increases, while the second-harmonic components grow.

The most striking aspect of the results concerns the RAOs at the two longest wavelengths considered, in particular the values predicted by the CFD model. Evidently, there is no monotonic or direct relationship between steepness and $2Z/H$ or Θ/ε at either of the speeds considered for $\lambda/L \geq 4$. For these waves, the RAO values may either decrease or increase with changing steepness, indicating that the influence of steepness on RAOs differs for $\lambda/L \geq 4$ compared with $\lambda/L \leq 3$ when the CFD model is used. Specifically, at $\lambda/L = 4$, increasing the wave steepness from 0.04 to 0.07 leads to an increase in heave RAO at both speeds and in pitch RAO at the lower speed, followed by a decrease as steepness increases further from 0.07 to 0.10. Interestingly, for the CFD runs at $\lambda/L = 6$, increasing steepness causes only a very slight increase in the RAO values of both heave and pitch motions.

The predictions of the two $2D + t$ models do not follow the same trend as the CFD results at $\lambda/L = 4$. Nevertheless, their predictions of the steepness effect on heave and pitch RAOs at this wavelength show closer agreement with the CFD model than might otherwise be expected. This is a strong piece of evidence that, while the $2D + t$ models may be capable of predicting the heave and pitch responses, and either of them may perform better over a specific range of forcing conditions, their results may not always follow those of a fully nonlinear model, such as a CFD model, when nonlinearities and motions become large. This is possibly linked to the fact that the $2D + t$ approach still relies heavily on simplifications of the problem, and not all nonlinear aspects are considered. Among these are the complicated splash dynamics, which introduce nonlinearities to the hydrodynamic forces, together with three-dimensional effects on the hydrostatic force and pitching moment, both of which are expected to be influential parameters in longer waves. This is because the wave period is longer, and, hence, the temporal and longitudinal gradients of pressure along the hull are smaller. The impulsive water-entry problem, representing the section of a planing ship, may therefore be equivalent to a physical

two-dimensional water-entry problem with a lower impulsive speed, during which the spray moves along the wedge wall at a reduced velocity. As such, the nonlinearities associated with the spray, which result in lower damping forces, may become more significant. Yet, this opens up future research opportunities into how such effects can be incorporated into a $2D + t$ model without under-prediction of the motions.

The second harmonics of the heave and pitch responses of the vessel at different speeds and wave steepnesses are found using the fast Fourier transform (FFT). As such, the FFT of the heave and pitch signals is calculated over a period of $\geq 15T$ and is shown as $Z(\tilde{\omega})/H$ and $\Theta(\tilde{\omega})/\varepsilon$, where $\tilde{\omega} = \omega/\omega_e$. The second harmonics are defined as the values at $\tilde{\omega} = 2$ (i.e., $\tilde{\omega} = 2\omega/\omega_e$). However, when detecting the value corresponding to the second harmonic, a tolerance of ± 0.05 is used, and the maximum value at $\tilde{\omega} = 2 = \pm 0.05$ is identified and taken as the second harmonic of the motion.

The values of the second harmonics of the heave and pitch responses of the vessel are plotted in Figs. 15 and 16, respectively, with the upper panel of each figure showing the results corresponding to $F_B \approx 2.65$, and the lower panels showing the results corresponding to $F_B \approx 4.0$. The left, middle, and right columns, respectively, show the values of the second harmonic detected in the heave and pitch signals of the responses obtained using the second-order $2D + t$ model, the weakly nonlinear $2D + t$ model, and the CFD model.

As seen, the second harmonics detected in the responses obtained using each model differ from one another (though not significantly), which is not surprising, as they may incorporate nonlinearity in different ways, with the CFD model accounting for nonlinearity at the highest level and with the least simplification. Regardless of the model used, the second harmonics of the heave and pitch motions predicted by all of them appear to be affected by wave steepness. This provides further evidence supporting the main hypothesis of this research, namely that unsteady planing motion is nonlinear. It can also be seen that the second harmonics of the heave and pitch responses may reach a peak value at $\lambda/L = 4$, which clearly confirms the influence of resonance in the second harmonic of the heave and pitch responses.

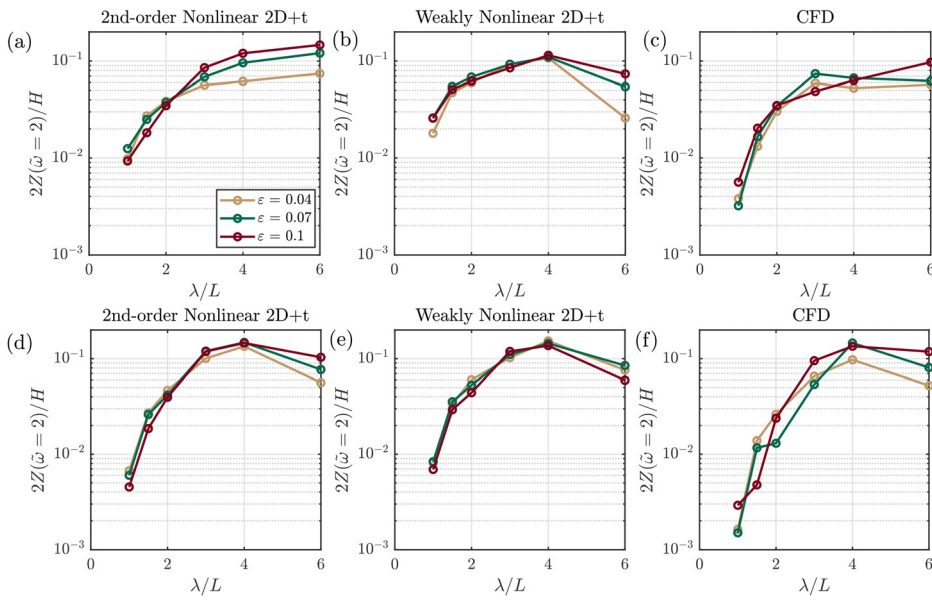


FIG. 15. Effects of wave steepness on the RAOs of second harmonic of heave motion $[2Z(\tilde{\omega} = 2)/H]$ at beam Froude numbers $F_B \approx 2.65$ (a)–(c) and $F_B \approx 4.0$ (d)–(f). Results from the CFD model are shown in the left panels (a) and (d), those from the weakly nonlinear $2D + t$ model in the middle panels (b) and (e), and those from the second-order $2D + t$ model in the right panels (c) and (f).

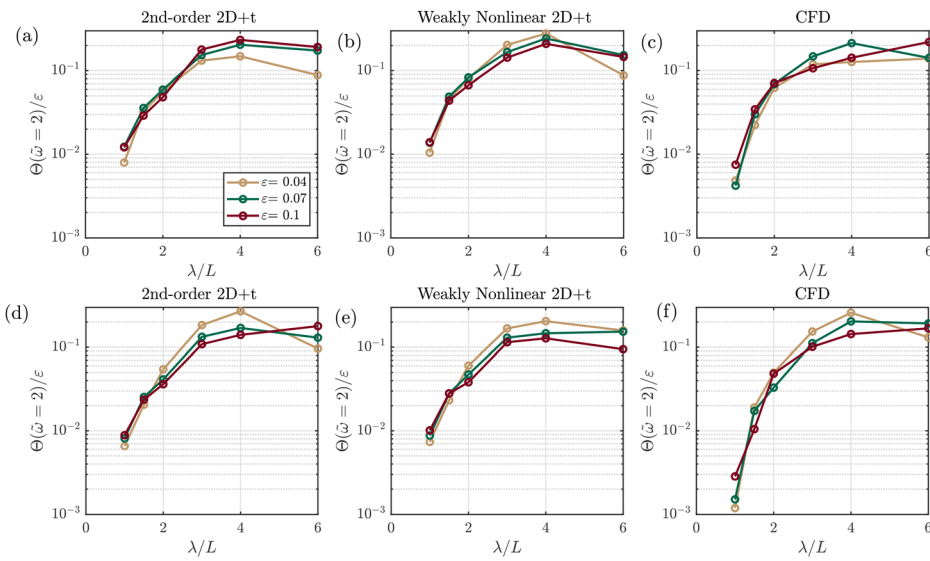


FIG. 16. Effects of wave steepness on the RAOs of second harmonic of pitch motion [$\Theta(\tilde{\omega} = 2)/\varepsilon$] at beam Froude numbers $F_B \approx 2.65$ (a)–(c) and $F_B \approx 4.0$ (d)–(f). Results from the CFD model are shown in the left panels (a) and (d), those from the weakly nonlinear 2D + t model in the middle panels (b) and (e), and those from the second-order 2D + t model in the right panels (c) and (f).

The second harmonic of the heave response predicted by the second-order nonlinear model and the CFD model is seen to decrease with increasing wave steepness in long waves, although it does not vary monotonically with wave steepness in shorter waves. In contrast,

the predictions of the weakly nonlinear model differ noticeably, with the discrepancy being most significant in the long-wave condition, where accelerations are less dominant. Hence, the effects of lift force calculation and slamming force on the response become more

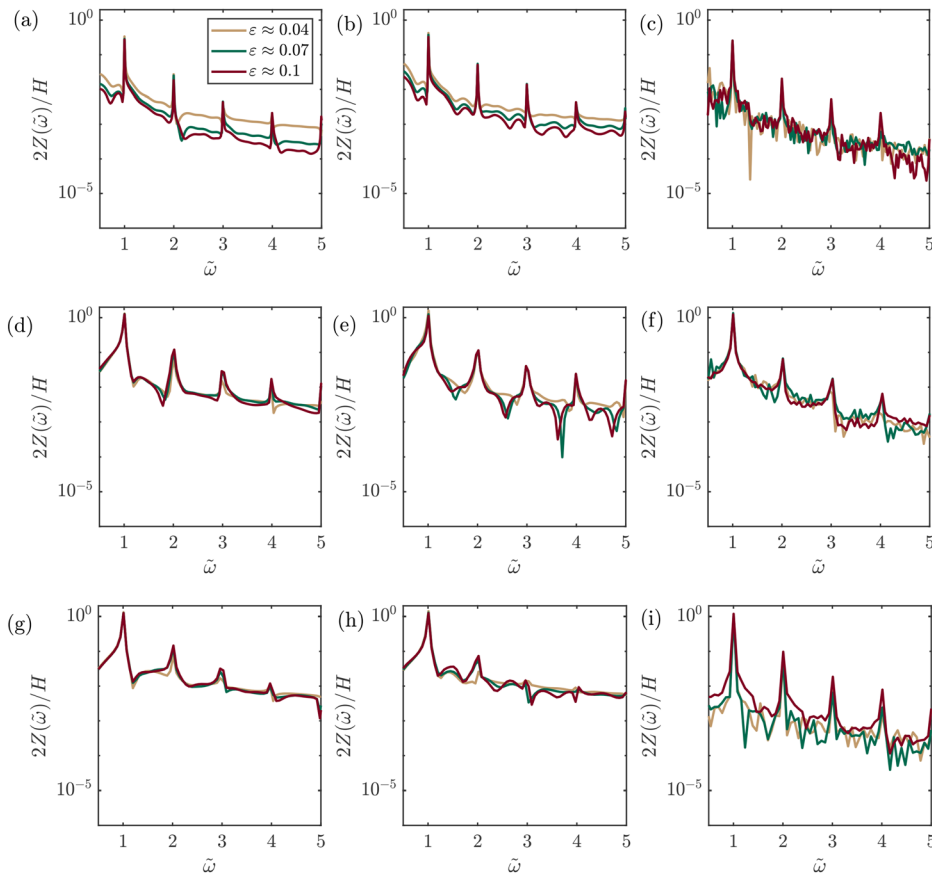


FIG. 17. Curves of $2Z(\tilde{\omega})/H$ for the heave response of the planing hull at $F_B \approx 2.65$, obtained by FFT. Results are shown for three wavelengths: $\lambda/L = 1.5$ (a)–(c), $\lambda/L = 4$ (d)–(f), and $\lambda/L = 6$ (g)–(i). Left panels (a), (d), and (g) correspond to the second-order 2D + t model, middle panels (b), (e), and (h) to the weakly nonlinear 2D + t model, and right panels (c), (f), and (i) to the CFD model.

pronounced. Accordingly, it can be concluded that the consideration of nonlinearity in the second-order $2D + t$ model allows it to capture the underlying physics more similarly to the CFD model.

The CFD model and the second-order $2D + t$ model also predict that the second harmonic at the lowest wave steepness is lower than that at higher steepnesses at lower speed. However, their predictions of the trend of the second harmonic of the pitch as a function of steepness for $\varepsilon \geq 0.07$ differ. This will be discussed later in the article when presenting the fluid flow patterns around the vessel obtained from the CFD model, but it can be briefly noted here that the difference is explained by spray generation and water detachment from the hull when the vessel rides over longer waves where flyover occurs. This primarily affects the pitch force by reducing the contribution of higher-order components.

The second harmonic of the pitch response predicted by the models exhibits two distinct behavior. For short-wave conditions, where the motion amplitudes are small and no fly-over motion occurs, the second harmonic increases with increasing wave steepness. However, for longer waves ($\lambda/L \geq 2$), where fly-over motion is more likely and frequent, it decreases with increasing wave steepness. This reduction is attributed to fly-over motion and water surface detachment. Unlike the lower-speed case, the second harmonic of the pitch response predicted by the $2D + t$ models shows a pattern very similar to that of the CFD model. This is because, at higher speeds, the fly-

over motion becomes more pronounced and lasts longer, enabling the $2D + t$ models to reproduce a pattern closer to that of the CFD model. The emergence of fly-over motion under the increase in wave steepness is shown in Appendix E.

An interesting point to note here concerns the observations made regarding the second-order harmonics and those reported by Pigazzini *et al.*,²² who observed that the second harmonic of the response has a direct relationship with wave steepness. This does not fully align with the findings of the present study. The discrepancy is likely because the model tested by Pigazzini *et al.*²² operated at $F_B < 2.3$, with the highest-speed tests limited to $\varepsilon \leq 0.07$, under which fly-over motion is not expected to occur. Therefore, a monotonic relationship between the second harmonic and wave steepness was expected in the results of Pigazzini *et al.*²² The effects of wave steepness on vertical acceleration at CG is not presented in the main body of the manuscript and is just briefly shown in Appendix F.

A better physical understanding of the responses predicted by each model may be gained by examining the FFT of the response, which are only presented for heave motion, and are plotted on a logarithmic scale in Figs. 17 and 18. In Figs. 17 and 18, the left panels show the FFT of the heave/pitch motions predicted by the second-order $2D + t$ model, the middle panels show those of the weakly nonlinear $2D + t$ model, and the right panels show those of the CFD model. Each panel shows the FFT values of the responses corresponding to

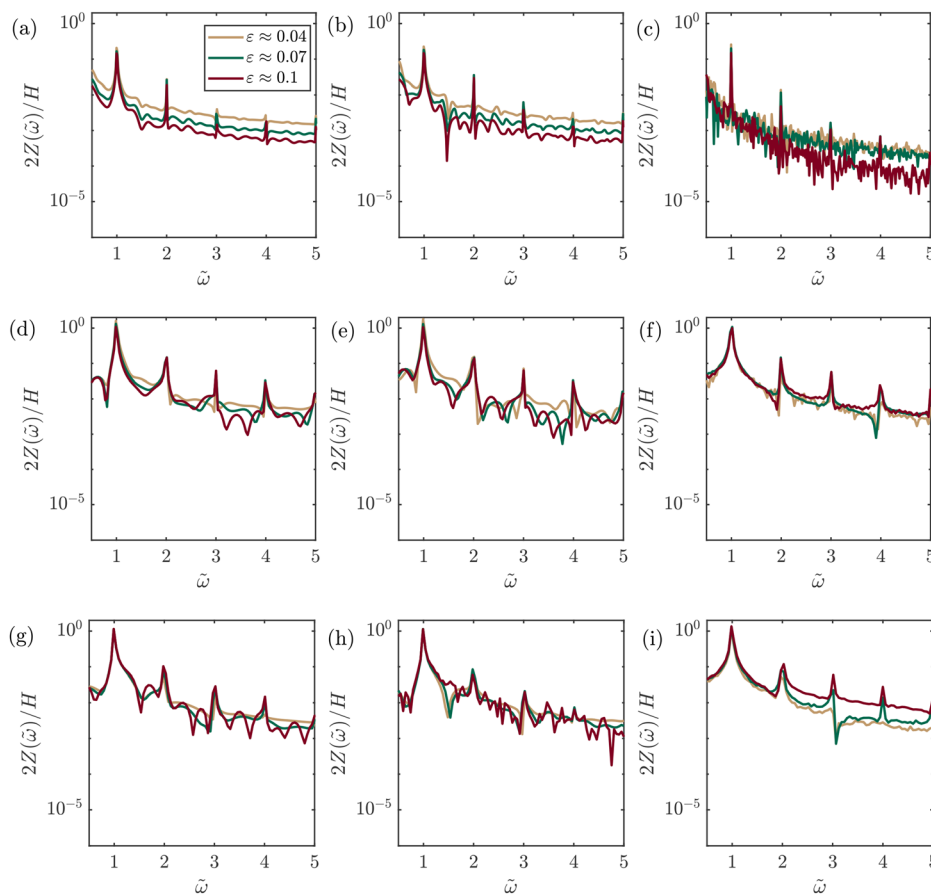


FIG. 18. Curves of $2Z(\tilde{\omega})/H$ for the heave response of the planing hull at $F_B \approx 4.0$, obtained by FFT. Results are shown for three wavelengths: $\lambda/L = 1.5$ (a)–(c), $\lambda/L = 4$ (d)–(f), and $\lambda/L = 6$ (g)–(i). Left panels (a), (d), and (g) correspond to the second-order $2D + t$ model, middle panels (b), (e), and (h) to the weakly nonlinear $2D + t$ model, and right panels (c), (f), and (i) to the CFD model.

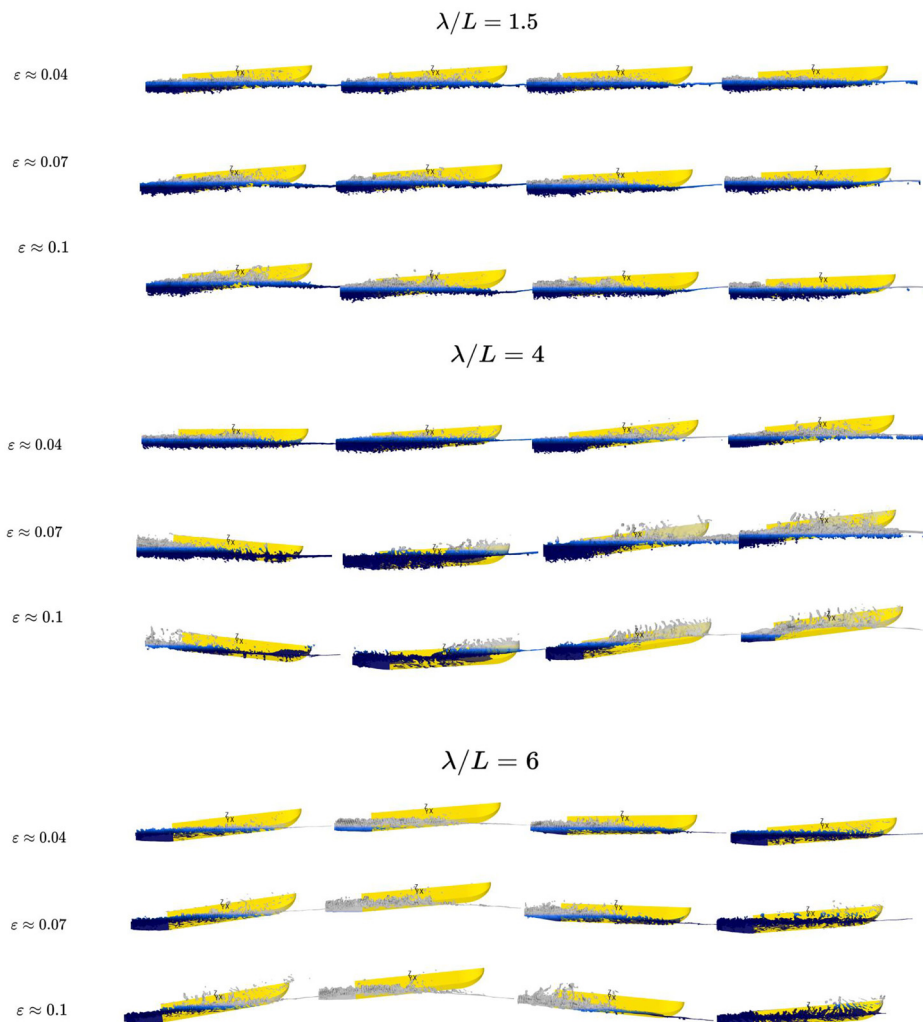


FIG. 19. Side views of the vessel motions at $F_B \approx 2.65$ under different wave conditions. The top three rows correspond to $\lambda/L = 1.5$, the middle three rows to $\lambda/L = 4$, and the bottom three rows to $\lambda/L = 6$, each shown for a range of wave steepnesses.

different wave steepnesses. For brevity, the responses are shown only for three wavelengths, $\lambda/L = 1.5$ (upper rows), 4 (middle rows), and 6 (lower rows).

As seen, the plots of $2Z(\tilde{\omega})/H$ corresponding to all considered wavelengths and Froude numbers, obtained by calculating the FFT of the heave signals predicted by any of the models, exhibit nonlinear behavior. That is, $2Z(\tilde{\omega})/H$ attain significant values at dimensionless frequencies other than $\tilde{\omega} = 1$. First, this matches the physical expectations (i.e., the dynamic motions of planing hulls are inherently nonlinear). Second, it is consistent with the observations in Figs. 13–16, where wave steepness was shown to influence the RAO values and second harmonics of the response.

The general observation from the plots of $2Z(\tilde{\omega})/H$ vs $\tilde{\omega}$ is that increasing wave steepness increase the nonlinearity of the wave-induced motions, and irregularities also begin to appear in the responses. This behavior is evident in the results of all models, interestingly confirming the earlier physical observation that nonlinearity increases with wave steepness. However, the irregularities emerging in the responses

predicted by the CFD model are more pronounced than those in the other models, particularly at $\lambda/L = 1.5$. This is an interesting observation, as the irregularities appearing at this shorter wavelength, present only in the CFD model results, are most likely due to wave scattering and diffraction effects, which are absent from the $2D + t$ formulations. The level of irregularity observed in the $2Z(\tilde{\omega})/H$ curves of the CFD model for $\lambda/L = 1.5$ increases with wave steepness.

As seen, at the lower speed, the irregularity and nonlinearity observed in $2Z(\tilde{\omega})/H$ vs $\tilde{\omega}$ predicted by the CFD model appear to be greater than those at the higher speed. However, for longer waves, the irregularities and nonlinearities in $2Z(\tilde{\omega})/H$ vs $\tilde{\omega}$ predicted by the CFD model decrease with increasing speed. This behavior is related to the fly-over motion of the vessel. At higher speeds, the fly-over motion becomes more developed, and the vessel experiences an airborne phase for a longer period, which reduces the duration over which water spray and flow detachment affect the motions. This will be discussed further in Sec. VIII. The FFT plots of pitch response of the vessel found using different models are presented in Appendix G.

VIII. FLUID FIELD AROUND THE PLANING HULL FOUND USING CFD MODEL

The results of the CFD model, run for the wave conditions outlined in Table V, are visualized in this section to provide a clearer understanding of the underlying physics. These simulations allow sampling of aspects of the surrounding fluid motion that cannot be captured by the $2D + t$ models, and they also offer further insight into the findings presented in the previous section. Results are shown in Figs. 19–24. In each figure, three wavelengths are considered: $\lambda/L = 1.5$ (top three rows), $\lambda/L = 4$ (middle three rows), and $\lambda/L = 6$ (bottom three rows). For each wavelength, results are presented for three wave steepnesses, 0.04, 0.07, and 0.1. Within each individual run, four time steps are shown, together spanning almost a full encounter period.

Figures 19 and 20 show side views of the vessel, with an iso-surface representation of the free surface and the associated spray formation, at $F_B \approx 2.65$ and $F_B \approx 4$. As observed, the wave-induced motions of the vessel (as opposed to the non-dimensional RAOs)

increase with wave steepness. This is evident when comparing results at a given time step across different steepness values, which appear in the same columns. At the higher beam Froude number, $F_B \approx 4$, the vessel exhibits fly-over motion in waves of length $4L$ and $6L$. For the shortest wavelength, at both speeds, the spray generated around the vessel attains a larger volume. This arises from the greater vessel motions and higher vertical velocities during the cycle, which displace a larger volume of water.

Interestingly, at the longest wavelength, the vessel motion is seen to follow the wave profile, consistent with physical expectation. This, however, manifests in a different pattern of fly-over motion compared with that observed for waves of length $4L$. In the $6L$ case, when the airborne phase ends, the vessel bow re-enters the water nearly tangential to the surface, leading to a relatively smooth water entry. By contrast, in the $4L$ condition, the airborne phase ends with the bow misaligned relative to the wave profile, resulting in a significant local pitch angle at the bow during re-entry.

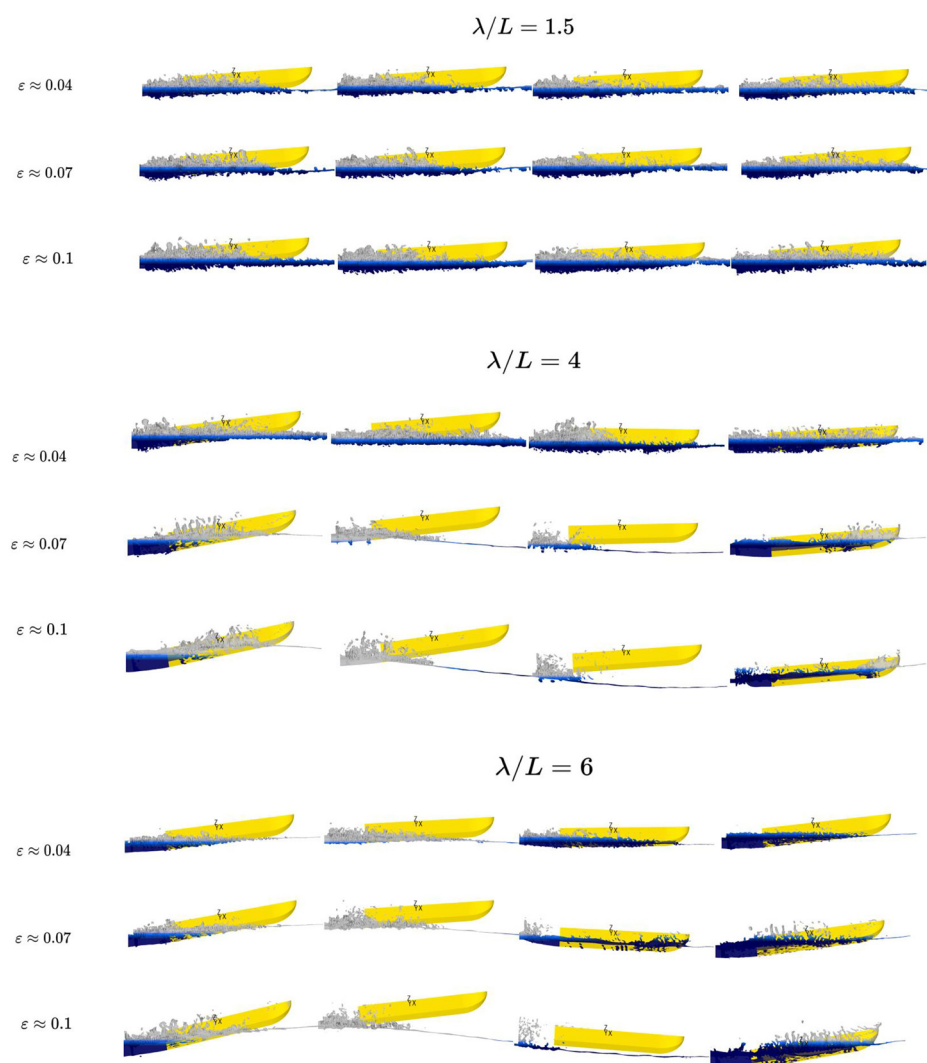


FIG. 20. Side views of the vessel motions at $F_B \approx 4$ under different wave conditions. The top three rows correspond to $\lambda/L = 1.5$, the middle three rows to $\lambda/L = 4$, and the bottom three rows to $\lambda/L = 6$, each shown for a range of wave steepnesses.

The pressure distribution acting on the planing hull advancing in different waves is shown in Figs. 21 and 22, corresponding to $F_B \approx 2.65$ and $F_B \approx 4.0$, respectively. The pressure has been normalized as

$$C_p = \frac{P}{0.5\rho_w u^2}. \quad (110)$$

It can be seen that when the vessel enters an airborne mode, the pressure acting on the bottom becomes negligible across the entire surface, as the wetted length is zero. This is followed by a pronounced slamming event, during which the pressure rises sharply. The magnitude of this slamming pressure is greater for re-entries in waves of $\lambda = 4L$, since in this case, the local pitch angle is relatively larger, thereby intensifying the impact. Interestingly, in the two steepest wave conditions at $\lambda = 4L$ and at the higher speed, the bottom-view pressure field during slamming exhibits a rounded wedge-shaped pattern, the area of which increases with steepness.

At the lower speed, no fly-over occurs in waves of $\lambda = 1.5L$ and $\lambda = 4L$, allowing a clearer view of the temporal evolution of pressure along the hull during a cycle. As the bow emerges, the pressure generally decreases with time. This may be attributed to the increase in trim angle and the conversion of kinetic to potential energy, which reduces the relative vertical velocity of the forward hull sections. Consequently, the pressure diminishes. When re-entry begins, however, slamming pressures rapidly develop and concentrate near the bow region. It is clearly observed that increasing wave steepness amplifies the pressure

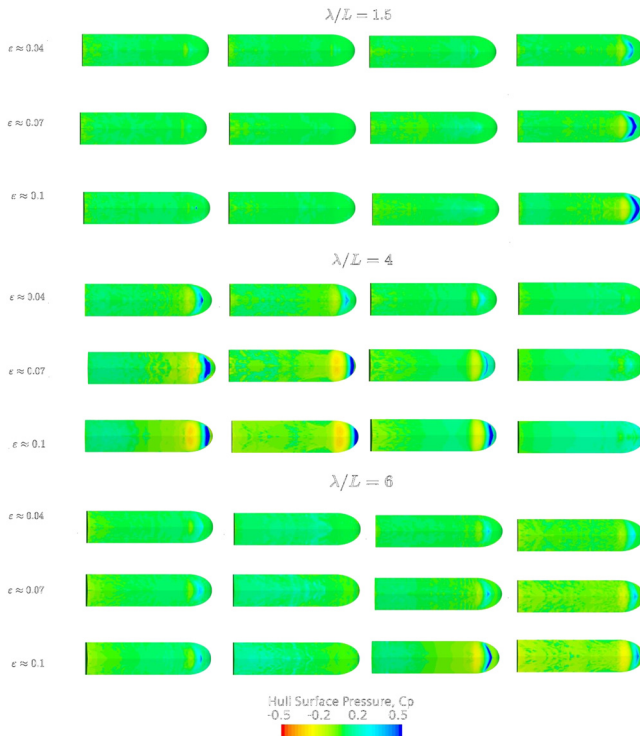


FIG. 21. Bottom-view pressure distribution on the surface of the planing hull at $F_B \approx 2.65$ under different wave conditions. The top three rows correspond to $\lambda/L = 1.5$, the middle three rows to $\lambda/L = 4$, and the bottom three rows to $\lambda/L = 6$, each shown for different wave steepnesses.

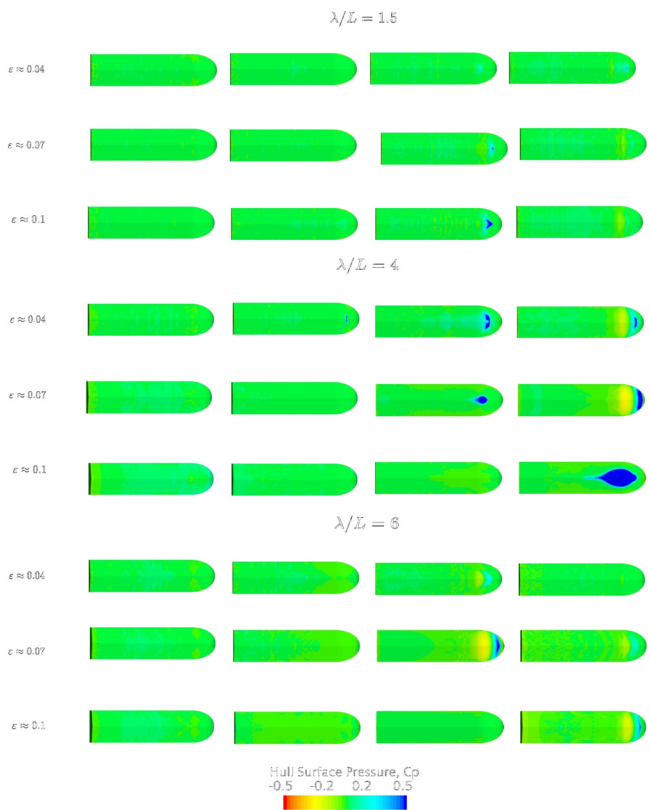


FIG. 22. Bottom-view pressure distribution on the surface of the planing hull at $F_B \approx 4$ under different wave conditions. The top three rows correspond to $\lambda/L = 1.5$, the middle three rows to $\lambda/L = 4$, and the bottom three rows to $\lambda/L = 6$, each shown for different wave steepnesses.

acting on the bow. This is evident when comparing snapshots at corresponding time steps for a given wavelength but different steepnesses. As the pressure rises, the area over which it acts also increases. This is consistent with physical expectation: in steeper waves, the height is greater, leading to higher orbital velocities and, consequently, an increased relative vertical velocity at the bow, which enhances slamming pressure.

The slamming pressure on the hull in waves of $\lambda = 4L$ is greater than that in waves of $\lambda = 1.5L$. This matches with the physical expectations. First, the dimensional wave height is larger for the longer wave, so a greater volume of water with higher kinetic energy is driven toward the vessel. Second, the RAO values and the vessel motions, particularly the velocity of the bow relative to the free surface at re-entry, are larger. Together, these effects generate greater slamming forces, which may also act over a larger wetted area.

A notable physical feature is the negative pressure that appears immediately aft of the peak slamming pressure at the bow. This can occur during planing in waves or just after re-entry when an airborne phase ends. While one might expect only a gradual drop from the peak to lower (still positive) pressure, suction pocket instead is observed. Wet-area snapshots show that the wetted footprint shrinks behind the pressure maximum and the spray root peels back along the bottom rather than shedding cleanly to the chine, i.e., partial de-

wetting/ventilation (this can be seen in Appendix H). Physically, the sectional added mass decreases during this rapid exit, and the associated unsteady term drives the local static pressure below ambient. The effect is more likely in steeper and longer waves, where heave/pitch accelerations and spray-root speed are larger. The ensuing aerated layer can generate additional vorticity and reduce hydrodynamic damping locally.

The vorticity field around the planing hull is calculated using

$$\boldsymbol{\omega} = \nabla \times \mathbf{v}. \quad (111)$$

The vorticity magnitude is calculated as

$$|\boldsymbol{\omega}| = \sqrt{\omega_x^2 + \omega_y^2 + \omega_z^2}, \quad (112)$$

where ω_x , ω_y , and ω_z are the vorticity components in the x , y , and z directions, respectively. The vorticity magnitude is normalized by the angular encounter frequency.

The vorticity fields around the planing hull at two beam Froude numbers, ≈ 2.65 and ≈ 4.0 , are shown in Figs. 23 and 24, respectively. The vorticity generated in the short-wave condition ($\lambda/L = 1.5$) is noticeably weaker than in longer waves. This is because the wave orbital velocity around the vessel is lower, and the vessel motions are also relatively small. As a result, only a weak vorticity field develops around the hull.

Interestingly, the strongest vorticity occurs in the free surface region behind the vessel, where the transom-generated waves appear. These waves are believed to be highly turbulent. Thus, although the vessel motions in short waves were shown to be nonlinear, the nonlinearity does not stem from vorticity. Instead, as explained earlier, it primarily arises from wave scattering and the nonlinear dynamics of the vessel itself.

Another notable observation is that increasing the operating speed reduces the intensity of the vorticity field behind the hull. This may be associated with the reduction in wetted-surface area and the decrease in the mean pitch angle as the vessel speed increases, both of which contribute to weaker transom waves.

Evidently, the vessel motions at $\lambda/L = 6$ generate broader and stronger vorticity zones around the hull, and in some cases even beneath it when the vessel experiences a bow-down ride. In contrast, the motions in waves of $\lambda/L = 4$ remain significant, but the regions of high vorticity are shorter and less coherent. This difference arises because, for a planing hull advancing in $\lambda/L = 6$ waves of similar steepness, the wave height is larger, resulting in stronger orbital velocities. Consequently, thicker spray sheets may form around the vessel, as a greater volume of water is driven along the hull surface before detaching at the chine.

The vorticities emerging under the bottom of planing hull at the two longer wave lengths are likely to be caused due to bow-down entrance of the vessel into the water, which may result in the fall of the free surface and highly turbulent flow below the hull.

The observation made here can well explain what was observed in Fig. 17 and 18. As seen, at the lower speed, the vorticity field around the vessel is higher, and it is expected a larger proportion of energy to be pumped into higher harmonics and into broadband content from intermittency, and, hence, signals of heave and pitch motion in waves with length of $\lambda = 6L$ are found to be more nonlinear as compared to those of $\lambda = 4L$.

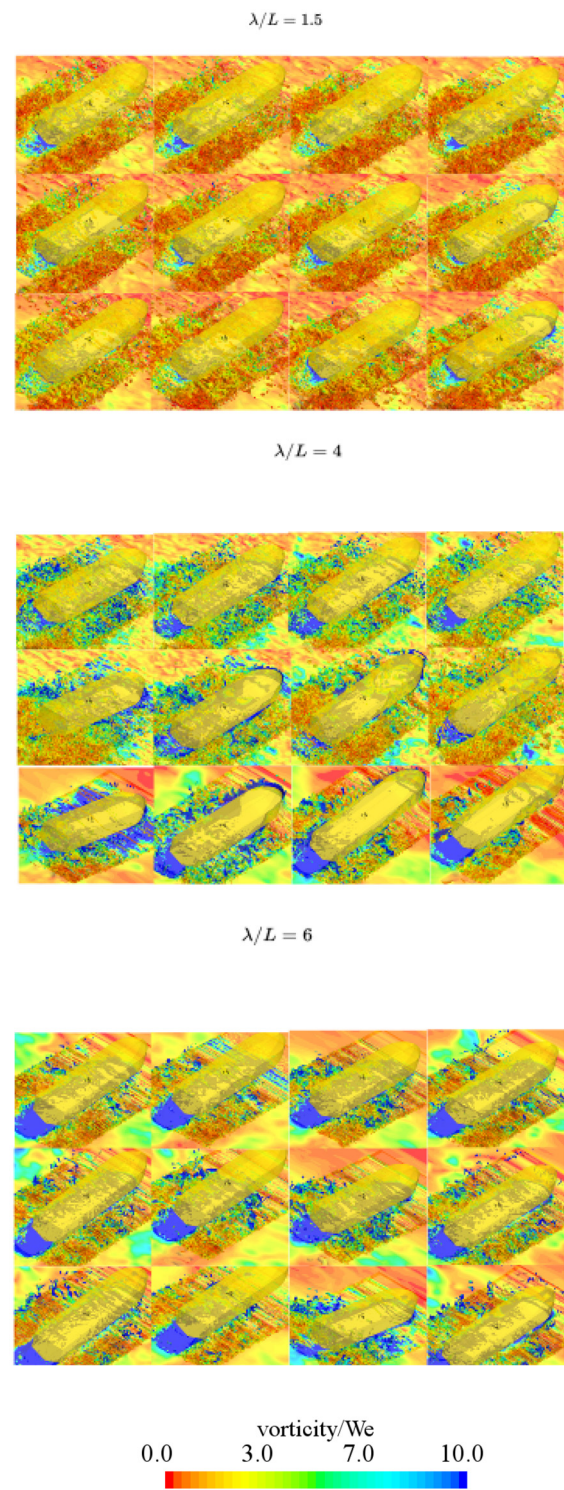


FIG. 23. Vorticity field around the planing hull at $F_B \approx 2.65$ under different wave conditions. The top three rows correspond to $\lambda/L = 1.5$, the middle three rows to $\lambda/L = 4$, and the bottom three rows to $\lambda/L = 6$, each shown for different wave steepnesses.

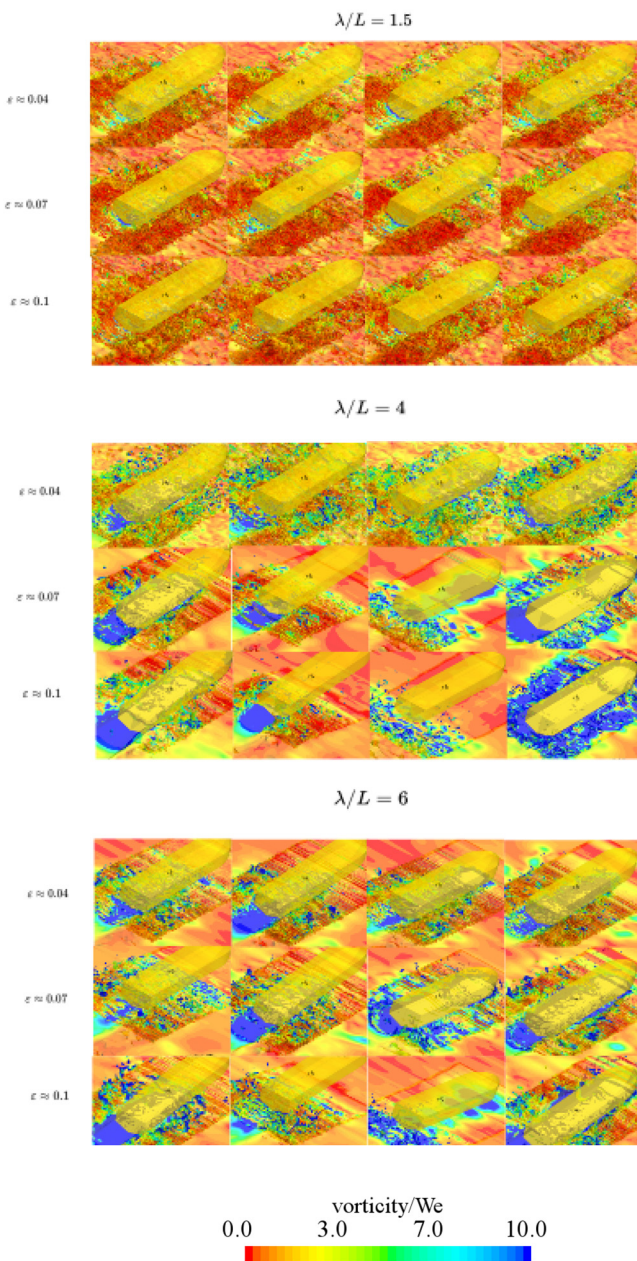


FIG. 24. Vorticity field around the planing hull at $F_B \approx 4$ under different wave conditions. The top three rows correspond to $\lambda/L = 1.5$, the middle three rows to $\lambda/L = 4$, and the bottom three rows to $\lambda/L = 6$, each shown for different wave steepnesses.

At higher speed, the hull-wave coupling at the longer wavelengths $\lambda = 4L$ and $\lambda = 6L$ weakens. The wetted contact length shortens, and the craft spends a greater fraction of each encounter cycle in fly-over. Consequently, the cycle-averaged vorticity decreases, even though individual re-entry events remain violent. This reduces the wave-locked nonlinearity associated with spray-root dynamics, ventilation, and pressure gradient. The reduction is more pronounced for

$\lambda = 6L$, since the vessel remains airborne for longer and re-enters more smoothly (with a lower local pitch angle), thereby weakening the ventilation events relative to the $\lambda = 4L$ case.

IX. COMPARATIVE SYNTHESIS OF MODELS

A final comparison between the three modeling approaches, together with notes on their applicability in physical and engineering studies, is presented in this section. The corresponding summary is provided in Table VI. It is emphasized that all three models are valuable and suitable for different purposes, rather than competing alternatives. The primary distinction between the models lies in how nonlinearities associated with the wetted surface, free-surface waves, and hydrodynamic force calculations are treated.

From a computational perspective, the fully nonlinear CFD model is the most expensive. When executed on high-performance computing facilities, simulating approximately 15 wave cycles requires several days of wall-clock time. For irregular wave conditions, the computational cost increases substantially, with simulations of around 150 cycles typically requiring 40–60 days. In contrast, both $2D + t$ models are computationally efficient. For regular wave conditions, they can complete simulations of 15 cycles within 2–5 min, while simulations under random wave conditions can be performed in approximately one hour. The low computational effort, together with an acceptable level of accuracy in predicting the responses, can be viewed as an advantage of the $2D + t$ models.

This large difference in computational cost makes the $2D + t$ models particularly suitable for early-stage vessel design, especially for preliminary assessments of hull structural response and parametric studies. Conversely, the fully nonlinear CFD model is better suited for detailed investigations of the underlying physical mechanisms, where high fidelity in resolving nonlinear flow features and wave-structure interactions is required.

From a physics perspective, the CFD model offers high-fidelity simulations and enables the resolution of spray formation and wake-driven wave patterns. These phenomena are of intrinsic interest in fundamental fluid mechanics and are also directly relevant to designers and boat builders at the final stage of the design process, immediately prior to construction. This capability, however, does not imply that the $2D + t$ models lack physical relevance. Both $2D + t$ formulations remain valuable tools for analyzing motion intermittency and nonlinear dynamics, as demonstrated by Tavakoli *et al.*,²⁵ where flyover events and intermittently wetted regions were successfully captured.

When attention is focused on higher-order harmonics, the $2D + t$ models can still provide useful insight, but their predictions must be interpreted with care. In particular, the weakly nonlinear $2D + t$ model may exhibit a loss of harmonic coherence for medium- and long-wave conditions, despite reproducing higher-harmonic content. Moreover, neither $2D + t$ formulation is able to represent irregular or scattered flow features, as they do not incorporate any explicit wave or flow scattering mechanisms.

In terms of applicability, the weakly nonlinear $2D + t$ model is best suited for near-linear wave conditions (i.e., $\epsilon < 0.05$), whereas the second-order $2D + t$ model is more appropriate for finite-amplitude waves, for which second-order Stokes wave representations remain valid. Both $2D + t$ models are restricted to the planing regime, where an impulsive flow assumption can be employed for sectional force estimation, and the present formulations are limited to hard-chine hull geometries. These constraints highlight the broader applicability of the

TABLE VI. Comparative synthesis of modeling assumptions, resolved physics, and applicability of the three different models used in the present study.

Aspect	Weakly nonlinear 2D+t	Second-order 2D+t	Fully nonlinear CFD
Wet surface nonlinearity	Weakly nonlinear	Weakly nonlinear	Fully nonlinear
Wave nonlinearity	Airy theory (linear)	Second-order Stokes	Fully nonlinear
Sectional forces	Linear	Higher-order terms	N/A (3 D fully nonlinear formulation)
Computational time for 15 T (regular waves)	2–5 min on PC (depending on steepness and speed)	2–5 min on PC (depending on steepness and speed)	7–14 days on 40 CPUs
Hull geometry	Deep-V and shallow-V planing hulls	Deep-V and shallow-V planing hulls	Any hull form
Speed range	$F_B > 1.5$	$F_B > 1.5$	Any speed
Wave steepness range	Small-amplitude waves	Finite-amplitude waves ($\epsilon < 0.2$)	High-order waves
Intermittent contact length and fly-over motion	Modeled	Modeled	Modeled
Spray formation	Cannot be captured	Cannot be captured	Can be captured
Possible sources of error	Under-prediction of damping forces	Over-prediction of damping forces	Numerical ventilation and relaxation parameters in the motion solver
Higher harmonics at short waves	Captured without irregularities related to wave scattering	Captured without irregularities related to wave scattering	Captured with expected wave scattering
Higher harmonics at medium and long waves	Captured with possible loss of harmonic coherence	Captured	Captured with expected wave scattering
Use for parametric studies	Highly suitable	Highly suitable	Limited practicality
Use for random wave modeling and statistical analyses (150T–300T)	Straightforward	Straightforward	Computationally demanding (40–60 days on HPC, large storage)
Use in engineering design	Early-stage design, rapid screening, and parametric optimization	Early-stage to intermediate design, assessment of nonlinear loads and motions	Final-stage design verification and detailed flow assessment
Use in physical and fundamental studies	Limited to nonlinear dynamics and simplified impact physics	Suitable for studying nonlinear wave impact interactions and harmonic generation	Well suited for high-fidelity investigation of spray, wake, and complex flow physics

CFD approach, which can be used to study the fluid physics around different planing hulls across a wide range of flow regimes.

X. CONCLUSION

The dynamics of planing hulls in regular and irregular waves are inherently nonlinear and cannot be resolved using standard linear models or high-order reduced models based on convolution integrals. Even conventional strip theory and three-dimensional panel models may fail to capture the behavior accurately, since the Kutta boundary condition governs the chine edges and transom. It has been shown that alternative approaches are required. In particular, 2D + t models and CFD methods have found to be suitable for predicting the dynamic motions of planing hulls at high speeds and across a range of wave steepnesses.

The use of modified versions of the Wagner solution for water entry, incorporating wave nonlinearity in the modeling of sectional forces, has been shown to improve the accuracy of predicted heave and pitch RAOs. Nevertheless, the classical Wagner solution remains a promising approach for heave and pitch responses in the longest-wave

conditions. This is likely due to the larger nonlinear damping terms in heave and pitch introduced by the modified formulation in the resonance zone.

Nonlinear effects of wave steepness on the motions were captured by all three models, each showing that increasing steepness generally reduces the heave and pitch RAOs across the tested wavelengths. However, the CFD results indicated that, in the longest waves, steepness does not lead to a monotonic decrease in RAOs, in contrast with the predictions of the 2D + t model. This may be attributed to the ability of the CFD model to resolve the turbulence field and capture cavity formation around the hull during each cycle. These effects reduce the nonlinear heave and pitch damping, such that the motions can increase with steepness at this wavelength. By contrast, at shorter wavelengths the vortical structures around the hull were weaker and primarily shed downstream, so the heave and pitch damping did not decrease with increasing steepness.

The nonlinearity of the heave and pitch responses, while generally increasing with wave steepness, was found to differ between models. In all cases, stronger nonlinearities were observed in short waves and near

resonance compared with the longest waves. The CFD predictions, however, showed pronounced nonlinearities both in short waves, likely due to wave scattering and the irregular wave field generated around the vessel, and in long waves, where strong vortical structures formed around the hull. At higher speeds, these nonlinear effects in the longest waves were observed to diminish.

This study has demonstrated the importance of nonlinearity in steep waves and highlighted the types of responses expected from different modeling approaches. While these results contribute to formulating an understanding of planing hull behavior in steep and extreme sea states, they are limited to monochromatic wave conditions. In reality, the sea must be represented by wave groups, and for steep waves, nonlinearity must also be incorporated into the group dynamics. This requires nonlinear models that account for wave-wave interactions in random seas, which may advance our understanding of planing hull responses in steep irregular waves and help to identify possible intermittency in the motions. Such developments provide a clear avenue for future research.

AUTHOR DECLARATIONS

Conflict of Interest

The authors have no conflicts to disclose.

Author Contributions

Sasan Tavakoli: Conceptualization (equal); Data curation (lead); Formal analysis (lead); Investigation (equal); Methodology (equal); Software (equal); Validation (equal); Visualization (equal); Writing – original draft (lead). **Rasul Niazmand Bilandi:** Conceptualization (equal); Formal analysis (supporting); Investigation (supporting); Methodology (supporting); Software (equal); Validation (equal); Visualization (equal); Writing – review & editing (lead). **Fatemeh Roshan:** Formal analysis (supporting); Methodology (supporting); Software (supporting); Validation (supporting); Visualization (supporting); Writing – review & editing (supporting). **Mansi Singh:** Conceptualization (supporting); Formal analysis (supporting); Methodology (supporting); Writing – review & editing (equal). **Simone Mancini:** Conceptualization (equal); Formal analysis (supporting); Investigation (supporting); Software (supporting); Validation (supporting); Writing – original draft (supporting); Writing – review & editing (equal).

DATA AVAILABILITY

The data that support the findings of this study are available from the corresponding author upon reasonable request.

APPENDIX A: SECOND-ORDER WAVE THEORY

The first- and second-order components of the water surface elevation are given by

$$\eta^{(1)} = \frac{H}{2} \cos(kx - \omega t), \quad (\text{A1})$$

$$\eta^{(2)} = \frac{H^2 k}{16} \cdot \frac{\cosh(kD)}{\sinh^3(kD)} \cdot (2 + \cosh(2kD)) \cdot \cos(2(kx - \omega t)). \quad (\text{A2})$$

The first-order component of the horizontal velocity $w_x^{(1)}$ and the second-order of the horizontal velocity $w_x^{(2)}$ are expressed as follows:

$$w_x^{(1)} = \frac{Hgk}{2\omega} \cos(kx - \omega t), \quad (\text{A3})$$

$$w_x^{(2)} = \frac{3H^2 \omega k}{16} \cdot \frac{\cosh(2kD)}{\sinh^4(kD)} \cos(2(kx - \omega t)). \quad (\text{A4})$$

The first- [$w_z^{(1)}$] and second-order [$w_z^{(2)}$] components of the vertical orbital velocity of the wave are formulated as

$$w_z^{(1)} = \frac{Hgk}{2\omega} \cdot \frac{\sinh(kD)}{\cosh(kD)} \sin(kx - \omega t), \quad (\text{A5})$$

$$w_z^{(2)} = \frac{3H^2 \omega k}{16} \cdot \frac{\sinh(2kD)}{\sinh^4(kD)} \sin(2(kx - \omega t)). \quad (\text{A6})$$

respectively. The first- ($\nu^{(1)}$) and second-order ($\nu^{(2)}$) components of the wave slope are expressed as follows:

$$\nu^{(1)} = -\frac{H}{2} k \sin(kx - \omega t), \quad (\text{A7})$$

$$\nu^{(2)} = -\frac{H^2 k^2}{16} \cdot \frac{\cosh(kD)}{\sinh^3(kD)} \cdot (\cosh(2kh)) \cdot \sin(2(kx - \omega t)). \quad (\text{A8})$$

Furthermore, theoretical background on second-order wave theory can be found in Ref. 125.

APPENDIX B: FICTIOUS HALF-WETTED BEAM FOR SECTIONS WITH WET CHINE

If the chine becomes wetted, an alternative approach to that described in Sec. III may be used. In contrast to the formulation presented in the main body of the manuscript, no minimal amplification can be applied. In such fluid-dynamic problems, a fictitious half-wetted beam is introduced, following the concept proposed by Tassin *et al.*¹¹⁸ In this case, c represents the spray-root distance from the centerline and takes values greater than $B/2$. This is achieved by imposing a zero-pressure condition at $x' = B/2$, thereby embedding the physical expectation directly into the pressure equation from which c is determined. The mathematical framework for this formulation was established by as¹¹⁸

$$\frac{h - h_c}{B} = \sqrt{1 + \tan^2 \beta} \ln \left\{ \tan \left[\frac{\pi}{4} + \frac{1}{2} \arcsin \left(\frac{1}{\sqrt{1 + \tan^2 \beta}} \times \sqrt{\frac{c^2}{(B/2)^2} - 1} \right) \right] \right\} - \sqrt{\frac{c^2}{(B/2)^2} - 1}. \quad (\text{B1})$$

In Eq. (B1), time rate of c is found by calculating the time derivative of Eq. (B1), which can be written as follows:

$$\dot{c} = \mathcal{P} \left(\frac{\mathcal{T}_1 \cdot \mathcal{T}_2}{\mathcal{T}_3} \right) \dot{h}. \quad (\text{B2})$$

\mathcal{P} , \mathcal{T}_1 , \mathcal{T}_2 , and \mathcal{T}_3 are given by

$$\mathcal{P} = \frac{B}{2c} \sqrt{\frac{c^2}{(B/2)^2} - 1}, \quad (\text{B3})$$

$$\mathcal{T}_1 = 2 \tan \left(\frac{\pi}{4} + \frac{1}{2} \arcsin \left(\frac{1}{\sqrt{1 + \tan^2 \beta}} \sqrt{\frac{c^2}{(B/2)^2} - 1} \right) \right), \quad (\text{B4})$$

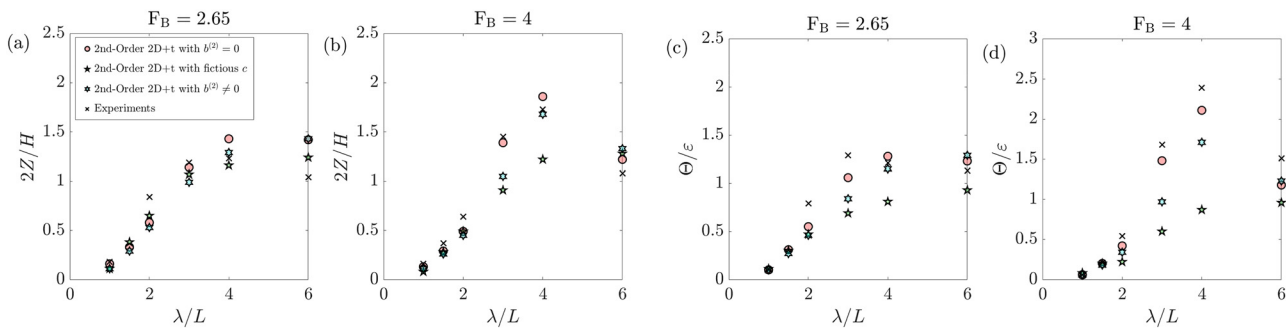


FIG. 25. Comparison of the heave and pitch predictions of the second-order nonlinear $2D + t$ model with non-zero $b^{(2)}$ and fictitious c after chine wetting, against those of the baseline model used in the manuscript with $b^{(2)} = 0$ and without a fictitious c .

$$\mathcal{T}_2 = \sqrt{1 - \left(\frac{1}{\sqrt{1 + \tan^2 \beta}} \sqrt{\frac{c^2}{(B/2)^2} - 1} \right)^2}, \quad (B5)$$

$$\mathcal{T}_3 = \sec^2 \left(\frac{\pi}{4} + \frac{1}{2} \arcsin \left(\frac{1}{\sqrt{1 + \tan^2 \beta}} \sqrt{\frac{c^2}{(B/2)^2} - 1} \right) \right), \quad (B6)$$

c can then be implemented in the pressure formulation, and a similar integral approach is used to compute the resulting force. However, a correction is applied to the terms associated with acceleration. This modification, also hypothesized by Tassin *et al.*,¹¹⁸ is intended to ensure that the resulting added mass force aligns with physical expectations. Accordingly, the pressure component associated with acceleration, denoted $p_a(x, t)$, is re-formulated as

$$p_a(x', t) = \rho_w \dot{V} (\mathcal{F}(x') - h_c + \sqrt{\left(\frac{B}{2}\right)^2 - x'^2}). \quad (B7)$$

APPENDIX C: DIFFERENT NONLINEAR $2D + t$ MODELS

As explained in the main body of the manuscript, different options exist for developing the modified version of the $2D + t$ model. One option is to include the $b^{(2)}$ term, which is usually set to zero since it is thought to introduce excessive damping and lead to over-prediction of the motion. Another option is to adopt the concept of a fictitious half-wetted beam whose extent grows with immersion, as formulated by Tassin *et al.*¹¹⁸ and presented in Appendix B. In this appendix, it is shown that either approach introduces additional damping, resulting in under-prediction of the motions.

TABLE VII. Mesh study with background domain cells, overset region cells, and resulting Z and Θ .

Mesh level	Number of cells in the background domain	Number of cells in the overset region	Z (m)	Θ ($^\circ$)
Very coarse	4 657 050	110,462	0.0295	3.059
Coarse	4 657 050	1 336 825	0.0313	3.204
Medium	4 657 050	3 783 800	0.0314	3.252
Fine	4 657 050	7 093 063	0.0310	3.312
Very fine	4 657 050	11 203 690	0.0306	3.254

To fulfill the aim of this section, two alternative formulations were tested. In the first, $b^{(2)}$ was activated and defined as follows:

$$b^{(2)} = -\rho_w c \left(\frac{1}{2} \cos^2 \beta \ln \frac{1+\epsilon}{1-\epsilon} + \epsilon (\sin^2 \beta + \pi - 2) \right), \quad (C1)$$

while in the second, the fictitious c and its corresponding time rate \dot{c} , as presented in Appendix B, were employed. The validation cases listed in Table IV were then run with these two models and compared against the results of the baseline model used in the present study.

The results of the runs performed with each model are shown in Fig. 25, where the heave and pitch RAOs are presented. As can be seen, the model employed in the manuscript predicts the responses with greater accuracy than the two alternative formulations, particularly in the resonance zone. In particular, the model with non-zero $b^{(2)}$ significantly underpredicts the pitch response.

APPENDIX D: MESH STUDY

The CFD model was run following a mesh study, as described in Sec. IV. The study was carried out for $F_B = 2.65$ under the wave condition $\lambda/L = 3$ and $H/B = 0.11$, which corresponds to one of the validation cases presented in Table IV.

Five different meshes were generated, each sharing the same background mesh but differing in cell size within the overset region. The meshes were named to reflect their respective cell sizes. The amplitudes of the heave and pitch responses were obtained using the zero-crossing method described in Sec. VI. The sensitivity of the results to mesh resolution is summarized in Table VII. The medium mesh was adopted for the simulations presented in this paper, as further mesh refinement beyond this level produced diminishing

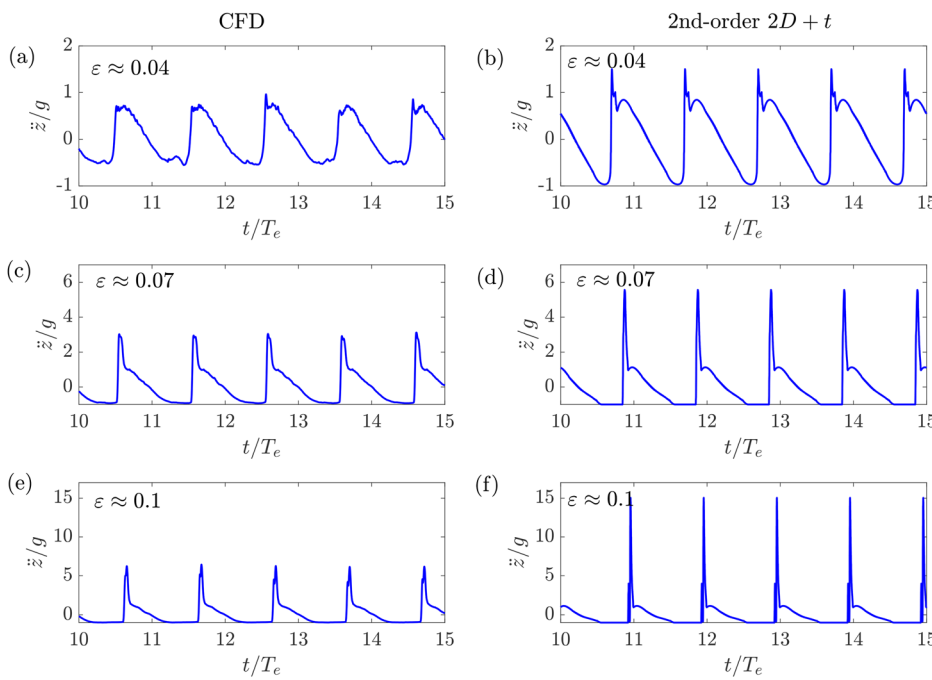


FIG. 26. Time history of vertical acceleration at the center of gravity of the vessel when traveling in waves with different wave steepnesses but the same wavelength of $\lambda/L \approx 4$ at $F_B = 4$. The results presented in the left panels are obtained from the CFD model, while those in the right panels are obtained from the second-order nonlinear model.

changes in the results while substantially increasing the computational cost.

APPENDIX E: FLY-OVER MOTION

As mentioned in the main body of the text, apart from visualization of the motions, the fly-over motion can be easily detected in the vertical acceleration plots of the vessel. It occurs when the

acceleration becomes equal to $-g$ and persists for a period longer than the sampling interval. In this appendix, it is shown how the fly-over motion emerges with increasing wave steepness when the problem is solved using both the CFD and the second-order nonlinear models. An example of the time history of the vertical acceleration at the CG of the vessel when traveling in waves with $\lambda = 4L$ at a speed corresponding to $F_B = 4$ is shown in Fig. 26. The results corresponding to three different wave steepnesses, 0.04, 0.07, and

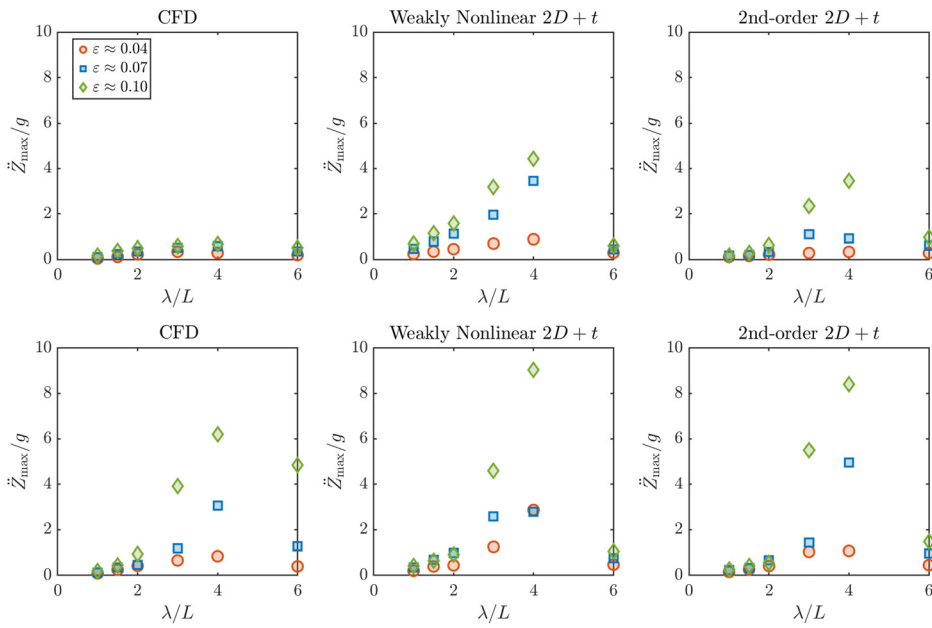


FIG. 27. The effects of wave steepness on the vertical acceleration at the center of gravity of the vessel for the two considered Froude numbers, $F_B \approx 2.65$ and $F_B \approx 4.0$.

0.1, are presented in this figure. Evidently, no fly-over motion appears in the CFD and second-order $2D+t$ simulations for $\varepsilon = 0.04$, whereas the fly-over motion is clearly detectable in the vertical acceleration time histories for $\varepsilon \approx 0.07$ and $\varepsilon \approx 0.1$. Interestingly, the fly-over motion predicted by the second-order $2D+t$ model lasts longer for $\varepsilon \approx 0.07$, while for $\varepsilon \approx 0.1$, the fly-over motion predicted by the CFD model persists for a longer duration. Finally, it should be noted that the vertical accelerations predicted by the second-order $2D+t$ model are larger than those predicted by the CFD model.

APPENDIX F: EFFECTS OF STEEPNESS ON VERTICAL ACCELERATION

This appendix briefly presents the effects of wave steepness on the vertical acceleration obtained from each of the models, without an in-depth discussion, as the main focus of the paper is on the heave and pitch responses. The maximum upward vertical acceleration of the vessel at the center of gravity for all cases outlined in Table V is shown in Fig. 27. As seen, increasing wave steepness leads to an increase in \ddot{Z}_{\max}/g . However, the predictions of the CFD

model are generally lower than those of the $2D+t$ models and show better agreement at lower speeds.

APPENDIX G: THE FFT PLOTS OF PITCH RESPONSE

The $\Theta(\tilde{\omega})/\varepsilon$ vs $\tilde{\omega}$ plots are not presented in the main text for the sake of brevity, as the pattern of the results is very similar to that of $2Z(\tilde{\omega})/H$ vs $\tilde{\omega}$. For this reason, they are included in this appendix. The results are shown in Figs. 28 and 29.

APPENDIX H: WET AREA

The wet-area pattern on the bottom of the studied hull during its ride in the steepest wave condition, for two different wavelengths $\lambda = 1.5L$ and $\lambda = 6L$ at the higher speed, is shown in Fig. 30 at four different snapshots to illustrate the features discussed in Sec. VIII.

At the lowest speed, the wave pattern around the hull is dominated by short waves, which supports the general concept that scattering around the hull enhances the presence of higher-frequency components. Together with the intermittent variation of wetted length and the associated changes in lift force (proportional to V^2),

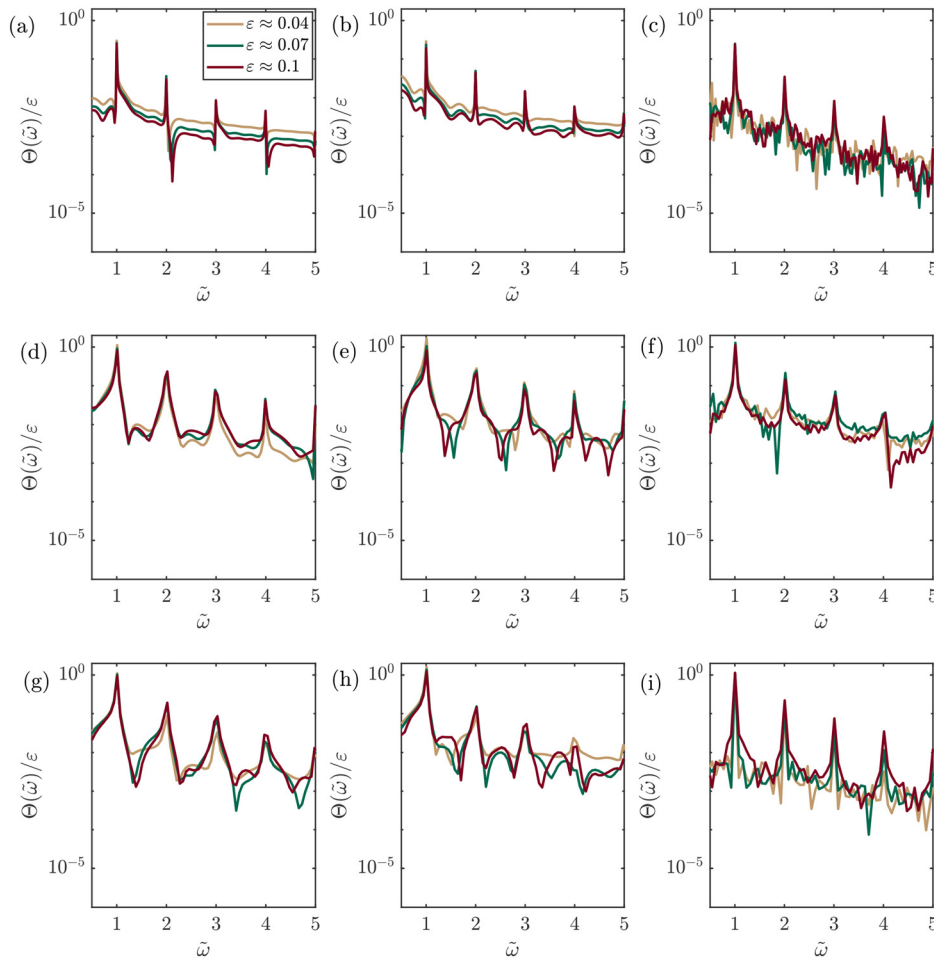


FIG. 28. Curves of $\Theta(\tilde{\omega})/\varepsilon$ for the pitch response of the planing hull at $F_B \approx 2.65$, obtained by FFT. Results are shown for three wavelengths: $\lambda/L = 1.5$ (a)–(c), $\lambda/L = 4$ (d)–(f), and $\lambda/L = 6$ (g)–(i). Left panels (a), (d), and (g) correspond to the second-order $2D+t$ model, middle panels (b), (e), and (h) to the weakly nonlinear $2D+t$ model, and right panels (c), (f), and (i) to the CFD model.

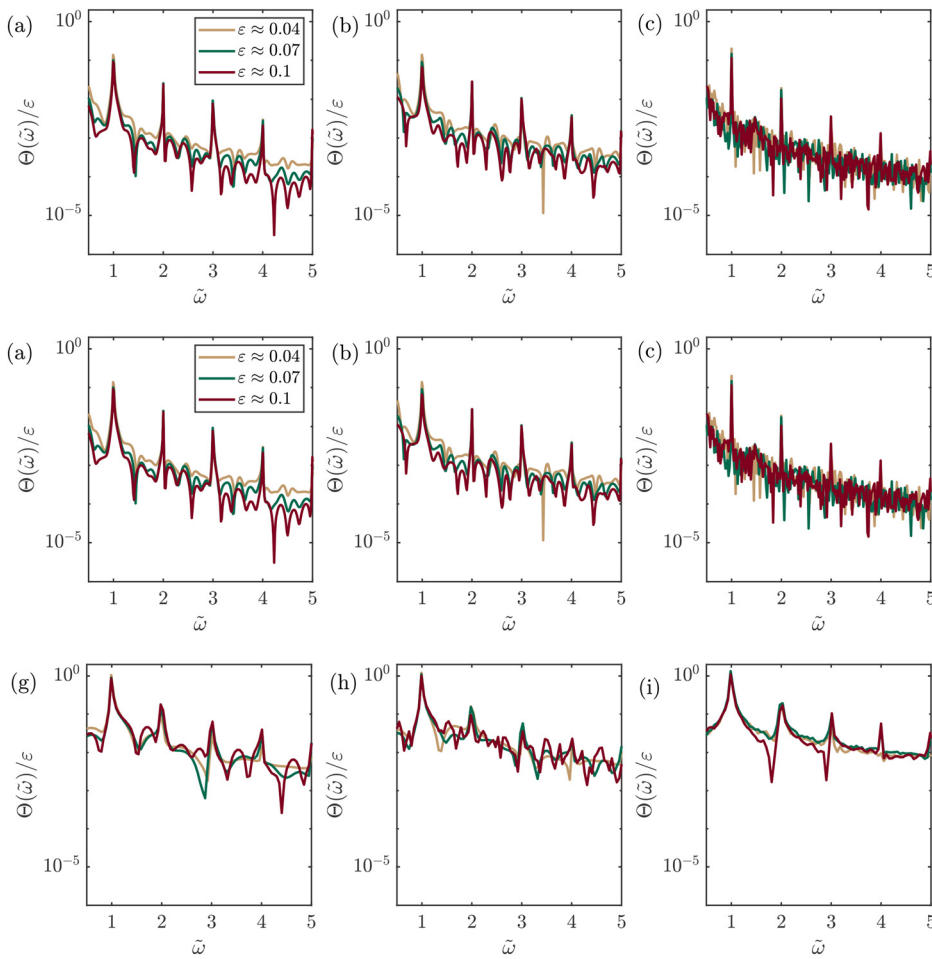


FIG. 29. Curves of $\Theta(\tilde{\omega})/\varepsilon$ for the pitch response of the planing hull at $F_B \approx 4.0$, obtained by FFT. Results are shown for three wavelengths: $\lambda/L = 1.5$ (a)–(c), $\lambda/L = 4$ (d)–(f), and $\lambda/L = 6$ (g)–(i). Left panels (a), (d), and (g) correspond to the second-order $2D + t$ model, middle panels (b), (e), and (h) to the weakly nonlinear $2D + t$ model, and right panels (c), (f), and (i) to the CFD model.

these processes generate nonlinearities. However, the nonlinearity associated with such short waves is expected to manifest primarily as irregularities in the FFT spectra of heave and pitch, as shown in

the last columns of Figs. 17 and 18. It can be well seen that the wet area on the bottom of the hull is very small and just moves from the front part to the middle part of the hull.

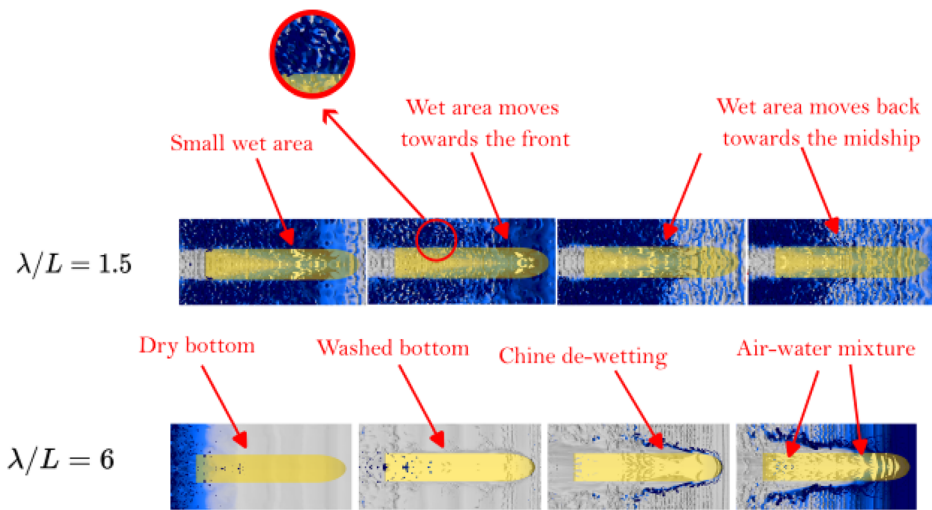


FIG. 30. Wet-area patterns on the bottom of the planing hull at different snapshots when advancing in the steepest wave condition with $F_B \approx 4$. The upper panel corresponds to $\lambda = 1.5L$, and the lower panel corresponds to $\lambda = 6L$.

In contrast, when the vessel advances in waves of length $6L$, there are instants when the bottom is almost completely dry as a result of the fly-over mode. Immediately afterward, the bottom becomes nearly washed, but soon de-wetting occurs near the chine, as indicated by the arrow. This behavior is caused by the large dimensional motions of the vessel, accompanied by a significant pitch rate. As the water separates, de-wetting develops near the chine, leading to the formation of an air–water mixture. The entrained mixture promotes energy dissipation and the generation of strong vortices beneath the hull.

REFERENCES

- ¹D. Savitsky, "Planing craft," *Nav. Eng. J.* **97**, 113 (1985).
- ²D. Savitsky, "Hydrodynamic design of planing hulls," *Mar. Technol.* **1**, 71 (1964).
- ³A. E. Green, "Note on the gliding of a plate on the surface of a stream," *Math. Proc. Cambridge Philos. Soc.* **32**, 248 (1936).
- ⁴W. Garland and K. Maki, "A numerical study of a two-dimensional stepped planing surface," *J. Ship Prod. Des.* **28**, 60 (2012).
- ⁵L. J. Doctors, "Curiosities of two-dimensional planing," *Z. Angew. Math. Phys.* **74**, 169 (2023).
- ⁶L. Olin, M. Altimira, J. Danielsson, and A. Rosén, "Numerical modelling of spray sheet deflection on planing hulls," *Proc. Inst. Mech. Eng., Part M* **231**, 811 (2017).
- ⁷D. Savitsky and M. Morabito, "Origin and characteristics of the spray patterns generated by planing hulls," *J. Ship Prod. Des.* **27**, 63 (2011).
- ⁸M. R. Kramer, K. J. Maki, and Y. L. Young, "Numerical prediction of the flow past a 2-D planing plate at low Froude number," *Ocean Eng.* **70**, 110 (2013).
- ⁹L. J. Doctors, "Pseudo-inviscid theory for transom-stern flow at low Froude numbers," *Appl. Ocean Res.* **154**, 104332 (2025).
- ¹⁰M. Rabaud and F. Moisy, "Ship wakes: Kelvin or Mach angle?," *Phys. Rev. Lett.* **110**, 214503 (2013).
- ¹¹M. Rabaud and F. Moisy, "Narrow ship wakes and wave drag for planing hulls," *Ocean Eng.* **90**, 34 (2014).
- ¹²S. Tavakoli, P. Shaghaghi, S. Mancini, F. De Luca, and A. Dashtimanesh, "Wake waves of a planing boat: An experimental model," *Phys. Fluids* **34**, 037104 (2022).
- ¹³Y. A. Semenov and B.-S. Yoon, "Onset of flow separation for the oblique water impact of a wedge," *Phys. Fluids* **21**, 112103 (2009).
- ¹⁴D. L. Blount and L. T. Codega, "Dynamic stability of planing boats," *Mar. Technol.* **29**, 4 (1992).
- ¹⁵S. H. Cohen and D. L. Blount, "Research plan for the investigation of dynamic instability of small high-speed craft," *SNAME Trans.* **94**, 197 (1986).
- ¹⁶T. Celano, "The prediction of porpoising inception for modern planing craft," *SNAME Trans.* **106**, 269 (1998).
- ¹⁷Y. Ikeda and T. Katayama, "Porpoising oscillations of very-high-speed marine craft," *Philos. Trans. R. Soc., Ser. A* **358**, 1905 (2000).
- ¹⁸A. W. Troesch and J. M. Falzarano, "Modern nonlinear dynamical analysis of vertical plane motion of planing hulls," *J. Ship Res.* **37**, 189 (1993).
- ¹⁹S. Tavakoli, R. N. Biliandi, S. Mancini, F. De Luca, and A. Dashtimanesh, "Dynamic of a planing hull in regular waves: Comparison of experimental, numerical and mathematical methods," *Ocean Eng.* **217**, 107959 (2020).
- ²⁰G. Fridsma, "A systematic study of the rough water performance of planing boats," Technical Report No. 1275 (Davidson Laboratory, Stevens Institute of Technology, 1969).
- ²¹G. Fridsma, "A systematic study of the rough water performance of planing boats—Irregular waves – Part II," Technical Report No. 1495 (Davidson Laboratory, Stevens Institute of Technology, 1971).
- ²²R. Pigazzini, F. De Luca, and C. Pensa, "An experimental assessment of nonlinear effects of vertical motions of Naples systematic series planing hulls in regular waves," *Appl. Ocean Res.* **111**, 102546 (2021).
- ²³E. Begovic, C. Bertorello, S. Pennino, V. Piscopo, and A. Scamardella, "Experimental seakeeping assessment of a warped planing hull model series," *Ocean Eng.* **83**, 1–15 (2014).
- ²⁴R. N. Biliandi, S. Tavakoli, S. Mancini, and A. Dashtimanesh, "Dynamic motion analysis of stepless and stepped planing hulls in random waves: A CFD model perspective," *Appl. Ocean Res.* **149**, 104046 (2024).
- ²⁵S. Tavakoli, R. N. Biliandi, S. Mancini, and C. Kirezci, "Nonlinear motions and dynamic intermittency of planing hulls in random wave fields: A structure-function approach," *Ocean Eng.* **343**, 123467 (2026).
- ²⁶C. Judge, M. Mousaviraad, F. Stern, E. Lee, A. Fullerton, J. Geiser, C. Schleicher, C. Merrill, C. Weil, J. Morin, M. Jiang, and C. Ikeda, "Experiments and CFD of a high-speed deep-V planing hull—Part II: Slamming in waves," *Appl. Ocean Res.* **97**, 102059 (2020).
- ²⁷E. Lee, M. Diez, E. Harrison, M. Jiang, L. Snyder, A. Powers, R. Bay, A. Serani, M. Nadal, E. Kubina, and F. Stern, "Experimental and computational fluid-structure interaction analysis and optimization of Deep-V planing-hull grillage panels subject to slamming loads—Part II: Irregular waves," *Ocean Eng.* **292**, 116346 (2024).
- ²⁸E. Lahtiuharju, T. Karppinen, M. Hellevaara, and T. Aitta, "Resistance and seakeeping characteristics of fast transom stern hulls with systematically varied form," *SNAME Trans.* **99**, 88 (1991).
- ²⁹J. Seo, H. K. Choi, U. C. Jeong, D. K. Lee, S. H. Rhee, C. M. Jung, and J. Yoo, "Model tests on resistance and seakeeping performance of wave-piercing high-speed vessel with spray rails," *Int. J. Naval Archit. Ocean Eng.* **8**, 442 (2016).
- ³⁰J. Y. Park, H. Choi, J. Lee, H. Chio, J. Woo, S. Kim, D. J. Kim, S. Y. Kim, and N. Kim, "An experimental study on vertical motion control of a high-speed planing vessel using a controllable interceptor in waves," *Ocean Eng.* **173**, 841 (2019).
- ³¹Y.-H. Lin and C.-W. Lin, "Numerical simulation of seakeeping performance on the preliminary design of a semi-planing craft," *J. Mar. Sci. Eng.* **7**, 199 (2019).
- ³²E. E. Zarnick, "A nonlinear mathematical model of motions of a planing boat in regular waves," Technical Report No. ADA052039 (David W. Taylor Naval Ship Research and Development Center, Bethesda, MD, 1978).
- ³³S. Rajendran, N. Fonseca, and C. G. Soares, "A numerical investigation of the flexible vertical response of an ultra large containership in high seas compared with experiments," *Ocean Eng.* **122**, 293 (2016).
- ³⁴T. H. von Kármán, "The impact on seaplane floats during landing," Technical Report No. NACA-TN-321 [National Advisory Committee for Aeronautics (NACA), 1929].
- ³⁵H. Wagner, "Über stoß- und gleitvorgänge an der oberfläche von flüssigkeiten," *Z. Angew. Math. Mech.* **12**, 193 (1932).
- ³⁶K. Garme, "Warp effects and bow submergence, over the limit for a 2D+T strip model of HSC," *Prog. Mar. Sci. Technol.* **7**, 3–10 (2023).
- ³⁷J. Keuning, "The nonlinear behaviour of fast monohulls in head waves," Ph.D. thesis (Technische Universiteit Delft, Delft, Netherlands, 1994).
- ³⁸R. Akers, in *Meeting of the New England Section of the Society of Naval Architects and Marine Engineers* (SNAME, 1999).
- ³⁹K. Garme, "Improved time domain simulation of planing hulls in waves by correction of the near-transom lift," *Int. Shipbuild. Prog.* **52**, 201 (2005).
- ⁴⁰V. Deyzen, "A nonlinear mathematical model of motions of a planning monohull in head seas," in *Proceedings of the 6th International Conference on High-Performance Marine Vehicles (HIPER'08)* (University of Naples, 2008).
- ⁴¹S. Hosseinzadeh, M. Khorasanchi, and M. S. Seif, "Investigation of planing vessels motion using nonlinear strip theory—An experimental and numerical study," *Ships Offshore Struct.* **14**, 684 (2019).
- ⁴²M. Ciampolini, F. Balduzzi, L. Romani, L. Bellucci, A. Bianchini, and G. Ferrara, "Development of an improved and versatile 2D+T modelling methodology for planing crafts," *Ocean Eng.* **265**, 112617 (2022).
- ⁴³D. J. Kim, K. P. Rhee, and Y. J. You, "Theoretical prediction of running attitude of a semi-displacement round bilge vessel at high speed," *Appl. Ocean Res.* **41**, 41 (2013).
- ⁴⁴P. Ghadimi, S. Tavakoli, A. Dashtimanesh, and R. Zamanian, "Steady performance prediction of a heeled planing boat in calm water using asymmetric 2D+T model," *Proc. Inst. Mech. Eng., Part M* **231**, 234 (2017).
- ⁴⁵E. Kahramanoğlu, S. Pennino, and H. Yilmaz, "Numerical evaluation of hydrodynamic characteristics of planing hulls by using a hybrid method," *Proc. Inst. Mech. Eng. Part M* **235**, 344–355 (2021)..
- ⁴⁶L. Xu, A. W. Troesch, and R. Peterson, "Asymmetric hydrodynamic impact and dynamic response of vessels," *J. Offshore Mech. Arct. Eng.* **121**, 83 (1999).
- ⁴⁷L. Xu and A. W. Troesch, "A study on hydrodynamic of asymmetric planing surfaces," in *Proceedings of the 5th International Conference on Fast Sea Transportation (FAST'99)* (FAST Conference Committee, Seattle, WA, 1999).

- ⁴⁸P. Ghadimi, S. Tavakoli, and A. Dashtimanesh, "Coupled heave and pitch motions of planing hulls at non-zero heel angle," *Appl. Ocean Res.* **59**, 286 (2016).
- ⁴⁹S. Tavakoli and A. Dashtimanesh, "Mathematical simulation of planar motion mechanism test for planing hulls by using 2D+T theory," *Ocean Eng.* **169**, 651 (2018).
- ⁵⁰S. Tavakoli and A. Dashtimanesh, "A six-DOF theoretical model for steady turning maneuver of a planing hull," *Ocean Eng.* **189**, 106328 (2019).
- ⁵¹A. Dashtimanesh, H. Enshaei, and S. Tavakoli, "Oblique-asymmetric 2D+T model to compute hydrodynamic forces and moments in coupled sway, roll, and yaw motions of planing hulls," *J. Ship Res.* **63**, 1–15 (2019).
- ⁵²R. Algarin and A. Bula, "A numeric study of the maneuverability of planing hulls with six degrees of freedom," *Ocean Eng.* **221**, 108514 (2021).
- ⁵³R. N. Bilandi, S. Tavakoli, and A. Dashtimanesh, "Seakeeping of double-stepped planing hulls," *Ocean Eng.* **236**, 109475 (2021).
- ⁵⁴S. C. De, "Contributions to the theory of stokes waves," *Math. Proc. Cambridge Philos. Soc.* **51**, 713 (1955).
- ⁵⁵J. D. Fenton, "A fifth-order stokes theory for steady waves," *J. Waterw., Port, Coastal, Ocean Eng.* **111**, 216 (1985).
- ⁵⁶T. Takami, W. Fujimoto, H. Houtani, and S. Matsui, "Combination of HOSM and FORM for extreme wave-induced response prediction of a ship in nonlinear waves," *Ocean Eng.* **286**, 115643 (2023).
- ⁵⁷S. Tavakoli, C. Kirezci, J. Lee, D. Sgarioto, A. T. Skvortsov, and A. V. Babanin, "A simple method for calculating the probability of quiescent periods in random seas for maritime search and rescue operations," *Ocean Eng.* **304**, 117838 (2024).
- ⁵⁸C. Kirezci, A. T. Skvortsov, D. Sgarioto, and A. V. Babanin, "Intermittency of gravity wave turbulence on the surface of an infinitely deep fluid: Directional effects," *J. Fluid Mech.* **999**, A84 (2024).
- ⁵⁹H. Sun and O. M. Faltinsen, "Dynamic motions of planing vessels in head seas," *J. Mar. Sci. Technol.* **16**, 168 (2011).
- ⁶⁰A. Korobkin, "Analytical models of water impact," *Eur. J. Appl. Math.* **15**, 821 (2004).
- ⁶¹A. A. Korobkin, "Second-order Wagner theory of wave impact," *J. Eng. Math.* **58**, 121 (2007).
- ⁶²J. M. Oliver, "Second-order Wagner theory for two-dimensional water-entry problems at small deadrise angles," *J. Fluid Mech.* **572**, 59 (2007).
- ⁶³A. Tassin, N. Jacques, A. E. M. Alaoui, A. Nême, and B. Leblé, "Hydrodynamic loads during water impact of three-dimensional solids: Modelling and experiments," *J. Fluids Struct.* **28**, 211 (2012).
- ⁶⁴T. I. Khabakhpasheva, A. A. Korobkin, and S. Malenica, "Fluid impact onto a corrugated panel with trapped gas cavity," *Appl. Ocean Res.* **39**, 97 (2013).
- ⁶⁵A. Tassin, D. J. Piro, A. A. Korobkin, K. J. Maki, and M. J. Cooker, "Two-dimensional water entry and exit of a body whose shape varies in time," *J. Fluids Struct.* **40**, 317 (2013).
- ⁶⁶A. Korobkin, E. I. Părău, and J.-M. Vanden-Broeck, "The mathematical challenges and modelling of hydroelasticity," *Philos. Trans. R. Soc., A* **369**, 2803 (2011).
- ⁶⁷S. Volpi, M. Diez, H. S. Sadat-Hosseini, D. H. Kim, F. Stern, R. S. Thodal, and J. L. Grenestedt, "Composite bottom panel slamming of a fast planing hull via tightly coupled fluid-structure interaction simulations and sea trials," *Ocean Eng.* **143**, 240 (2017).
- ⁶⁸M. Izadi, P. Ghadimi, M. Fadavi, and S. Tavakoli, "Hydroelastic analysis of water impact of flexible asymmetric wedge with an oblique speed," *Meccanica* **53**, 2585 (2018).
- ⁶⁹M. Diez, E. J. Lee, E. L. Harrison, A. M. R. Powers, L. A. Snyder, M. J. Jiang, R. J. Bay, R. R. Lewis, E. R. Kubina, P. Mucha, and F. Stern, "Experimental and computational fluid-structure interaction analysis and optimization of deep-V planing-hull grillage panels subject to slamming loads—Part I: Regular waves," *Mar. Struct.* **85**, 103256 (2022).
- ⁷⁰C. Gilbert, J. Gilbert, and M. J. Javaherian, "Water entry of a flexible wedge: How flexural rigidity influences spray root and pressure wave propagation," *Phys. Rev. Fluids* **8**, 090502 (2023).
- ⁷¹S. Tavakoli, A. V. Babanin, and S. Hirdaris, "Hydroelastic Analysis of hard chine sections entering water—observations for use in preliminary design stage," *J. Offshore Mech. Arct. Eng.* **145**, 051901 (2023).
- ⁷²S. Tavakoli, T. Mikkola, and S. Hirdaris, "A fluid–solid momentum exchange method for the prediction of hydroelastic responses of flexible water entry problems," *J. Fluid Mech.* **965**, A19 (2023).
- ⁷³S. Tavakoli, S. Hosseinzadeh, T. D. Tsatsoulis, and S. Hirdaris, "Hydroelastic analysis of flexible asymmetric water entry of wedge-shaped bodies using a fully coupled partitioned CFD-CSD model," *Ocean Eng.* **348**, 124018 (2026).
- ⁷⁴A. Rosén, K. Garme, K. Razola, and E. Begovic, "Numerical modelling of structure responses for high-speed planing craft in waves," *Ocean Eng.* **217**, 107897 (2020).
- ⁷⁵A. M. Ibrahim and C. Q. Judge, "Investigations of hull girder slamming factor for a semi-displacement vessel using model testing," *Appl. Ocean Res.* **150**, 104084 (2024).
- ⁷⁶J. Tu, F. Feng, Y. Lu, S. Wang, and Q. Cao, "Structural strength evaluation of a planing hull based on a one-way coupled CFD-FEA," *Brodogradnja* **76**, 76407 (2025).
- ⁷⁷Z. Ren, M. J. Javaherian, and C. M. Gilbert, "Kinematic and inertial hydroelastic effects caused by vertical slamming of a flexible V-shaped wedge," *J. Fluids Struct.* **103**, 103257 (2021).
- ⁷⁸P. Peddamallu, S. Rajendran, J. Saripalli, and X. Zhou, "Coupling a time-domain code with a RANS solver for slamming analysis," *Ships Offshore Struct.* **20**, 1731 (2025).
- ⁷⁹Y. Tang, S. L. Sun, A. Abbasnia, C. G. Soares, and H. L. Ren, "A fully nonlinear BEM-beam coupled solver for fluid–structure interactions of flexible ships in waves," *J. Fluids Struct.* **121**, 103922 (2023).
- ⁸⁰S. Tavakoli, M. Singh, S. Hosseinzadeh, Z. Hu, Y. Shao, S. Wang, L. Huang, A. Grammatikopoulos, Y. P. Li, D. Khojasteh, J. Liu, A. Dolatshah, H. Cheng, and S. Hirdaris, "A review of flexible fluid-structure interactions in the ocean: Progress, challenges, and future directions," *Ocean Eng.* **342**, 122545 (2025).
- ⁸¹A. Esfandari, S. Tavakoli, and A. Dashtimanesh, "Comparison between the dynamic behavior of the non-stepped and double-stepped planing hulls in rough water: A numerical study," *J. Ship Prod. Des.* **36**, 52 (2020).
- ⁸²E. Kahramanoğlu, F. Çakıcı, and A. Doğrul, "Numerical prediction of the vertical responses of planing hulls in regular head waves," *J. Mar. Sci. Eng.* **8**, 455 (2020).
- ⁸³B. Tagliafierro, S. Mancini, P. Ropero-Giralda, J. M. Domínguez, A. J. C. Crespo, and G. Viccione, "Performance assessment of a planing hull using the smoothed particle hydrodynamics method," *J. Mar. Sci. Eng.* **9**, 244 (2021).
- ⁸⁴S. Capasso, B. Tagliafierro, S. Mancini, I. Martínez-Estévez, C. Altomare, J. M. Domínguez, and G. Viccione, "Regular wave seakeeping analysis of a planing hull by smoothed particle hydrodynamics: A comprehensive validation," *J. Mar. Sci. Eng.* **11**, 700 (2023).
- ⁸⁵A. Hosseini, S. Tavakoli, A. Dashtimanesh, P. K. Sahoo, and M. Körgesaar, "Performance prediction of a hard-chine planing hull by employing different CFD models," *J. Mar. Sci. Eng.* **9**, 481 (2021).
- ⁸⁶M. Ji, Y. Han, L. Jin, Y. Wu, Y. Wang, and Y. Kuai, "Numerical simulation on the characteristics of interface breakup and entrained bubble distribution around ship under quasi-stationary state," *Phys. Fluids* **37**, 043354 (2025).
- ⁸⁷R. Niazmand Bilandi, S. Mancini, A. Dashtimanesh, and S. Tavakoli, "A revisited verification and validation analysis for URANS simulation of planing hulls in calm water," *Ocean Eng.* **293**, 116589 (2024).
- ⁸⁸A. Hosseini, S. Tavakoli, A. Dashtimanesh, T. Mikkola, and S. Hirdaris, "Drift test analysis of a conventional planing hull utilising CFD and 2D+t models," *Ocean Eng.* **308**, 118226 (2024).
- ⁸⁹T. Tezdogan, Y. K. Demirel, P. Kellett, M. Khorasanchi, A. Incecik, and O. Turan, "Full-scale unsteady RANS CFD simulations of ship behaviour and performance in head seas due to slow steaming," *Ocean Eng.* **97**, 186 (2015).
- ⁹⁰T. Tezdogan, A. Incecik, and O. Turan, "Full-scale unsteady RANS simulations of vertical ship motions in shallow water," *Ocean Eng.* **123**, 131 (2016).
- ⁹¹M. Terziev, T. Tezdogan, E. Oguz, T. Gourlay, Y. K. Demirel, and A. Incecik, "Numerical investigation of the behaviour and performance of ships advancing through restricted shallow waters," *J. Fluids Struct.* **76**, 185 (2018).
- ⁹²Y. Wei, A. Incecik, and T. Tezdogan, "A hydroelasticity analysis of a damaged ship based on a two-way coupled CFD-DMB method," *Ocean Eng.* **274**, 114075 (2023).
- ⁹³S. Ding, M. Zheng, S. Tavakoli, S. Li, J. Lan, B. Lin, T. Zou, and M. Zhang, "Research on inland ship hydrodynamic modeling and parameter identification based on CFD," *Ocean Eng.* **318**, 120064 (2025).

- ⁹⁴M. Z. Aung, A. Nazemian, and E. Boulogouris, "Computational fluid dynamics study on demihull interference and shallow water effects on resistance and wash wave of high-speed catamaran ferry using OpenFOAM," *Phys. Fluids* **37**, 087204 (2025).
- ⁹⁵C. Guedes Soares, N. Fonseca, and R. Pascoal, "Abnormal wave-induced load effects in ship structures," *J. Ship Res.* **52**, 30 (2008).
- ⁹⁶G. F. Clauss, M. Klein, C. Guedes Soares, and N. Fonseca, "Response based identification of critical wave scenarios," *J. Offshore Mech. Arct. Eng.* **135**, 031107 (2013).
- ⁹⁷M. Onorato, D. Proment, G. Clauss, and M. Klein, "Rogue waves: From nonlinear Schrödinger breather solutions to sea-keeping test," *PLoS One* **8**, e54629 (2013).
- ⁹⁸M. Klein, G. F. Clauss, S. Rajendran, C. Guedes Soares, and M. Onorato, "Peregrine breathers as design waves for wave-structure interaction," *Ocean Eng.* **128**, 199 (2016).
- ⁹⁹S. Rajendran, N. Fonseca, and C. Guedes Soares, "Prediction of vertical responses of a container ship in abnormal waves," *Ocean Eng.* **119**, 165 (2016).
- ¹⁰⁰S. Wang and C. Guedes Soares, "Experimental and numerical study of the slamming load on the bow of a chemical tanker in irregular waves," *Ocean Eng.* **111**, 369 (2016).
- ¹⁰¹S. Wang, H. D. Zhang, and C. Guedes Soares, "Slamming occurrence for a chemical tanker advancing in extreme waves modelled with the nonlinear Schrödinger equation," *Ocean Eng.* **119**, 135 (2016).
- ¹⁰²M. Klein, S. Wang, G. Clauss, and C. Guedes Soares, "Experimental study on the effect of extreme waves on a LNG carrier," *J. Mar. Sci. Appl.* **22**, 52 (2023).
- ¹⁰³S. Wang, M. Klein, S. Ehlers, G. Clauss, and C. Guedes Soares, "Analysis of the behavior of a chemical tanker in extreme waves," *J. Mar. Sci. Appl.* **23**, 877 (2024).
- ¹⁰⁴S. Wang and C. Guedes Soares, "Statistical characterization on slamming and green water impact onto a chemical tanker in extreme sea conditions," *Mar. Struct.* **103**, 103818 (2025).
- ¹⁰⁵M. Caponetto, H. Söding, and R. Azcueta, "Motion simulations for planing boats in waves," *Ship Technol. Res.* **50**, 182 (2003).
- ¹⁰⁶B. Molchanov, S. Lundmark, M. Fürth, and M. Green, "Experimental validation of spray deflectors for high speed craft," *Ocean Eng.* **191**, 106482 (2019).
- ¹⁰⁷F. Roshan, R. Niazmand Bilandi, F. De Luca, S. Mancini, P. Kujala, and A. Dashtimanesh, "High speed planing craft dynamics in irregular waves: Safety improvement using interceptor systems," *Appl. Ocean Res.* **161**, 104692 (2025).
- ¹⁰⁸S. Tavakoli, M. Zhang, A. A. Kondratenko, and S. Hirdaris, "A review on the hydrodynamics of planing hulls," *Ocean Eng.* **303**, 117046 (2024).
- ¹⁰⁹X. Mei, Y. Liu, and D. K. P. Yue, "On the water impact of general two-dimensional sections," *Appl. Ocean Res.* **21**(1), 1–15 (1999).
- ¹¹⁰C. Judge, A. W. Troesch, and M. Perlin, "Initial water impact of a wedge at vertical and oblique angles," *J. Eng. Math.* **48**, 279 (2004).
- ¹¹¹S. Wang and C. Guedes Soares, "Numerical study on the water impact of 3D bodies by an explicit finite element method," *Ocean Eng.* **78**, 73 (2014).
- ¹¹²Y. A. Semenov and A. Iafrati, "On the nonlinear water entry problem of asymmetric wedges," *J. Fluid Mech.* **547**, 231 (2006).
- ¹¹³D. Battistin and A. Iafrati, "Hydrodynamic loads during water entry of two-dimensional and axisymmetric bodies," *J. Fluids Struct.* **17**, 643 (2003).
- ¹¹⁴R. Hascoët, N. Jacques, Y.-M. Scolan, and A. Tassin, "A two-dimensional analytical model of vertical water entry for asymmetric bodies with flow separation," *Appl. Ocean Res.* **92**, 101878 (2019).
- ¹¹⁵S. Y. Sun, S. L. Sun, and G. X. Wu, "Oblique water entry of a wedge into waves with gravity effect," *J. Fluids Struct.* **52**, 49 (2015).
- ¹¹⁶M. Jalalisendi, S. Zhao, and M. Porfiri, "Shallow water entry: Modeling and experiments," *J. Eng. Math.* **104**, 131 (2017).
- ¹¹⁷A. C. Fairlie-Clarke and T. Tveitnes, "Momentum and gravity effects during the constant velocity water entry of wedge-shaped sections," *Ocean Eng.* **35**, 706 (2008).
- ¹¹⁸A. Tassin, A. A. Korobkin, and M. J. Cooker, "On analytical models of vertical water entry of a symmetric body with separation and cavity initiation," *Appl. Ocean Res.* **48**, 33 (2014).
- ¹¹⁹C. W. Hirt and B. D. Nichols, "Volume of fluid (VOF) method for the dynamics of free boundaries," *J. Comput. Phys.* **39**, 201 (1981).
- ¹²⁰Siemens, *Simcenter STAR-CCM+ 2210 Released! What's New?* (Siemens, 2022).
- ¹²¹International Towing Tank Conference, "Recommended procedures and guidelines: Practical guidelines for ship CFD," Report 7.5-03-02-03 [International Towing Tank Conference (ITTC), 2011].
- ¹²²I. Drummen, M. Wu, and T. Moan, "Experimental and numerical study of containership responses in severe head seas," *Mar. Struct.* **22**, 172 (2009).
- ¹²³M. Rodriguez and J. Spinneken, "A laboratory study on the loading and motion of a heaving box," *J. Fluids Struct.* **64**, 107 (2016).
- ¹²⁴A. Karola, S. Tavakoli, T. Mikkola, J. Matusiak, and S. Hirdaris, "The influence of wave modelling on the motions of floating bodies," *Ocean Eng.* **306**, 118067 (2024).
- ¹²⁵R. G. Dean and R. A. Dalrymple, *Water Wave Mechanics for Engineers and Scientists*, Advanced Series on Ocean Engineering (World Scientific, Singapore, 1991), Vol. 2, p. 368.